The Thermo-Mechanical Behaviour of Polymethyl Methacrylate in Roll-to-Roll Hot Embossing of Microfluidic Channels

by

Long Sun

A Doctoral Thesis

Submitted in partial fulfilment of the requirements for the award of
Doctor of Philosophy of Loughborough University

April 2020

Abstract

The roll-to-roll (R2R) hot embossing technique is developed from the conventional hot embossing technique, which has been a predominant method for fabricating microfluidic channels on polymeric materials, such as polymethyl methacrylate (PMMA). The benefits of R2R hot embossing are the ability to take advantage of conventional hot embossing, as well as the potential for mass production. However, the research in R2R hot embossing remains limited, with very few studies to test or simulate the process of R2R hot embossing. This thesis presents a systematic analysis of the R2R hot embossing by investigating the thermo-mechanical behaviour of PMMA.

Both experimental and numerical methods have been used to understand the R2R hot embossing of PMMA-based microfluidic channels. For the experimental method, a series of R2R hot embossing trials have been conducted on a PMMA film with a custom-designed generic shim. The shim contains straight line features with a relief height of 40 µm and different line widths. The trial experiment runs at different embossing temperatures from 105 to 110 °C at every one degree, while other process parameters, such as nip pressure and web moving speed, are kept constant. The numerical method employs calibration data from tensile tests and DMA to simulate the formation of microfluidic channels in the cross-sectional area using the finite element simulation package, Abaqus/Standard. A Python script has been written to automatically generate input files for these simulations.

From experimental trials of R2R hot embossing it has demonstrated that at temperatures close to T_g, there are nearly no embossed features. The transfer rate, which is calculated by dividing the highest channel depth by the stamp height, increases with line widths. The highest transfer rate is 51.3% when the a 1-mm-wide line feature is embossed at 109 °C. The simulation method employs a parallel network model with viscoplastic components calibrated from test data ranging from 90 to 110 °C and strain rate ranging from 0.001 to 0.1/s. The calibrated data agrees well with the test data, and shows

reasonable accuracy in predicting the cross-sectional profile of microfluidic channels. The Python script has been proved to be an efficient way for such numerical predictions under different process parameters. These findings have been generated to provide for guidance for microfluidic chip designers to modify shim layouts, and for process engineers to optimise the process parameters of R2R hot embossing.

Acknowledgements

Great acknowledgement is made to my supervisors, Changqing Liu and David Whalley, for they gave me enormous guidance, encouragement and inspiration which made it possible to explore the world of science and seek out the jewel of knowledge. I am also grateful that they offered me opportunities to conduct my research both at my university and a technical institution like VTT Finland, for me to broaden my horizons in both academic and industrial environments.

My visits to VTT have been enjoyable and fruitful thanks to the hospitality and support of the staff at VTT: especially, my supervisors from VTT Oulu: Teemu Alajoki, Ralph Liedert and Leena Hakalahti, and their co-workers: Jukka Pekkanen, Marika Kurkinen, Christina Liedert and Sanna Uusitalo. Teemu, Ralph and Leena have contributed greatly to the initiation and formation of the research collaborations between Loughborough University and VTT, and gave me a lot of help in my research and daily life in Finland. Thanks to VTT for providing the PMMA samples and giving access to the R2R hot embossing pilot machine and DMA.

Special thanks to the following people from Wolfson School, for providing their insights and knowledge to support my work: Zhiwen Chen, Yingying Lim, Weiwei Zhao, Li Liu, Junlei Tao, Jing Wang, Max Farrand, David Britton, Emarh Demirci, Sijung Hu, Paul Conway, Vadim Silberschmidt, Andy Harland and Liguo Zhao.

Acknowledgement is also made to the funding body of my project, Marie Curie International Research Staff Exchange Schematic Fellowship within the 7th European Community Framework (FP7-PEOPLE-2010-IRSES: Programme No.269113).

Lastly, thanks to my wife, my parents, my parents-in-law and my grandparents, for they gave me a lot of emotional help during the writing-up stage. I am sure that my PhD project is not my own but one piece which belongs to my loving, patient and supportive family. Thank you.

Contents

List of Figures

List of Tables

Abbreviations

LOC	lab-on-a-chip
MEMS	microelectromechanical systems
CVD	chemical vapour deposition
PVD	physical vapour deposition
RIE	reactive ion etching
SEM	scanning electron microscope
LIGA	lithographie (lithography), galvanoformung (electroplating), abformung (moulding)
CE	capillary electrophoresis
R2R	roll-to-roll
P2P	plate-to-plate
R2P	roll-to-plate
PMMA	polymethyl methacrylate
PDMS	polydimethylsiloxane
PC	polycarbonate
PP	polypropylene
COC	cyclic olefin polymer
COP	cyclic olefin copolymer
PS	polystyrene
PET	polyethylene teraphthalate
PE	polyethylene
PEN	polyethylene naphthalate
PVB	polyvinyl butyral
PVC	polyvinyl chloride
CA	cellulose acetate
AR	Aspect Ratio

FEA	Finite Element Analysis
FEM	Finite Element Method
DMA	Dynamic Mechanical Analysis
GB	Gigabyte
RAM	Random Access Memory
SDTA	Single Differential Thermal Analysis

Symbols

T_g	glass transition temperature	°C
ε	strain	
γ	shear strain	
$\dot{\gamma}$	shear strain rate	
σ	stress	MPa
α	coefficient of thermal expansion	1/K
ΔT	increase in temperature	K
δ_{ij}	Kronecker delta function	
$\mathbf{F}$	deformation gradient tensor	
J	Jacobian of deformation gradient tensor	
$\mathbf{B}$	left Cauchy-Green deformation tensor	
I_1, I_2, I_3	Invariants of $\mathbf{B}$	
W	strain energy density	
$\bar{\mathbf{U}}$	strain energy potential	
μ	shear modulus	MPa
K	bulk modulus	MPa
G	complex modulus	MPa
G'	the real part of complex modulus, storage modulus	MPa
G''	the imaginary part of complex modulus, complex modulus	MPa
δ	loss factor	
E	Young's modulus	MPa
υ	Poisson's ratio	
ρ	density	g/mm^3
F	force	N

P	pressure	MPa
L	length	mm
L	velocity gradient	
η	viscosity	mm^2/s
α_T	WLF shift factor	
K_v	elastic modulus of an elastic-viscous network	
K_p	plastic modulus of an elastic-viscous network	
H'	hardening modulus	
C_{ij}, K, β	hyperelastic model parameters	
ω	frequency	Hz
A	area	mm^2

Chapter 1

Introduction

1.1 Background and Context

This thesis describes a project to establish a numerical method for simulation of a microfabrication technique: the roll-to-roll (R2R) hot embossing process. R2R hot embossing is a promising technique for fabricating microfluidic channels on thermoplastic polymers, such as polymethyl methacrylate (PMMA). The project has also required mechanical characterisation of PMMA, to provide the necessary properties for validating the models against embossing experiments.

The simulation results are intended to assist in the design of embossing rollers and to allow optimisation of the processing parameters for R2R hot embossing.

1.1.1 Lab-on-a-Chip: Microfluidic Technology

Lab-on-a-chip (LOC), also known as Micro Total Analysis Systems (μTAS), is a microfluidics based technology that manipulates small volumes of fluids to perform multiple experimental or diagnostic tests [1, 2]. LOC devices have many advantages over traditional diagnostic methods [1, 3]: they are portable due to their small size; the consumption of fluid is small thus smaller sample volumes are required and less waste is

generated; and they have high surface-to-volume ratios, which leads to a fast system response and better management of chemical reactions. The small sizes of such devices also enable massively parallel implementation of operations, and they are suitable for integration.

Figure 1.1 shows a typical development process for a LOC device [1]. The concept of LOC is first developed, followed by specification of the required chemical analyses, design, computer simulation, fabrication, packaging, testing and finally prototypes are made. Note that simulation and testing results are repeatedly reviewed to optimise the design and manufacturing process.

The LOC technology is seen as a complete integration of all these necessary steps to perform a chemical or biochemical analysis, especially in high demand clinical diagnosis such as point-of-care testing [4–7], which requires analyses of DNA, proteins and other biochemical compounds from samples such as human blood and urine, near or at the site of patient care [5]. Among the commonly used products in the market are blood glucometers and pregnancy testers [5]. Although LOC devices have been developed for more than two decades [8], commercially successful LOC device-based products are still rare in the market [9, 10]. One of the main reasons is that manufacturing methods for the LOC devices have not been well-developed to meet the high-volume, low-cost manufacturing requirements [9, 10]. Fabrication of LOC devices benefits mostly from processes developed for the fabrication of microelectronics and microelectromechanical systems (MEMS) [8]. Micromachining processes identical to those for silicon involved have been used to build microstructures for LOC devices [10]. These fabrication techniques include photolithography, surface micromachining (such as chemical vapour deposition (CVD) and physical vapour deposition (PVD)) and bulk micromachining (such as dry and wet etching) [11]. For glass micromachining, there are also similar patterning processes to those used for silicon micromachining, such as wet etching and reactive ion etching (RIE), and bonding techniques. There are also polymer-based microfabrication techniques including hot embossing, injection moulding and soft lithography [1, 11].

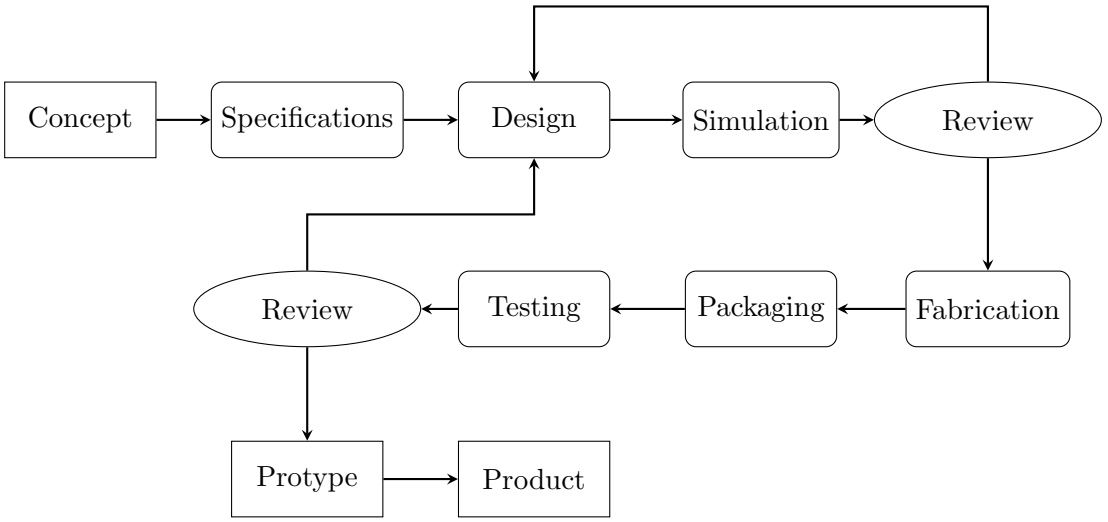

FIGURE 1.1: Development process for a LOC device from concept to product, reproduced from [1].

1.1.2 LOC Applications

LOC devices are characterised by the study and manipulation of submillimetre-scale fluids. The essential components of LOC devices do not only include microchannels but also other structures such as microvalves [12, 13], micromixers [14–16] and micropumps [17, 18]. These components have made it possible to exploit the benefit of microscale environments, where surface tension and capillary forces are more dominant than the forces produced by gravity at the macroscale. Consequently LOC devices have been used in the manipulation of fluids, for example: pumping liquid through a microchannel [19], patterning surfaces in open microchannels [20], filtering multiple analytes [21], forming monodisperse droplets in a continuous liquid stream [22]. Other than the manipulation of fluids, the widely reported LOC applications include nucleic acid biotechnology (such as DNA and RNA sequencing [23]), medical diagnostics (such as point-of-care testing [24]), drug delivery (such as screening [25, 26]) and many more emerging technologies.

1.1.3 Hot Embossing

Hot embossing[1] has been widely used for fabricating polymer-based LOC devices and has very high replication accuracy for the master structure. The size of the microstructure can be made as little as a few tens of nanometres. When used in this size range the process is named nanoimprint technology [27, 28]. The conventional hot embossing process can be described in three steps [29, 30]:

1. The polymer substrate is placed in a vacuum chamber and heated to a temperature just above its glass transition temperature. The stamp (or master structure) is heated to the same temperature.

2. The stamp is pressed into the polymer by a predefined embossing force.

3. The stamp and the substrate are isothermally cooled and separated, leaving microstructures on the sample replicated in the polymer.

The hot roller embossing is the hot embossing technique using rollers instead of plates [30], through which a continuous moulding process can be achieved. There are two approaches to roller hot embossing [30]: the first one is a single roller rolling on a flat polymer substrate, which is called roll-to-plate (R2P) hot embossing, and the second one includes two counter-rotating cylinders and the polymer film is fed between them, which is called roll-to-roll (R2R) hot embossing [31]. The R2R hot embossing process is discussed in detail in Chapter 2.

Typical hot embossing system components include heating and cooling units, mounting plates and mould inserts [30]. Heat is transferred to mould inserts however small gaps in tools may affect the uniformity of heating, which can influence the flow of polymers in the microcavities [32]. Therefore it is essential to set a holding time for the moulding process to let the flowing polymer fill the microcavities. Another factor is the measurement of temperature. A temperature sensor is placed near the polymer melt to determine

[1]The terms 'embossing' and 'coining' are similar operations in macrofabrication, where 'embossing' only refers to a forging operation of uniform structures. However, in microfabrication the term 'embossing' is used for both of the two operations.

the temperature of the melt. Other parameters include the pattern shape, size and orientation, the material properties and thickness [29, 33–35], as illustrated in Figure 1.2. These parameters are considered in conventional hot embossing and they are relevant for roll-to-roll (R2R) hot embossing as well. However, there are other parameters to be optimised in roll-to-roll hot embossing, such as the preheating time before the polymer web is fed into the embossing rollers [31, 36, 37].

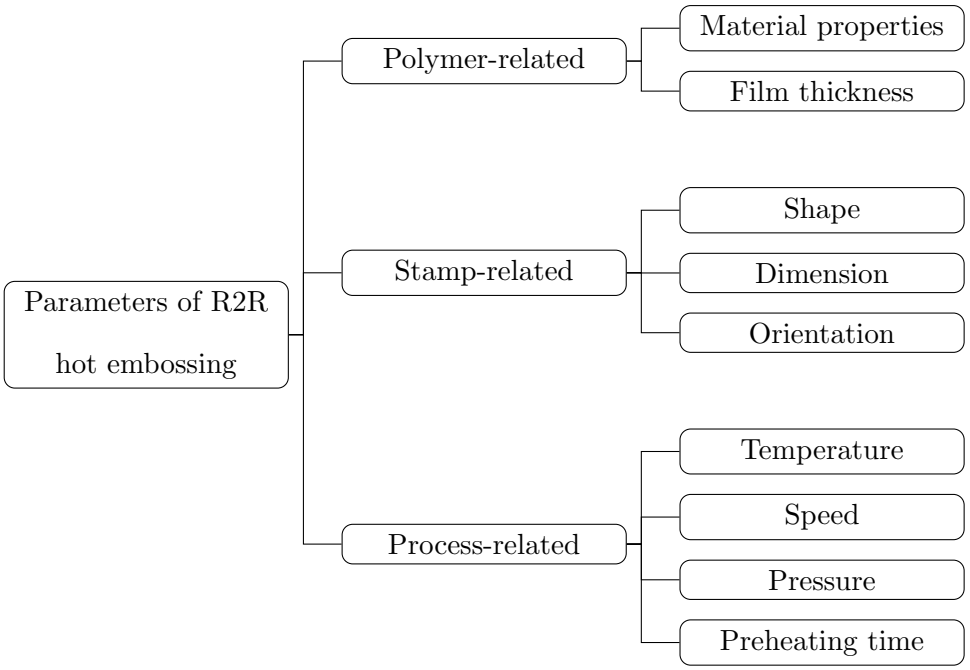

FIGURE 1.2: Parameters affecting the embossed profile in the R2R hot embossing.

The conventional and R2R hot embossing techniques have been applied in the fabrication of microfluidic chips, including a design of capillary electrophoresis (CE) chip. The principle of a CE chip is illustrated in Figure 1.3 [38]: First the sample on one side of the shorter channel is injected into the long channel by a difference in electrical potential. Once the sample has been injected into the long buffer channel, it is separated into its components depending on both their molecular size and electric charge [38]. The CE chips have been one of the first widely developed LOC devices because of their simple geometrical designs: no vertical channel profiles or high-aspect-ratio structures are needed. Still, the CE chips have achieved high sensitivity and resolution in the chemical analysis with limited amounts of test sample. After the development of these simple LOC devices, more compact and more versatile devices have emerged and the

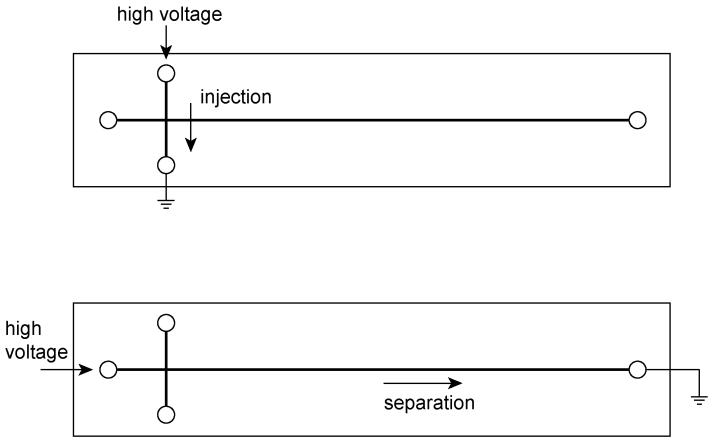

FIGURE 1.3: Principle of a capillary electrophoresis chip, reproduced from [38].

need for highly accurate micromachining techniques has raised. Geometrical designs have been made more and more complex in the planar hot embossing technique and other conventional micromachining techniques. And currently microfluidic channels are fabricated by hot embossing to micro sizes, they have been used widely in cell biology due to their similar sizes to the cells. However, there is a need to reduce the channel sizes for higher efficiency in chemical reactions and shrinking the overall sizes for LOC systems.

1.2 Research Motivation and Methodology

In current roll-to-roll hot embossing processes, the controllable parameters are optimised via a set of process trials, and there are no effective models to support these trials. The motivation of the research project is to establish an effective method to model the thermo-mechanical behaviour of the material (polymethyl methacrylate) used for R2R hot embossing and use the material model to assist the experimental work.

The PhD project has been supported by both Loughborough University and VTT[2] Technical Research Centre of Finland Ltd. in Oulu. Within VTT's research group for printed electronics, the research team of micro- and biosystems have been developing

[2]VTT is the abbreviation of Finnish words 'Valtion Teknillinen Tutkimuslaitos' (State Technical Research Centre).

microfluidic devices to realise lab-on-a-chip solutions, via planar hot embossing, R2R hot embossing and injection moulding. A joint programme between Loughborough University and VTT Oulu was established, the primary goal of which was to investigate hot embossing parameters through experiments (at VTT Oulu) and simulations (at Loughborough University).

The programme consisted of three stages: the first stage investigated the mechanical behaviour of PMMA near its glass transition temperature (T_g), through dynamic mechanical analysis (DMA) tests and tensile tests under different temperatures. The second stage involved experiments varying the process parameters during R2R hot embossing to optimise the parameters. The third stage was to develop simulations of material deformation during the R2R hot embossing process.

1.3 Aims and Objectives

Conventional and roll-to-roll hot embossing have both been widely used for fabricating polymer-based LOC devices. However, there are few published studies of modelling and simulating the polymer deformation in these hot embossing processes, especially R2R hot embossing. Therefore, it is essential to study the thermo-mechanical behaviour of the polymer from room temperature to temperatures above its glass transition temperature. A typical material used in hot embossing, the polymethyl methacrylate (PMMA), was chosen as the material to be studied in this project. It was anticipated that analogue results can be obtained for other amorphous polymer materials. The primary aim of this thesis is to investigate the thermo-mechanical behaviour of PMMA during the R2R hot embossing of microfluidic channels. To achieve the aim, the following objectives should be met:

- to review the advanced polymer-based manufacturing techniques for microfluidic chips, especially hot embossing (conventional and roll-to-roll hot embossing).

- to conduct mechanical tests on the PMMA films over a range of strains, strain rates and temperatures.
- to employ constitutive models to define the thermo-mechanical behaviour PMMA.
- to use a simulation tool for R2R hot embossing processes.
- to validate the simulation accuracy by comparing with experimental data.

1.4 Main Contributions

This thesis contributes to the area of R2R hot embossing. Specifically, it introduces the numerical and experimental methods to study the thermo-mechanical behaviour of PMMA during the R2R hot embossing of microfluidic channels. The major contributions of this study are:

1. A generic shim with different channel layout has been designed and fabricated to be used in the R2R hot embossing experiments.
2. A series of experimental trials have been conducted at every 1 °C from PMMA's glass transition temperature (T_g) to 5 °C above T_g to show the temperature effects on the thermal-mechanical behaviour of PMMA.
3. A parallel network model has been implemented to model the thermo-mechanical behaviour of PMMA and compared with mechanical calibrations experiments.
4. An automation script has been created to define the simulation files following the shim layouts and the process parameters of R2R hot embossing.
5. The method for simulating R2R hot embossing has never been published. It has shown reasonable accuracy in predicting the profiles of PMMA-based microfluidic channels after R2R hot embossing.

1.5 Thesis Structure

Following this introductory chapter, the structure of this thesis is as follows: Chapter 2 presents a literature review of the techniques which have been used to fabricate polymer-based microfluidic devices, including the master replication technique, soft lithography, thermoforming, injection moulding, hot embossing and bonding, and existing studies of the thermo-mechanical behaviours of amorphous polymers in the hot embossing process. Chapter 3 describes the methodology and results for dynamic mechanical analysis (DMA) and tensile tests on PMMA samples under different test conditions. These test results are analysed and fitted with constitutive models in Chapter 4, which presents the simulation of R2R hot embossing of microfluidic channels. The experimental results are compared with numerical simulations in Chapter 5. Chapter 6 concludes the work and gives recommendations from this project. The thesis structure is also shown in Figure 1.4.

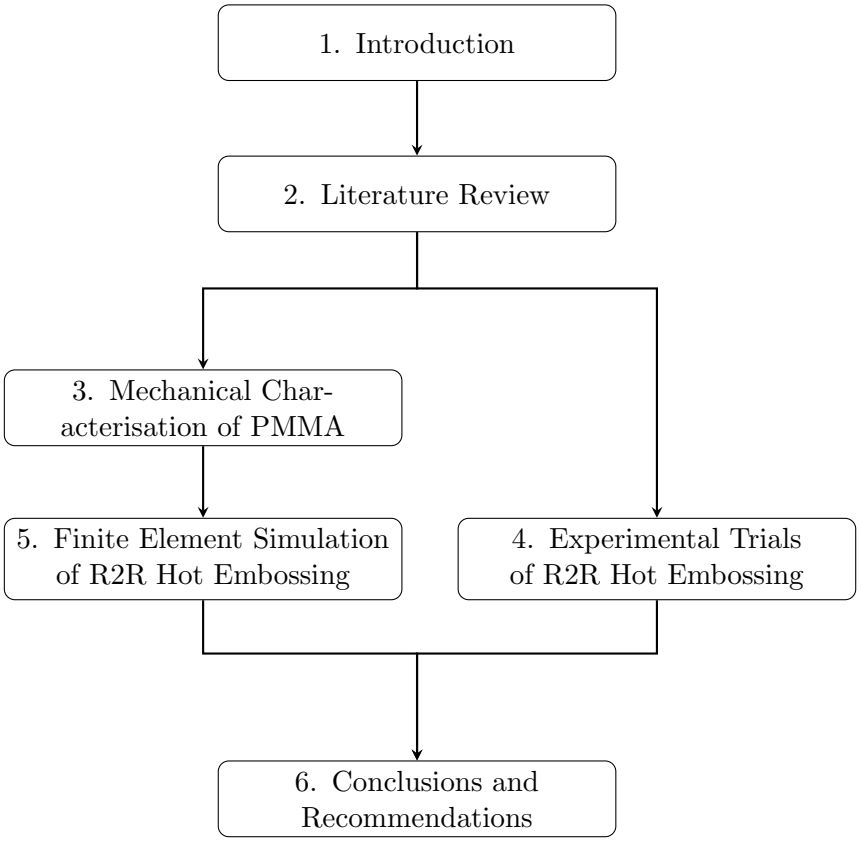

FIGURE 1.4: Structure of the thesis.

Chapter 2

Literature Review

This chapter presents the literature review for the PhD study which includes two major sections:

1. The first section describes the methods used for fabricating polymer-based microfluidic devices. The materials used for microfluidic devices will be reviewed first, followed by the introduction to replication methods for masters. The next part highlights the highly developed microfabrication technologies include injection moulding, hot embossing, thermoforming, soft lithography and the bonding techniques for closing the open microfluidic channels. In addition, roll-to-roll hot embossing is reviewed for its equipment setup, operation and control variables, pros and cons and the latest developments of R2R hot embossing.

2. The second section includes an introduction to the characteristics of thermoplastic materials and some existing constitutive models used to describe the behaviour of thermoplastics during the hot embossing process. Numerical simulations of conventional and roll-to-roll hot embossing are also reviewed.

2.1 Microfabrication of Polymer-based Microfluidic Devices

2.1.1 Geometry for Microfluidic Channels

The simplest geometry for a microfluidic channel is a rectangular cross-section, which can be fabricated with both negative and positive stamps (Figure 2.1). The aspect ratio (AR) of the cross-section is defined by the feature height h divided by the feature width w:

$$AR = \frac{h}{w} \tag{2.1}$$

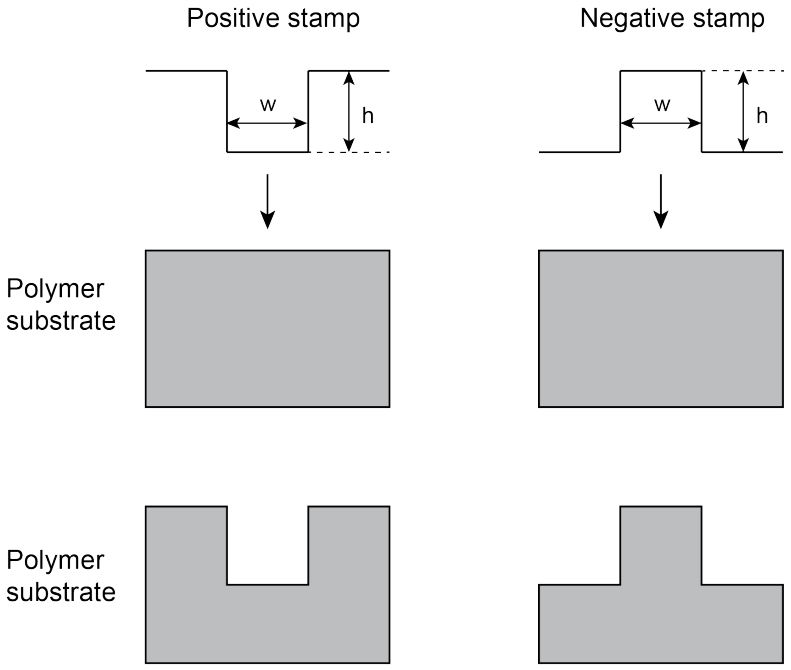

FIGURE 2.1: Schematic of positive and negative stamps.

2.1.2 Materials

Glass and silicon were used in the early development of microfluidic systems, however polymers are more attractive nowadays because of their advantages over the two traditional materials [29, 39]: polymers are transparent as glass, hard and can be processed by a wide range of fabrication techniques. Besides, polymers have very low costs per unit

area compared to glass and silicon, and are therefore well-suited to production of disposable microfluidic devices. A typical parameter used to describe the polymers' properties is the glass transition temperature (T_g), which can be measured as a distinct change in slope of the specific capacity versus temperature [29]. When the polymer is heated to above T_g, the energy of motion of the polymer chain is large enough to overcome the intra-molecular friction. Large segments of polymer chain start to depart freely so the polymer becomes flexible and soft. At the decomposition temperature, the polymer chains begin to break and the polymer decomposes. According to the physical properties around T_g, polymers can be divided into three main classes: thermosets, elastomers and thermoplastics.

Thermosets: in these materials, the molecular chains have cross-links which form during processing (for instance, when heated up or exposed to ultraviolet light). This process is called curing. When the polymers are reheated they remain stable. Therefore, they cannot be reshaped once cross-linked. At higher temperatures, the polymer decomposes and the temperature is called the decomposition temperature. A typical material used in microfluidic devices is SU-8, an excellent photoresist material and it is often used in the lithography process, while polyimide is a material which is stable at high temperatures [40].

Elastomers: in these materials, the molecular chains are longer than those in the other polymers and they do not interact with each other chemically, but rather stretch elastically under external forces. The elastomer returns to its original shape when the external force is withdrawn. A typical elastomer is polydimethylsiloxane (PDMS), a widely used prototyping material with low costs, excellent surface chemistry and ease of handling. PDMS is well-suited to the manufacturing of low-volume microfluidic devices, however for medium- to large-volume manufacturing scale there has been a lack of commercially available equipment.

Thermoplastics: these materials soften at temperatures above T_g, thus they can be processed by fabricating techniques such as hot embossing and injection moulding. Curing does not happen when the material is heated up so they can be reshaped many times

by heating. Numerous thermoplastic materials have been developed, and typical materials used in microfluidic devices are polymethyl methacrylate (PMMA), polycarbonate (PC), polypropylene (PP), polystyrene (PS), cyclic olefin polymers (COP) and cyclic olefin copolymers (COC) [40, 41].

2.1.3 Microfabrication Techniques

Micron-scale, open channels can be created on the polymer sheet by replication techniques including soft lithography, injection moulding, hot embossing and roll-to-roll (R2R) hot embossing. After the replication process another polymer sheet can be bonded to the structured polymer sheet to form a closed channel.

2.1.3.1 Masters for Replication

As masters are necessary for all replication processes, the fabrication of replication masters is one of the most crucial steps in manufacturing commercial microfluidic devices [42, 43]. In general, most microfabrication techniques are suited for the master fabrication. The most common fabrication methods are wet etching, dry etching, optical lithography, laser ablation, LIGA (German acronym for 'Lithography, Electroplating, and Moulding') and precision micromachining. Silicon masters are easy to fabricate and can be made quickly at low cost, thus they are usually used in soft lithography and hot embossing. The recent development of polymer materials such as SU-8 [44, 45] and PDMS [46, 47] can be used as replication masters. Polymer masters are soft, while silicon masters are rigid. A soft master can be used for large-area replication as it will conform and make intimate contact, which is not the case for rigid masters [11].

Master detachment (sometimes referred as de-embossing or releasing) has been an important issue in all microfabrication methods. To satisfy the detachment requirements: (a) The masters must have positively sloped walls; (b) The master surface need to be smooth; (c) Contact areas between the master and replica should not be free from chemical bonds [11].

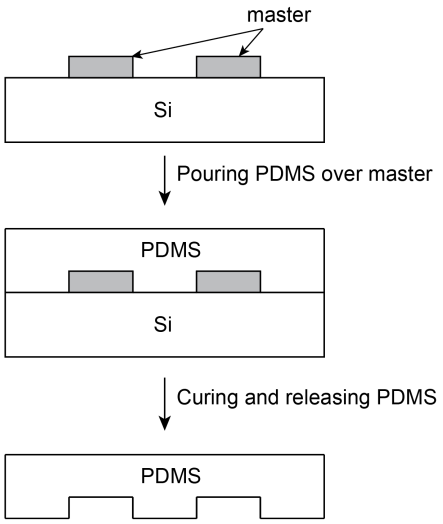

FIGURE 2.2: Illustration of the procedure for fabricating PDMS stamps, reproduced from [48].

2.1.3.2 Soft Lithography

Soft lithography, also called casting, is commonly used to develop elastomers for microfluidic applications [48–50]. The process is called soft because of the use of soft materials, notably PDMS. The starting point of the process is fabricating the PDMS stamp. Liquid PDMS is poured onto the master (usually SiO_2, Si_3N_4 or photoresist) and cured. After curing the PDMS sheet is peeled away from the master (Figure 2.2). Major soft lithography techniques include micro contact printing (μCP) and replica moulding (Figure 2.3) [50].

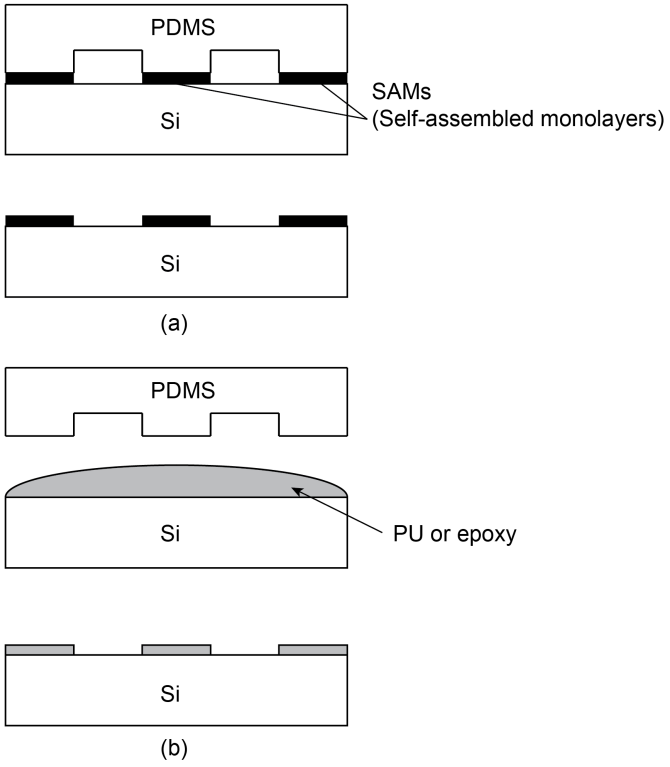

FIGURE 2.3: Schematic of soft lithography techniques: (a) Micro contact printing of SAMs; (b) Replica moulding of PU or epoxy, reproduced from [50].

2.1.3.3 Injection Moulding

Injection moulding has been developed for automated commercial manufacturing in the macroscopic world and it is also used for fabricating micron-scale features on polymeric materials (for instance, PMMA [51], PC [51] and COC [52, 53]). Figure 2.4 is a cross-sectional diagram of a typical injection moulding machine [29]. During injection moulding, polymer in the granulated form is fed into the plastifying unit and heated to above its melting temperature. The polymer melt is then compressed and injected into the mould cavities to form microfluidic channels [29, 54].

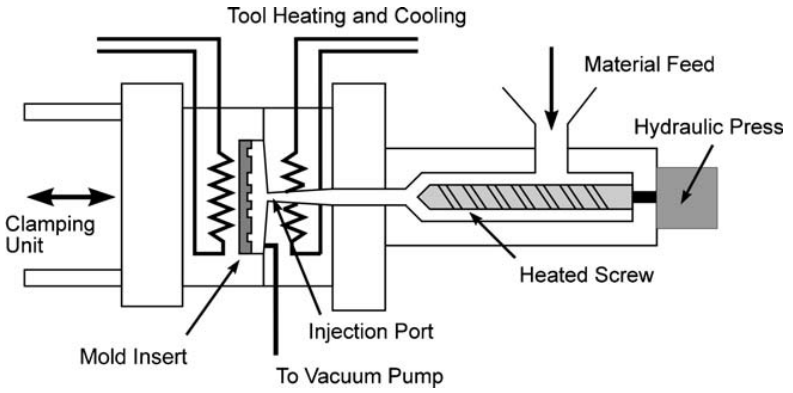

FIGURE 2.4: Schematic of an injection moulding machine [29].

2.1.3.4 Hot Embossing

Hot embossing is also called thermal embossing as opposed to ultraviolet (UV) embossing which uses UV light to fabricate UV-curable materials [55]. Figure 2.5 shows the principle of planar hot embossing of microfluidic channels. Hot embossing has advantages over other micro-fabrication techniques for its moderate cost of tools and equipment [56]. What stands out is that the hot embossing can be integrated with roll-to-roll technology to enable continuous manufacturing. Widely used materials for this method include polymethyl methacrylate (PMMA) with a T_g of $\sim$105 °C [37] and polycarbonate (PC) with a T_g of $\sim$150 °C [57]. The embossing force is in the order of 20 to 30 kN and the holding time is in the order of 1 minute [37, 57]. The aspect ratio can be as high as 20:1. De-embossing takes place after cooling below the polymer's T_g.

To adapt these replication techniques for research and industrial use, several issues should be considered, such as the process and equipment set up, the tooling costs and the cycle time, as shown in Table 2.1 [29]. The cycle time of soft lithography is normally from minutes to a few hours compared to minutes for hot embossing and from minutes to seconds for injection moulding. The initial equipment cost for injection moulding is the highest among these three replication techniques. Injection moulding has been widely used in commercial production, nevertheless, this replication method is limited in use for research institutions because of it being a difficult process to manage and set up equipment [46, 58]. Consequently, soft lithography and hot embossing are preferred in low- and medium-volume manufacturing and in academic research, while injection

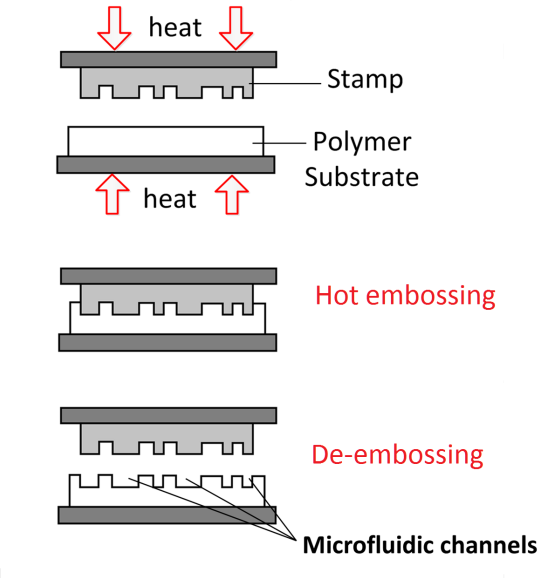

FIGURE 2.5: Schematic of planar hot embossing of microfluidic channels.

moulding has been more widely adopted for industrial applications, such as for the manufacture of point-of-care testing systems [29].

TABLE 2.1: Comparison of different microfabrication techniques, reproduced from [29].

Process	Equipment setup	Tooling costs	Cycle time	Geometrical flexibility	Production automation
Soft lithography	hours	$< \$2k$	min-hours	High	Not existed
Injection moulding	days	$\$20k - \$150k$	sec-min	High (3D)	High
Hot embossing	hours-days	$\$2k - \$15k$	min	Medium (2D)	Medium

2.1.3.5 Bonding

A variety of bonding processes have been developed to form closed channels on the polymer-based microfluidic chips [39, 59–62]. Polymers can be thermally bonded under pressure. Polymers or thick resists can be used to define bonds and channels. Other bonding techniques include adhesive bonding where adhesives are used to bond microfluidic chips [62], and solvent bonding where two polymer parts are combined by suitable solvents to form chemical bonds [60].

2.1.4 Roll-to-Roll (R2R) Hot Embossing

The roll-to-roll (R2R) replication techniques include R2R UV embossing and R2R hot embossing [30, 37]. The continuous replication process and the potential to integrate with other R2R processes (such as gravure or flexo printing and lamination [63, 64]) make R2R replication techniques more suitable for use in mass manufacturing. R2R UV embossing uses UV light to cure a photopolymer and R2R hot embossing uses heat and pressure to process a polymer. The R2R UV embossing does not require heating and pressing tools, however there are disadvantages such as limitation of film thickness, chemical resistance and optical properties.

The differences between conventional (planar) hot embossing and R2R hot embossing are summarised in Table 2.2 [37].

TABLE 2.2: Comparisons between conventional hot embossing and R2R hot embossing, reproduced from [37].

	Planar hot embossing	R2R hot embossing
Mould	Flat and rigid, typically a few millimetres thick	Metal shim mounted on to a roller, typically tens to hundreds of microns thick
Process	Pieces by piece	Continuous
Temperature	Mould undergoes a temperature cycle of heating and cooling	Mould does not undergo temperature cycle
Load	Cyclical force over an area	Constant nip pressure
De-embossing	In the direction perpendicular to the mould	Similar to peeling

2.1.4.1 Equipment Setup

An R2R hot embossing unit consists of an embossing roller and a counter pressure roller (see Figure 2.6). The nip between the embossing roller and the counter pressure roller provides the necessary nip pressure for the hot embossing process to take place.

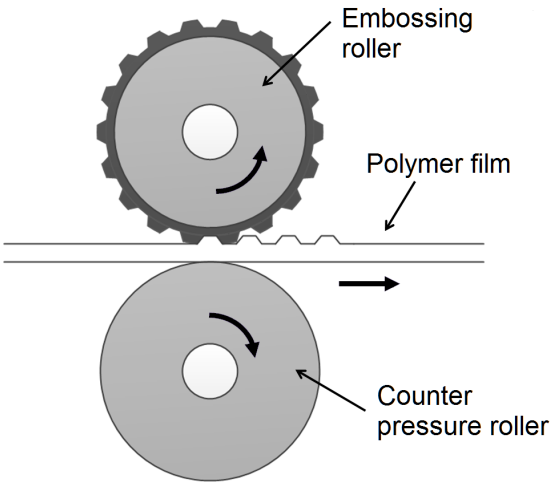

FIGURE 2.6: Schematic of R2R hot embossing.

2.1.4.2 Operation and Control Variables

The operation and control variables are similar to those in the conventional, planar hot embossing. The most important parameters are: temperatures (of the embossing roller and counter pressure roller), rolling speed and nip pressure, however there are a number of secondary variables including pre-heating time, stamp shape, dimension and orientation. These parameters are currently selected via trial experiments in order to achieve the best filling results. Depending on the properties of the material and the embossing equipment, the typical methods to increase the filling rate are to increase the embossing temperature and nip pressure, and lower the rolling speed. Current R2R hot embossing systems can hardly achieve complete mould filling, for the embossing time is relatively short and there is no holding stage as in conventional hot embossing. However, there are a number of ways to improve the embossing results at the current R2R hot embossing settings. The temperature of the embossing roller is the main parameter which relates to the thermo-mechanical behaviour of the material being embossed. The temperature of the counter pressure roller is usually lower than that of the embossing roller in order to quickly cool the polymer films after de-embossing.

2.1.4.3 Pros and Cons

The advantages of R2R hot embossed microfluidic devices (for example, the microfluidic mixer shown in Figure 2.7 [65]) are:

- Low cost: thermoplastic materials are cheap compared with conventional materials such as glass and silicon, allowing disposable chips to be made, which is suited for in-vitro diagnostic testing.
- High process repeatability: the replication tools for microfluidic chips can be repeatedly used.
- Integrated functionality: R2R hot embossing can be integrated with other R2R processing techniques such as R2R screen printing and R2R lamination.
- Parallel printing: the R2R hot embossing enables moulding multiple chips on the same polymer film.

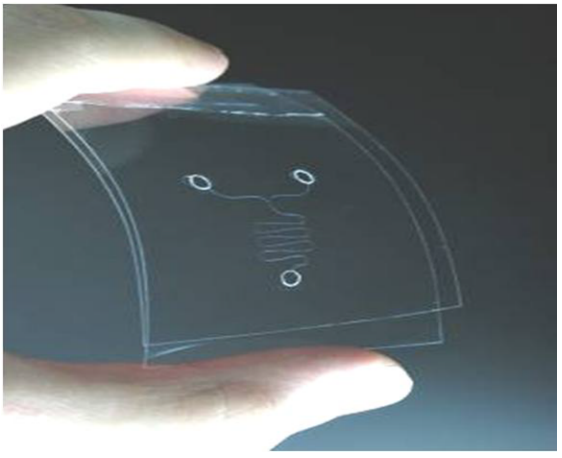

FIGURE 2.7: A R2R-hot-embossed microfluidic mixer [65].

The main disadvantage of R2R hot embossing compared to similar polymer microfabrication techniques is the limitation in heights and aspect ratios (ARs) of the microstructures on the embossed products, due to the rotating movement and the relatively short contact time between the embossing roller and the thermoplastic film. Nevertheless, R2R hot embossing has been a promising fabrication technique for making microfluidic chips,

and researchers have been developing strategies to complete the cycle of development including commercialisation of R2R-hot-embossed microfluidic devices.

2.1.4.4 Latest Developments

Equipment Development

Some early examples of R2R hot embossing equipment were reported by Jiang *et al.* [66], Ishizawa *et al.* [67] and Ng *et al.* [37]. In Jiang *et al.*'s work, micro-scale holes were fabricated on a copper roller by photolithography. The copper roller was used as the moulding roller and pressed by another hot roller under pneumatic forces. The authors also employed an extruder and slid-die in front of the embossing rollers so that PC films were fabricated and immediately fed into the two embossing rollers. This arrangement was unique as the fabrication process of thermoplastic film was integrated with the R2R hot embossing system. Microlens with an average diameter of 210 µm and a depth between 8 to 20 µm were fabricated.

Ishizawa *et al.* reported a hydraulic R2R embossing machine, including a roller which was wrapped with 50 µm-thick mould, another roller which acted as the counter pressure roller and a PET film was passed through between the two rollers. The rollers were heated to approximately 80-100 °C by infrared heaters. As a result, 10 µm diameter holes were fabricated on the polyethylene terephthalate (PET) films under the load of 3 kN.

A recent innovation in the roller heating method, induction heating, was reported by Yun *et al.* [68]. The induction heating is a non-contact heating process: heat was produced in the conductive material by the internal resistance of the material and the induced current. Yun *et al.* claimed that this heating system had a more even temperature distribution and cleaner working environment than that of the oil heated rollers. They performed R2R hot embossing experiments on polyethylene naphthalate (PEN) films ($T_g = 120$ °C), at an embossing temperature of 140 °C and a rolling speed of 0.8 m/min.

Liu *et al.* developed an infrared-assisted R2R hot embossing process in which polyethylene terephthalate (PET) and polycarbonate (PC) films were heated by IR radiation [69]. 150-µm-deep microstructures were embossed on both sides of the thermoplastic films. Another recent development of double-sided R2R hot embossing was published by Nagato *et al.* who demonstrated an iterative R2R hot embossing technique for fabricating multilayerd structures.

Parametric Study

The basic principle of a parametric study on the R2R hot embossing processes is to change only one parameter (such as the roller temperature, rolling speed and nip pressure) at a time and keep other parameters constant and identify the influences of process parameters on the shapes and dimensions of the embossed microstructures. One of the first parametric studies of R2R hot embossing process was reported by Ng *et al.* [37], who tested the effects of nip pressure, rolling speed and roller temperature on the embossed depth of PMMA films. The results showed that when raising the nip pressure from 1 bar to 5 bars the embossed depth was raised from around 0 to around 2 µm. The authors also claimed that the embossed depth increased when lowering the rolling speed from 35 mm/s to 1.5 mm/s, however the tendency was not clearly shown in the speed ranging from 35 to around 8 mm/s as the embossed depths were all below 2 µm and close to 0. Besides, they did not explain why there was a dramatic increase in the depth from ∼2 µm to ∼32 µm when the speed was lowered from ∼8 mm/s to 1.5 mm/s. The authors argued that the optimum roller temperature was ∼140 °C because at any temperatures they tested below or above 140 °C, the embossed depth was lower than that at ∼140 °C. However, a key problem with this argument is that each increment of temperature growth was 10 °C, while PMMA is very sensitive to temperature, especially at temperatures near its T_g. Therefore, a smaller temperature increment at temperatures near PMMA's T_g is required. Nevertheless, this parametric study has drawn a general conclusion on the effects of roller temperature, roller speed and nip pressure. This argument was later supported by Liu *et al.* [69], who reported that the depth of replicated ditches increased when nip pressure changed from 4 to 8 °C, and the ditch

depth decreased when rolling speed range was increased from 0.6 to 1.8 mm/s. Yeo *et al.* used a Box-Benhken [1] design matrix to determine three process parameters during the R2R hot embossing of PMMA: roller temperature, preheating temperature and pressure [70]. The normalised depth peaked at 6 bars of pressure, 110 °C of roller temperature and 105 °C of preheating temperature.

Some other existing studies have examined the effects of preheating, cooling and pattern density on the embossed depth [71–73]. In these studies, the preheating temperature was adjusted according to the thermal properties of the thermoplastic material and the process parameters such as the rolling speed and embossing temperature. In Kim *et al.*'s work, a position roller was placed at the front of the embossing rollers where an infrared heater was used to preheat the backside of the PMMA substrate. By changing the contact angle between the PMMA substrate and the embossing roller, the preheating time was increased from 9 to 18 seconds for a rolling speed of 0.5 m/min. An air injector cooled the PMMA substrate to room temperature after embossing. They found that substrate cooling had no influence on the variation of embossed depths, however an extended preheating time can significantly increase the embossed depth. Overheating the PMMA substrate forced it to go out of shape if the preheating time was set to over 20 s. In addition, they discovered that a lower pattern density moulds achieved better replication results.

Summary

Table 2.3 lists the recently developed micro R2R hot embossing processes, including the dimensions of embossed microchannels, maximum aspect ratio and maximum transfer rate. Note that the mould transfer rate is introduced as the ratio between the actual and designed feature depth, therefore 100% transfer rate does not indicate complete mould filling.

[1] A statistical method used in the design of experiments which requires three different factor values to run an experiment.

TABLE 2.3: Comparative study of recently developed R2R hot embossing processes.

Geometry	Material	Lateral size(µm)	Depth (µm)	Max. aspect ratio	Max. transfer rate	Reference
Holes	PC	220	20	0.09	71%	Jiang *et al.* [66]
Lines	PMMA	50	30	0.6	85%	Ng *et al.* [37]
Lines	PMMA	30-200	20	0.667	80%	Yeo *et al.* [70]
Lines	PEN	20-230	25	0.8	40%	Yun *et al.*[68]
Holes	COC	0.5-20	0.7	1.46	70%	Velten *et al.* [74]
Y-shape	CA	11.7-400	9	0.77	82%	Vig *et al.* [75]
U-shape	PMMA	60	46	0.77	58%	Liedert *et al.* [76]
Lines	COC,PVC	200	41.4	0.21	100%	Tsao *et al.* [77]
Y-shape, holes	PS,PMMA,PC	200	238	1.19	99%	Cheng *et al.* [78]
U-shape	PE,PP,COC	2000	110	0.06	97%	Zhang *et al.* [79]

Recent studies have successfully established the major equipment setup for R2R hot embossing processes. Some essential process parameters, such as embossing temperature, preheating time and temperature, rolling speed, pressure, have been identified. A number of R2R-hot-embossed devices have been used for LOAC applications, such as capillary electrophoresis (CE) [76, 80, 81], interconnected microreactor [82] and separation chips [75, 83]. There are a wide choice of geometries including lines, holes, U-shaped and Y-shaped channels. Most of the reported microstructures have a lateral size of tens to hundreds of microns and a depth of less than 100 µm, which are suitable for LOAC applications. The aspect ratios are mostly below 1, and the highest aspect ratio presented in Table 2.3 is 1.46. The transfer rate varies with different geometry designs and R2R equipment. Close to 1 transfer ratios have been achieved only at small aspect ratios (∼0.06) or large lateral size (∼200 µm). Moreover, there are several challenges which are rarely reported in literature:

1. Stamp/shim fabrication: the stamp/shim material and fabrication method need to be carefully chosen to get the best geometry accuracy and surface roughness which suitable for R2R hot embossing. The cost and lifetime of stamp/shim should also be considered for reducing the overall cost of R2R hot embossing.

2. Quality check: the quality of R2R-hot-embossed microstructures has been assessed only to a very limited extent, especially for the use of LOAC applications. Geometric defections and incomplete mould filling could both affect the performance of LOAC devices. Additional studies are necessary to assess the quality of microstructures.

3. Study of thermoplastics' thermo-mechanical behaviour: the thermoplastic film is heated and pressed to form a channel in the embossing process and peeled off from the stamp/shim in the de-embossing process. A systematic and theoretical analysis is required for understanding the thermo-mechanical behaviour of thermoplastics in R2R hot embossing. This thesis focuses on this challenge.

2.2 Thermo-Mechanical Behaviour Studies of Thermoplastics in Hot Embossing and Their Applications to Hot Embossing

2.2.1 Characteristics of Thermoplastic Materials

Thermoplastic polymer materials consist of macromolecules with no cross-linking [84]. They are either randomly or partly coiled. Randomly coiled thermoplastics are in a glassy state and referred to as amorphous thermoplastics. The other group is called semicrystalline thermoplastics. The molecular arrangements of amorphous and semicrystalline thermoplastics are described in Figure 2.8. There are crystalline, rigid amorphous and mobile amorphous regions in the polymer's molecular arrangements. These regions relate to the characteristic temperatures within the material such as the melting temperature of the crystalline, T_m. The glass transition temperature, T_g, is raised by the mobile amorphous regions. The relationship between T_m and T_g has been found to be [40]:

$$T_g \cong 0.66 \cdot T_m \tag{2.2}$$

where T_g and T_m are in Kelvin.

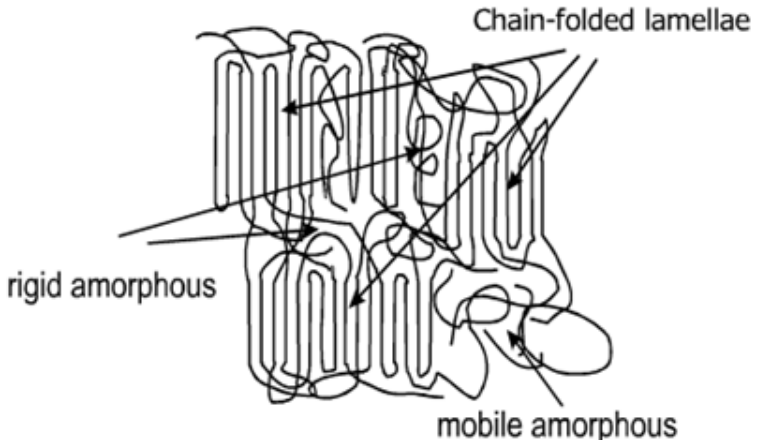

FIGURE 2.8: Amorphous and semicrystalline molecular arrangements [40].

Polymethyl methacrylate (PMMA) is a transparent amorphous thermoplastic, also known by its trade names Plexiglas, Acrylite, Lucite and Perspex. It is a light-weight material with a density of 1.16 to 1.20 g/cm^3. The skeletal formula of PMMA is $(C_5O_2H_8)_n$ and its structure is shown in Figure 2.9.

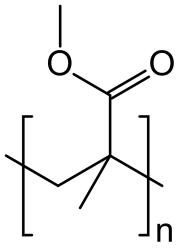

FIGURE 2.9: Skeletal formula of the PMMA repeating unit.

2.2.2 Existing Simulation Approaches

Many attempts have been made to model the planar hot embossing processes, and those models have included the use of fluid-based theories and solid-based theories. These theories are crucial to developing appropriate numerical methods for use within simulations of the hot embossing processes on thermoplastic materials. Relevant thermoplastic materials include polymethyl methacrylate (PMMA), polycarbonate (PC), polystyrene (PS), polypropylene (PP), cyclic olefin polymer (COP) and cyclic olefin copolymer (COC).

2.2.2.1 Newtonian Fluid

Some early studies include a Newtonian fluid to describe the squeezing flow of thermoplastics during hot embossing. A simple squeezing flow model is based on two flat, circular disks with a radius of R, applied by a force of F. The thickness of residual layer under the moulding force F of the elapsed time t is:

$$h(t) = \sqrt{\frac{3\pi R^4 \eta}{16Ft}} \tag{2.3}$$

where η is the viscosity of the fluid.

The residual layer can be defined by F and t:

$$h(t) \propto \sqrt{\frac{1}{Ft}} \tag{2.4}$$

An example of using the Newtonian fluid to simulate hot embossing is reported by Jeong *et al.* [85]. They have used the commercial simulation program, CFD-ACE, to track the deforming polymer interface during nanoimprinting. A major problem with this model is that it is only limited to small shear velocities when the fluid viscosity is constant. The shear-thinning liquid could be an alternative simulation approach, as discussed in the following section.

2.2.2.2 Shear-Thinning Fluid

The shear thinning behaviour has been used to describe a polymer melt at high velocities when fluid viscosity is not constant and Newtonian flow is not valid. At this stage, when the shear velocity increases, the corresponding shear stress increases in a degressive behaviour. The viscosity of a polymer melt decreases with increasing temperature and increases with increasing pressure. One of the most well-known mathematical description of shear thinning is the Carreau-Yasuda model, which has the form: [86, 87]:

$$\eta(\dot{\gamma}) = \eta_\infty + (\eta_0 - \eta_\infty)[1 + (\lambda\dot{\gamma})^a]^{\frac{n-1}{a}} \tag{2.5}$$

where $\eta(\dot{\gamma})$ is the viscosity, $\dot{\gamma}$ is the shear rate, η_0 is the zero-shear-rate viscosity, η_∞ is the infinite-shear-rate viscosity, λ is the relaxation time, n is a power-law index that characterise the degree of shear thinning, a is a constant that sets the size and curvature of the crossover region between Newtonian and shear-thinning behaviour.

Juang *et al.* have tested the dynamic complex viscosity of PVB (polyvinyl chloride), PMMA and PC at different temperatures and strain rates and applied the Carreau-Yasuda model to characterise the dynamic complex viscosity [88]. Then they used the software DEFORM to simulate the flow pattern in isothermal hot embossing.

Many fluid-based simulations discussed above have been proved to be close to experimental values [85, 88, 89], however, the actual hot embossing typically takes place below a thermoplastic material's melting temperature where its thermo-mechanical behaviour are more complex than that in the fluid-based models. Some recent simulations focus on solid mechanics which is based on the finite element (FE) method to describe a thermoplastic material's behaviour at temperatures close to its T_g. Two-dimensional models of simple geometries and plane-strain elements have been employed in those published works, while more complex geometries and the use of three-dimensional simulations have rarely been reported. For small deformations, linear elastic, linear viscoelastic and viscoplastic models have been employed to describe the thermoplastics' behaviour. For large deformations, hyperelastic and some novel constitutive models are reported.

2.2.2.3 Linear Elastic Model

Elasticity theory is the most simple theory used for modelling the material's mechanical behaviour at small deformations. If tested in tension a linear elastic material specimen will return to its original shape after the load is removed. For linear solids, the stress σ is a linear function of strain and the strain ε is independent of the rate or load history. The relationship between σ and ε in uniaxial loading is defined by Hooke's law:

$$\sigma = E\varepsilon \tag{2.6}$$

where E is Young's modulus, the slope of the stress versus strain curve in a tension test.

For an isotropic, linear solid, the Hooke's law in multiaxial loading can be expressed with thermal effects as below:

$$\begin{bmatrix} \varepsilon_{11} \\ \varepsilon_{22} \\ \varepsilon_{33} \\ \gamma_{12} \\ \gamma_{13} \\ \gamma_{23} \end{bmatrix} = \frac{1}{E} \begin{bmatrix} 1 & -\nu & -\nu & 0 & 0 & 0 \\ -\nu & 1 & -\nu & 0 & 0 & 0 \\ -\nu & -\nu & 1 & 0 & 0 & 0 \\ 0 & 0 & 0 & 2(1+\nu) & 0 & 0 \\ 0 & 0 & 0 & 0 & 2(1+\nu) & 0 \\ 0 & 0 & 0 & 0 & 0 & 2(1+\nu) \end{bmatrix} \begin{bmatrix} \sigma_{11} \\ \sigma_{22} \\ \sigma_{33} \\ \sigma_{12} \\ \sigma_{13} \\ \sigma_{23} \end{bmatrix} \tag{2.7}$$

where ε_{ij} is normal strain, γ_{ij} is shear strain, σ_{ij} is stress, ν is Poisson's ratio, the ratio of lateral strain to longitudinal strain.

Using index notation, this expression can be re-written as below:

$$\varepsilon_{ij} = \frac{1+\nu}{E}\sigma_{ij} - \frac{\nu}{E}\sigma_{kk}\delta_{ij} + \alpha\Delta T\delta_{ij} \tag{2.8}$$

where δ_{ij} is the Kronecker delta symbol:

$$\delta_{ij} = \begin{cases} 1, & i = j \\ 0, & i \neq j \end{cases} \tag{2.9}$$

2.2.2.4 Linear Viscoelastic Model

The response of a typical thermoplastic material is strongly dependent on temperature and rate [90]. At temperatures below T_g the material behaves like glass with stiff mechanical response. Near T_g there is a dramatic drop in the material's modulus and the stress in the material is strongly rate-dependent. This regime is referred to as the viscoelastic regime. At temperatures above T_g, the material shows rubbery behaviour with little dependency on the strain rate, and the modulus increases with temperature. In general, these regimes of mechanical behaviours (glassy, viscoelastic and rubbery) are

identified at different temperature ranges (below, near and above T_g) and each regime depends on the molecular structure of the material. The viscoelastic behaviour can be measured by applying either a step load or a sinusoidal load. The use of sinusoidal load is introduced here as it will be discussed further in the dynamic mechanical analysis (DMA). For a dynamic, sinusoidal load, the periodic strain is:

$$\epsilon = \epsilon_0 \exp(i\omega t) \tag{2.10}$$

where t is time, ω is the frequency of oscillation.

And the dynamic stress response is:

$$\sigma = \sigma_0 \exp(i(\omega t + \psi)) \tag{2.11}$$

where ψ is the phase lag of strain with respect to stress.

The complex modulus E^*

$$E^* = E' + iE'' \tag{2.12}$$

where E' and E'' are the real and imaginary parts of the complex relaxation modulus E. The complex relaxation modulus is deduced from the generalised Maxwell model, which is represented by a parallel network of the Maxwell elements (a Maxwell element is an elastic spring and a viscous dashpot connected in series) (Figure 2.10). Each parallel branch is identified with a spring constant E_i, and a relaxation time η_i. The model consists of n number of Maxwell elements.

$$E(t) = E_\infty + \sum_{i=1}^{n} E_i e^{-(t/\eta_i)} \tag{2.13}$$

where $E(t)$ is the complex modulus, t is the relaxation time and E_∞ is

$$E_\infty = \lim_{t \to +\infty} E(t) \tag{2.14}$$

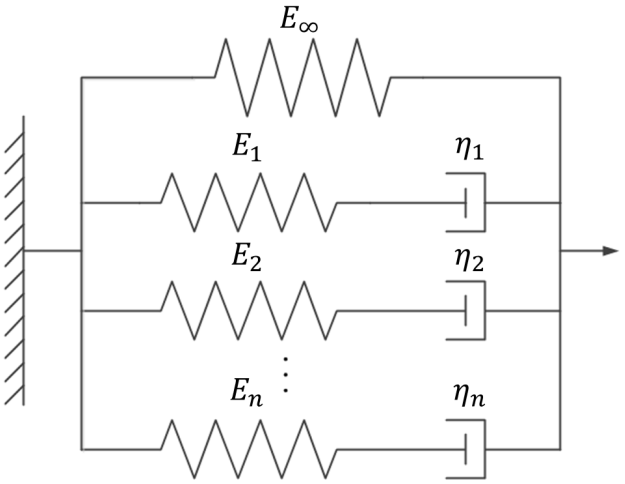

FIGURE 2.10: Schematic of the generalized Maxwell model.

The constitutive relation is defined as:

$$\sigma(t) = \epsilon_0 E(t) + E(t-\xi)\frac{d\epsilon}{d\xi} \tag{2.15}$$

The loss factor $\tan\delta$ is expressed as:

$$tan\delta = \frac{E''}{E'} \tag{2.16}$$

And the storage and loss moduli can be expressed as:

$$E'(\omega) = E_0\left[1 - \sum_{i=1}^{N} e_i\right] + E_0 \sum_{i=1}^{N} \frac{e_i \eta_i^2 \omega^2}{1 + \eta_i^2 \omega^2} \tag{2.17}$$

$$E''(\omega) = E_0 \sum_{i=1}^{N} \frac{e_i \eta_i \omega}{1 + \eta_i^2 \omega^2} \tag{2.18}$$

where a dimensionless complex modulus e_i is defined as:

$$e_i = \frac{G_i}{G_0} \tag{2.19}$$

It should be noted that the temperature-dependence of a viscoelastic material can be defined over a large time scale, although no single experiment is able for such a range. The temperature-dependence is studied by examining a certain range of temperate-dependent data at a short period time and use the time-temperature superposition (TTS) principle to predict the material responses in the whole temperature and time range.

The well-known Willams-Landel-Ferry (WLF) equation was developed based on the free volume theory [91]. According to the theory, a free volume change results in a mobility change for the molecules within a polymeric material and therefore its temperature-dependent mechanical properties. The WLF equation can be applied to define the shift function which describes the temperature-dependent mechanical properties with reference to those at the glass transition temperature. The shift factor α_T is given by:

$$\log(\alpha_T) = \frac{-C_1(T - T_g)}{C_2 + (T - T_g)} \tag{2.20}$$

where C_1 and C_2 are material constants.

Linear viscoelastic models have been widely used in the simulation of hot embossing process [80, 92–95]. The linear viscoelastic models are suitable for simulating the planar hot embossing in which the thermoplastic material completely fills in the embossing mould. However, neither hyperelasticity theory nor viscoelasticity theory defines the material response caused by plastic deformation, which is an essential part in simulating the R2R hot embossing process. Plastic theories, especially the viscoplastic theory, could be used to define the rate-dependent inelastic behaviour behaviour.

2.2.2.5 Elastic-Viscoplastic Model

The two-layer viscoplastic model is a viscoplastic model which consists of an elastic-plastic network in parallel with an elastic-viscous network (Figure 2.11) [90]. K_v and K_p are the elastic and plastic modulus of the two networks, respectively, m is the total time or equivalent strain order, σ_y is the initial yield stress, H' is the hardening modulus,

A and n are Norton-Hoff rate parameters. The elastic-plastic network represents the time-independent material behaviour and is based on the von Mises yield condition, while the elastic-viscous network represents the time-dependent material behaviour.

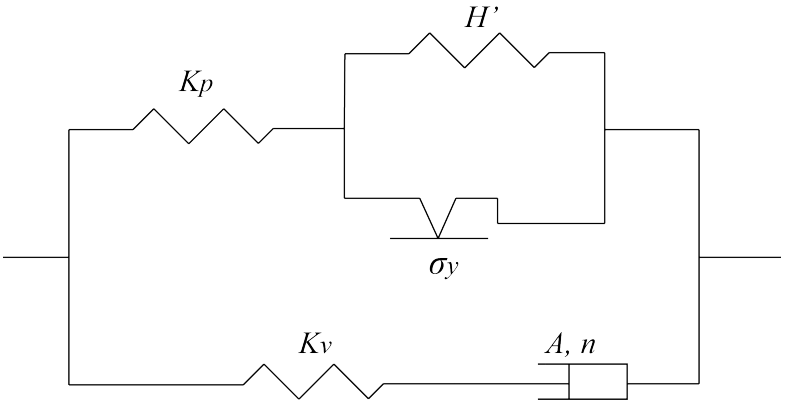

FIGURE 2.11: Schematic of the two-layer viscoplastic model.

The ratio of the elastic modulus of the elastic-viscous network (K_v) to the total modulus ($K_p + K_v$) is:

$$f = \frac{K_p}{K_p + K_v} \tag{2.21}$$

The stress-strain relation in the elastic-plastic network is defined as:

$$\sigma_p = \frac{\sigma_y}{\varepsilon_y^{n_1}}(\varepsilon_y + \varepsilon_p)^{n_1} = \sigma_y(1 + \frac{K_p}{\sigma_y}\varepsilon_p)^{n_1} \tag{2.22}$$

where n_1 is the work hardening exponent.

The viscous behaviour is assumed to be governed by the Norton-Hoff rate law, which is:

$$\dot{\varepsilon}_v = A\sigma_v^n \tag{2.23}$$

The total stress for a given total strain ε is:

$$\sigma = A^{-\frac{1}{n}}\dot{\varepsilon}^{\frac{1}{n}} + \sigma_y + H'\varepsilon \tag{2.24}$$

The related work conducted by Abdel-Wahab *et al.* have demonstrated good correlations between uniaxial tensile test data and simulations for PMMA [96]. However, the model

was validated for the temperature range below T_g, however did not include strain rate dependence for PMMA.

2.2.2.6 Hyperelastic Model: A Large-Strain Elastic Model

The rubbery regime above a thermoplastic material's T_g can be described approximately by the hyperelasticity theory. The hyperelasticity theory is a large-strain theory for ideally elastic material for which the stress-strain relationship is specified by the strain energy density [90]:

In large-strain theories, the deformation gradient tensor $\mathbf{F}$ is the derivative of the deformed vector $\mathbf{x}$ vector with respect to its reference vector $\mathbf{X}$ of the same point:

$$\mathbf{F} = F_{ij} = \delta_{ij} + \frac{\partial u_i}{\partial x_j} \tag{2.25}$$

The left Cauchy-Green deformation tensor is:

$$\mathbf{B} = \mathbf{F} \cdot \mathbf{F}^T \quad B_{ij} = F_{ik}F_{jk} \tag{2.26}$$

Invariants of $\mathbf{B}$:

$$I_1 = \text{trace}(\mathbf{B}) = B_{kk} \tag{2.27}$$

$$I_2 = \frac{1}{2}(I_1^2 - \mathbf{B} \cdot \mathbf{B}) = \frac{1}{2}(I_1^2 - B_{ik}B_{ki}) \tag{2.28}$$

$$I_3 = \text{det}\mathbf{B} = J^2 \tag{2.29}$$

An alternative set of invariants of $\mathbf{B}$:

$$\bar{I}_1 = \frac{I_1}{J^{2/3}} = \frac{B_{kk}}{J^{2/3}} \tag{2.30}$$

$$\bar{I}_2 = \frac{I_2}{J^{4/3}} = \frac{1}{2}(\bar{I}_1^2 - \frac{B_{ik}B_{ki}}{J^{4/3}}) \tag{2.31}$$

$$J = \sqrt{\text{det}\mathbf{B}} \tag{2.32}$$

The strain energy density W is specified as a function of deformation gradient tensor $\mathbf{F}$ and for an isotropic material:

$$W(\mathbf{F}) = U(I_1, I_2, I_3) = \bar{U}(\bar{I}_1, \bar{I}_2, J) \tag{2.33}$$

The stress-strain relationship can be calculated from the strain energy density:

$$\begin{aligned}\sigma_{ij} = \frac{1}{J}F_{ik}\frac{\partial W}{\partial F_{jk}} = \frac{2}{J^{5/3}}(\frac{\partial \bar{U}}{\partial \bar{I}_1} + \bar{I}_1\frac{\partial \bar{U}}{\partial \bar{I}_2})B_{ij} \\ - \frac{2}{3J}(\bar{I}_1\frac{\partial \bar{U}}{\partial \bar{I}_1} + 2\bar{I}_2\frac{\partial \bar{U}}{\partial \bar{I}_2})\delta_{ij} - \frac{2}{J^{7/3}}\frac{\partial \bar{U}}{\partial \bar{I}_2}B_{ik}B_{kj} + \frac{\partial \bar{U}}{\partial J}\delta_{ij}\end{aligned} \tag{2.34}$$

Some well-known hyperelastic models in specific forms of the strain energy density are listed below: The generalised neo-Hookean model is related to $\bar{I}_1$ [97]:

$$\bar{U} = \frac{\mu_1}{2}(\bar{I}_1 - 3) + \frac{K_1}{2}(J-1)^2 \tag{2.35}$$

where μ_1 and K_1 are shear and bulk modulus for small deformations.

In the Mooney-Rivlin model, the strain energy density is a linear combination of barI$_1$ and barI$_2$. The generalised Mooney-Rivlin model [98] is expressed as:

$$\bar{U} = \frac{\mu_1}{2}(\bar{I}_1 - 3) + \frac{\mu_2}{2}(\bar{I}_2 - 3) + \frac{K_1}{2}(J-1)^2 \tag{2.36}$$

where μ_1, μ_2 and K are material properties. For small deformations, the shear modulus and bulk modulus are $\mu = \mu_1 + \mu_2$, $K = K_1$.

The generalised polynomial form of the strain energy potential is:

$$\bar{U} = \sum_{i+j=1}^{N} C_{ij}(\bar{I}_1 - 3)^i(\bar{I}_2 - 3)^j + \sum_{i=1}^{N}\frac{K_i}{2}(J-1)^{2i} \tag{2.37}$$

where C_{ij} and K_i are material properties. For small deformations, the shear modulus and bulk modulus are $\mu = 2(C_{01} + C_{10})$, $K = 2K_1$.

The form of the Yeoh strain energy potential is [99]:

$$\bar{U} = \sum_{i=1}^{3} C_{i0}(\bar{I}_1 - 3)^i + \sum_{i=1}^{3} \frac{K_i}{2}(J-1)^{2i} \tag{2.38}$$

where C_{i0} and K_i are material properties.

In the Arruda-Boyce model, strain energy density is [100]:

$$\bar{U} = \mu\{\frac{1}{2}(\bar{I}_1 - 3) + \frac{1}{20\beta^2}(\bar{I}_1^2 - 9) + \frac{11}{1050\beta^4}(\bar{I}_1^3 - 27) + \dots\} + \frac{K}{2}(J-1)^2 \tag{2.39}$$

where μ, K, β are shear and bulk modulus for small deformations.

For the hyperelastic models above, the material parameters can be estimated by fitting the results of uniaxial tensile tests. One approach is to fit shear modulus at small strains and select the remaining parameters at a large stretch. For the Marlow model, it is assumed that the strain energy density is independent of the second stretch invariant. No curve fitting is required as the material response is determined from uniaxial test data only.

The form of strain energy potential in the Marlow Model is [101]:

$$\bar{U} = \int_0^{\lambda_T(I)-1} T(\varepsilon)d\varepsilon \tag{2.40}$$

where $T(\varepsilon)$ is the nominal uniaxial stress and $\lambda_T(I)$ is the uniaxial stretch.

There have been a number of existing simulations in which a hyperelastic model is employed to describe the nonlinear elastic behaviour for thermoplastic materials above their T_g (Neo-Hookean [102], Mooney-Rivlin [103, 104]). Hyperelastic models have also been adopted to define the elastic part of many other constitutive models [95, 105, 106].

2.2.2.7 Dupaix-Boyce Elastic-Viscoplastic Model

The model is an example of a large-strain elastic-viscoplastic theory which consists of a parallel connection of two spring-dashpot branches. Each branch has an elastic

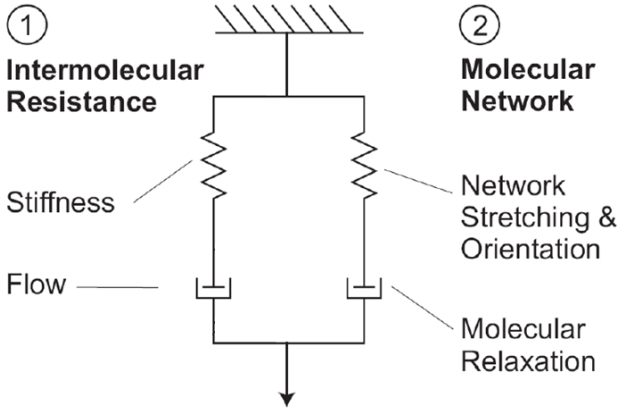

FIGURE 2.12: Schematic of the Dupaix-Boyce elastic-viscoplastic model [107].

spring, which represents the energy stores in the material, and a viscoplastic dashpot, which represents the energy dissipation. A schematic of such model (Dupaix-Boyce model) is shown in Figure 2.12 [107]. The spring and dashpot on the left represent the intermolecular resistance between adjacent polymer parts. The intermolecular resistance is the main cause of the initial stress of the material and a finite stress in the flow, and the yield stress [107]. The spring on the right represents the network stretching and orientation of the molecular network which causes the polymer to stiffen at large strains. The highly nonlinear dashpot represents molecular relaxation which occurs at higher temperatures or lower strain rates. Once the stress is increased to the threshold of the elastic level, the molecular chain network breaks and the material exhibits viscous behaviours. The deformation gradient is divided into two parts: the elastic part $\mathbf{F}_i^e$ and the plastic part $\mathbf{F}_i^e$. i represents either $\mathbf{I}$ (intermolecular resistance) or $\mathbf{N}$ (molecular network resistance). The velocity gradient, Li, is defined as:

$$\mathbf{L}_i = \dot{\mathbf{F}}_i \mathbf{F}_i^{-1} = \dot{\mathbf{F}}_i^e \mathbf{F}_i^{e-1} + \mathbf{F}_i^e \dot{\mathbf{F}}_i^p \mathbf{F}_i^{p-1} \mathbf{F}_i^{p-1} = \mathbf{L}_i^e + \tilde{\mathbf{L}}_i^p \tag{2.41}$$

The total deformation gradient equals the deformation gradients of each side of the parallel branches. Therefore the deformation gradient $\mathbf{F}$ is:

$$\mathbf{F} = \mathbf{F_I} = \mathbf{F_N} \tag{2.42}$$

$$\mathbf{F}_i = \mathbf{F}_i^e \mathbf{F}_i^p \tag{2.43}$$

The deformation gradient is divided into two parts: the elastic part $\mathbf{F}_i^e$ and the plastic part $\mathbf{F}_i^e$. i represents either $\mathbf{I}$ (intermolecular resistance) or $\mathbf{N}$ (molecular network resistance). The velocity gradient $\mathbf{L_i}$ is defined as:

$$\mathbf{L}_i = \dot{\mathbf{F}}_i \mathbf{F}_i^{-1} = \dot{\mathbf{F}}_i^e \mathbf{F}_i^{e-1} + \mathbf{F}_i^e \dot{\mathbf{F}}_i^p \mathbf{F}_i^{p-1} \mathbf{F}_i^{p-1} = \mathbf{L}_i^e + \tilde{\mathbf{L}}_i^p \tag{2.44}$$

The plastic velocity gradient consists of a symmetric plastic rate of stretching and an antisymmetric plastic spin: $\tilde{\mathbf{L}}_i^p = \tilde{\mathbf{D}}_i^p + \tilde{\mathbf{W}}_i^p$ The antisymmetric plastic spin is taken zero, and rate of plastic stretching is:

$$\tilde{\mathbf{D}}_i^p = \dot{\gamma}_i^p \mathbf{N}_i \tag{2.45}$$

where $\mathbf{N}_i$ is the normalized deviatoric stress, and γ_i^p is the plastic strain rate. The total stress of the model is:

$$\mathbf{T} = \mathbf{T_I} + \mathbf{T_N} \tag{2.46}$$

The stress on the intermolecular part is:

$$\mathbf{T}_\mathrm{I} = \frac{1}{\mathrm{J_I}} \mathrm{L^e} [\ln \mathbf{V_I^e}] \tag{2.47}$$

where $\mathrm{J_I}$ is the volume change, $\mathrm{L^e}$ is the fourth order tensor of elastic constants, and $\mathbf{V_I^e}$ is the left stretching tensor. The shear modulus can be calculated as:

$$\mu = \frac{1}{2}(\mu_g + \mu_r) - \frac{1}{2}(\mu_g - \mu_r) \tanh(\frac{5}{\Delta T}(T - T_g)) + X_g(T - T_g) \tag{2.48}$$

where μ_g is the modulus in the glassy region, μ_r is the modulus in the rubbery region, ΔT is the temperature range of glass transition, T_g is the glass transition temperature, X_g is the slope outside the glassy region.

The glass transition temperature is strain rate dependent:

$$T_g = \begin{cases} T_g^* : & \dot{\gamma}_I^P < \dot{\gamma}_{\text{ref}} \\ \xi \log \frac{\dot{\gamma}_I^P}{\dot{\gamma}_{\text{ref}}} + T_g : & \dot{\gamma}_I^P \geq \dot{\gamma}_{\text{ref}} \end{cases} \tag{2.49}$$

where T_g^* is a reference transition temperature, ξ is a material constant, $\dot{\gamma}_{\text{ref}}$ is a reference strain rate.

The plastic strain range in the intermolecular resistance I is:

$$\dot{\gamma}_I^P = \dot{\gamma}_{0I} \exp[-\frac{\Delta \text{G}(1 - \tau_I/s)}{kT}] \tag{2.50}$$

where ΔG is the activation energy, s is the shear resistance, k is Boltzmann's constant, and T is absolute temperature. The stress on the molecular network is:

$$\mathbf{T}_N = \frac{1}{J_N} \frac{\nu kT}{3} \frac{\sqrt{N}}{\lambda_{ch}} \mathbf{L}^{-1} \frac{\lambda_{ch}}{\sqrt{N}} [\bar{\mathbf{B}}_{\text{N}}^e - (\lambda_{ch})^2 \mathbf{I}] \tag{2.51}$$

where ν is chain density, N is number of rigid links, $\mathbf{L^{-1}}$ is the inverse Langevin function, λ_{ch} is chain stretch.

The Dupaix-Boyce model described both elastic and viscoplastic responses for the thermoplastic materials. This model can be implemented in the FE package, Abaqus, by writing a user-defined subroutine (UMAT/VUMAT). The main drawback of this model is that it includes more than 10 material constants which are calibrated from the test data.

2.2.3 Applications to Hot Embossing

2.2.3.1 Simulations of Planar Hot Embossing

Numerical simulations of planar hot embossing are well documented, however, the simulations of R2R hot embossing are rarely reported in literature. The simulation processes

were mostly investigated in the embossing/moulding step when the thermoplastic material fills in the microcavities of the stamp, and the de-embossing/de-moulding step when the thermoplastic material is released from the stamp. For the microstructured parts, the stamp was modelled as two-dimensional or three-dimensional geometry with microstructures, and it was assumed as a rigid part with no deformations during the embossing and de-embossing steps. Commercial software and finite element programs were often used for simulating such steps. The following section reviews the literature related to simulations of hot embossing.

An early example of simulating the embossing and de-embossing processes was reported by Worgull *et al.* [92]. They empolyed MOLDFLOW (injection and compression moulding simulation software) to simulate the embossing step and ANSYS (finite element software) to simulate the de-embossing step. For the embossing step, the distribution of the polymer layer was similar to that in the injection moulding. For the de-embossing process, the simulation was based on a viscoelastic model for the material PMMA. The heat capaciy of the thermoplastic material was determined as a function of temperature by a DSC test. In-plane stress distribution in the microstructures were calculated.

Jena *et al.* employed a viscoelastic model (generalised Maxwell model) with WLF temperature dependance for the hot embossing process on COC [95]. They performed dynamic rhelogical measurements at temperatures from 20 °C above T_g to 60 °C above T_g. The test data of complex modulus versus frequency was fitted to the Prony series, and a master curve was made by shifting the curves at different temperatures. The simulation results were close to the experimental resutls in terms of the profiles of the embossed microchannel. However, the model lacked plastic/viscoplastic components which is essential in the de-embossing stage.

Ames *et al.* implemented a thermo-mechanically coupled theory with a user subroutine in Abaqus/Explicit [108] to model the response of PMMA and COC at temperatures from room temperature to T_g, and also continuously across T_g. They simulated the microchannels embossed at 90 and 130 °C and claimed that the predicted results agreed well with the experimental results. This method considered both elastic and viscoplastic

properties in the constitutive model, and could model material responses from temperatures below T_g and through the glass transition.

A method alternative to the finite element modelling to simulate the embossing of PMMA, PC and COC was introducted by Taylor *et al.* [109]. The topography was calculated by convolving an iteratively found contact pressure distribution with a point-load response. A linear Kelvin-Voigt model was employed to describe the viscoelastic behaviour. They designed a stamp with quasi-periodic patterns and simulated the topographies of PMMA embossed using the the convolution method. Peak penetrations simulations for PMMA embossed at 110 to 130 °C showed modest agreement with the experimental results. This method had the advantage of short execution time (less than 2 seconds) however did not capture the geometrical and material nonlinearities. Another drawback of this simulation approach was that the aspect ratio of microchannels was limited to less than 1.

Jena *et al.* have studied the patterns 0°, 45°, 90°, 135° to the direction of polymer web registration [110]. They claimed that the microfluidic channels along the direction of polymer chain orientation were easy to replicate than those across the polymer chain orientation. However, they also stated that the polymer chain orientation may be developed in the replication process, such as injection moulding. Therefore polymer orientation should be considered for the anisotropic injection-moulded polymers.

The demoulding/de-embossing process has been studied by [111–114], in which the de-embossing force is the main cause of defects. It has been suggested that the crack should be initiated far way from features for better demoulding results.

For the previous simulations of planar hot embossing, efective results have been discovered in incomplete filling [89], shape recovery [115, 116], fracture caused by de-embossing force [111, 113]. All the simulations presented above have been based on these assumptions: the mould and thermoplastic material are uniformly heated, and all stamp surfaces have uniform roughness, as a result, the validation of such simulations should be considered under all these boundary conditions.

2.2.3.2 Simulations of R2R Hot Embossing

Although there are many numerical studies on the conventional hot embossing, only a few works in literature demonstrate the simulation for R2R hot embossing [94, 117].

Deng *et al.*'s work focused on simulating the R2R hot embossing process of PVC films. They simulated micro 'pyramid' features of 70 µm deep were embossed on a PVC film at the feeding speed of 0.4 m/min, a loading force of 500 N and temperatures from 100 to 160 °C. A 3D model was created, in which the two rollers were assigned to elastic-plastic property and the PVC film was assigned to linear viscoelasticity. Additionaly, heat transfer from the roller to the top surface of the PVC film was introduced in the FE model. Silimarily, Sahli *et al.* made a 3D model of a COC layer between two rollers, however, did not incorporate any thermal properties for the model parts.

A closer look to the literature on simulations of R2R hot embossing, however, reveals of a number of shortcomings. First, the material model was not always applicable for the whole R2R hot embossing process, where temperature rises from below T_g to above T_g. Second, these studies have not been experimentally validated and the feature dimensions are not related to the ranges reported in recent R2R hot embossing experiments. This thesis will introduce a more effective method to simulate the R2R hot embossing.

2.3 Conclusions

In this chapter, we have introduced the techniques for fabricating polymer-based microfluidic devices, including injection moulding, hot embossing, thermoforming, soft lithography and bonding. We have reviewed the theories to describe the thermo-mechanical behaviour of thermoplastics in these fabrication techniques. To our knowledge, although these theories have been adopted in the studies of planar hot embossing, they have rarely been studied directly in R2R hot embossing. Moreover, no research to date has systematically studied the R2R hot embossing by analysing the thermo-mechanical behaviour of thermoplastic materaials and how the behaviour is affected by process parameters of

R2R hot embossing. To overcome the problem, we propose a more general solution to study the R2R hot embossing.

Chapter 3

Mechanical Characterisation of PMMA

3.1 Introduction

This chapter introduces the methodology for determining the thermo-mechanical behaviour of PMMA, which includes dynamic mechanical analysis (DMA) and tensile tests. The results of these tests have been calibrated and verified to existing constitutive models so that we can use the finite element method to simulate the R2R hot embossing process.

3.1.1 Introduction to Dynamic Mechanical Analysis (DMA)

Dynamic mechanical analysis (DMA) is a technique used to measure the time-dependent mechanical behaviour of materials and is widely used to test their viscoelastic properties often as a function of temperature and frequency. A DMA test machine, also known as a dynamic mechanical analyser, has wider temperature range and strain rate range than those applied in typical compressive and tensile tests. The dynamic mechanical analyser applies a sinusoidal stress to a sample, allowing the material's response to stress, temperature, frequency and other values to be studied. In DMA testing storage

modulus (G') and loss modulus (G'') values are measured as a function of temperature or frequency, and the loss factor ($\tan\delta$) is calculated as the ratio between the loss modulus and storage modulus. Storage modulus (G') and loss modulus (G'') are the technical terms which are used to describe the elastic and viscous portion of the material. Figure 3.1 shows some typical moduli curves obtained using in DMA. In this example the material's thermal-mechanical plateau is divided into four regions: glassy, glass transition, rubbery and flow regions, each identified by the change of storage modulus (G'), loss modulus (G'') or loss factor ($\tan\delta$). At low temperatures both G' and G'' does not change significantly (G' is close to 1 GPa and G'' is close to 10 MPa). This region is the glassy region. In the next region (glass transition range), G' decreased dramatically to around 1 MPa, while G'' rises to near 1 GPa and then drops to 1 MPa. In the rubbery plateau G' decreases slightly in the moduli range around 1 MPa, while G'' decreases slightly in the moduli range around 100 kPa. The glass transition range is the region where hot embossing is performed [30]. It can be seen from the figure that the loss modulus and loss factor peak within this region, while the storage modulus decreases by several decades. From this type of graph the glass transition temperature (T_g) can be determined. The specific methods used for measuring T_g are discussed in detail in Section 3.2.

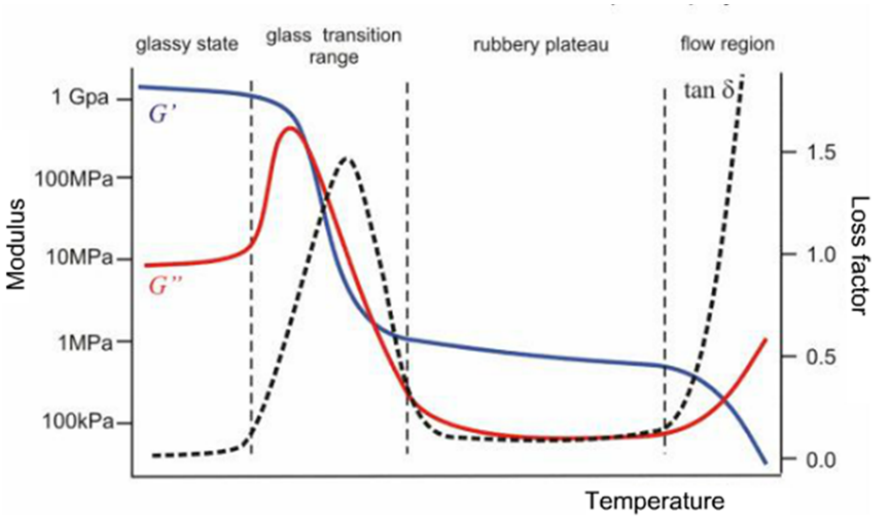

FIGURE 3.1: A typical graph of moduli and loss factor versus frequency in DMA [90].

The strain rates in DMA were approximated as the average strain rate in a quarter of a

cycle of the sinusoidal force. The strain amplitude can be approximated as the prescribed displacement divided by the initial specimen gauge length, and the time duration is a quarter of the period of the excitation force. It is assumed that the strain change in this time duration is linear. Therefore, the average strain rate $\dot{\varepsilon}$ can be calculated as:

$$\dot{\varepsilon} = \frac{strain}{time} = \frac{\frac{x_0}{l}}{\frac{1}{4\omega}} \tag{3.1}$$

where x_0 is sample head displacement in a quarter of a cycle of the sinusoidal force, l is initial specimen length, ω is frequency of the excitation force.

3.1.2 Introduction to Tensile Tests

Two kinds of uniaxial tests can be performed to determine a material's mechanical properties: compressive and tensile. These tests can provide a wide range of stress/strain data at specific strain rates and temperatures. Such tests have been standardised as defined by the British Standard Institute [118]. A lot of literature have reported compressive test on PMMA, covering strain rates ranging from 10^{-4}/s to 10^{-1}/s and at temperatures ranging from room temperature to well above PMMA's T_g [105, 107, 108, 119]. However, there are currently no published comprehensive tensile test data sets covering the temperature range from T_g to 10 °C above T_g at every 1 °C. The PMMA film used in this project (Plexiglas 99524, Evonik Röhm, Germany) has a thickness of less than 1 millimetre and is therefore not suitable for compressive tests which require sample typically more than 1 millimetre thick. Therefore, tensile tests were conducted instead of the more commonly used compressive tests. To verify the tensile test results, we compared the results with the compressive test results made by Ames [108]. Both the tensile and compressive test data had the same trends however there were discrepancy between two groups of data values because the PMMA type was different. The experimental data are calibrated and verified in Chapter 5.

In tensile tests the applied load and deformation are recorded. The term engineering stress σ_E is defined by the load F divided by the initial cross-sectional area A_0, while the

engineering strain ε_E is defined by the length change ΔL divided by the initial length l_0 [118].

$$\sigma_E = \frac{F}{A_0} \tag{3.2}$$

$$\varepsilon_E = \frac{\Delta L}{l_0} \tag{3.3}$$

However, true terms of stress and strain should be used in situations with large deformations. True stress and strain can be calculated as follows [118]:

$$\varepsilon_T = \sigma_E(1+\varepsilon_E)\varepsilon_T = ln(1+\varepsilon_E) \tag{3.4}$$

$$\sigma_T = \frac{F}{A} = \frac{F}{A_0}\frac{L}{L_0} = \sigma_E(1+\varepsilon_E) \tag{3.5}$$

3.2 DMA

3.2.1 Equipment

We have conducted DMA tests on a dynamic mechanical analyser (DMA/SDTA861e, Mettler Toledo, USA), which has a temperature range from -150 to 500 °C and a frequency range from 0.001 to 1000 Hz. Figure 3.2 shows a schematic of the DMA/SDTA861e [120]. The force sensor is a piezoelectric crystal which generates an electrical signal from the actual force applied to the test sample. A temperature sensor is also located close to the sample. The thermal effects are measured by single differential thermal analysis (SDTA), which records the temperature difference between the sample and a reference point (which undergoes the same thermal cycle). A linear motor provides the input force through a drive shaft to the sample.

All DMA tests were carried out in tension mode, in which one end of the sample was fixed and the other end was subjected to oscillating force. The sample was pre-stressed to prevent buckling. The benefit of tension mode is that clamping does not affect the sample deformation.

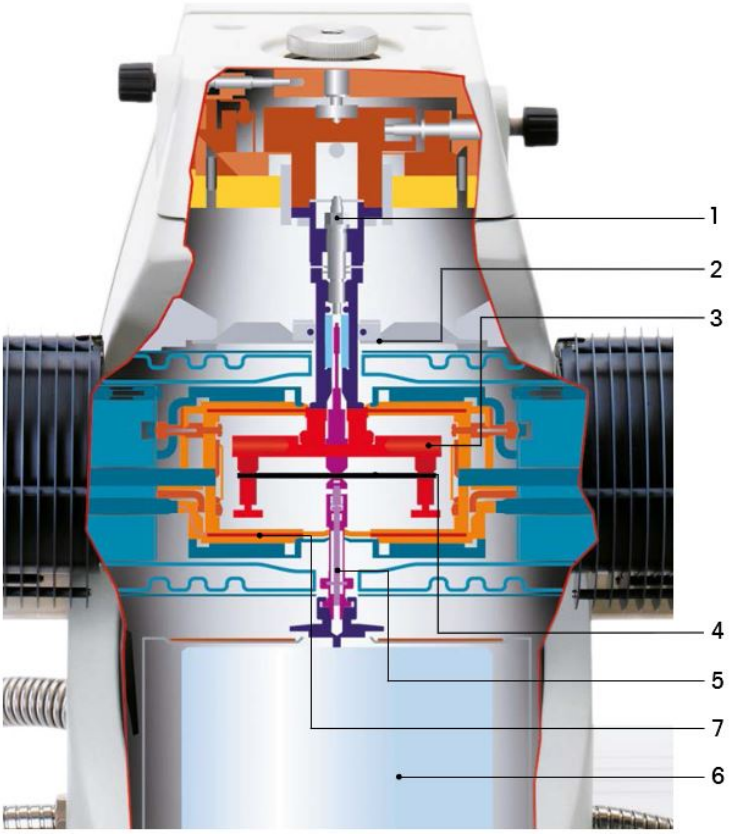

FIGURE 3.2: Schematic of the DMA/SDTA861e. Main components: 1.Force sensor; 2.Displacement sensor; 3.Clamp; 4.Sample; 5.Drive shaft; 6.Linear motor; 7.Furnace. [120]

3.2.2 Sample Material Preparation

The material tested in DMA and in tensile tests is the same one used to fabricate microfluidic chips - PMMA Plexiglas 99524 films with a glass transition temperature (T_g) of around 105 °C. Table 3.1 lists the mechanical and thermal properties of this material at room temperature [121].

Plexiglas 99524 was also the film used in the R2R hot embossing experiments in this PhD project. 375-µm-thick Plexiglas 99524 film was cut into rectangular samples with

TABLE 3.1: Mechanical and thermal properties of PMMA Plexiglas 99524 at room temperature [121].

Properties	Unit	Value
Young's modulus	(MPa)	2200
Yield stress	(MPa)	54
Yield strain	(%)	5
Nominal strain at break	(%)	35
Poisson's ratio		0.37
Pencil hardness		2H
Coefficient of linear thermal expansion (0-50 °C)	$(10^{-5} \times 1/\mathrm{K})$	10
Specific heat capacity	$(\mathrm{kJ/kg} \times \mathrm{K})$	1.5
Density	$(\mathrm{g/cm^3})$	1.16

approximate dimensions of 9 mm × 3 mm. The measuring gauge length was approximately 7 mm, depending on the clamp instalment. It has been reported Plexiglas films are produced through a cell cast method, and no molecular chain orientation exists in the as-cast film [122].

3.2.3 Testing Procedure

The PMMA specimens were loaded into the DMA machine with a pre-stress. Initial test trials were conducted to determine the linear region of the material response under the input sinusoidal force.

Then the PMMA films were tested under a temperature sweep from 20 to 150 °C at every 10 degrees to determine the appropriate force amplitudes and temperatures. Afterwards the PMMA samples were tested over the same temperature range at 1 Hz and 10 Hz. The storage modulus and loss modulus were measured as a function of temperature, and the corresponding complex modulus and loss factor were calculated.

Then a dynamic frequency sweep was performed at frequencies from 0.02 to 200 Hz, at temperatures ranging from 20 to 150 °C. For each isothermal step, a stabilisation time of 5 minutes was set prior to data recording. A reference curve was established for PMMA, from which significant material transitions could be determined. The PMMA samples

were then tested over small ranges in temperatures near the temperature of embossing (103 to 112 °C at every 1 °C) and frequencies (0.02 to 200 Hz). According to Equation (3.1), the approximate average strain rates were from 10^{-4} to 1/s.

3.2.4 Results and Analysis

3.2.4.1 Temperature Sweep

The storage modulus, loss modulus, complex modulus and loss factor versus sample temperature at 1 Hz and 10 Hz are plotted in Figures 3.3, 3.4, 3.5 and 3.6 respectively. The results are also presented for a fixed frequency and varying temperatures in Figures 3.7 and 3.8.

The storage modulus versus temperature curves exhibited a dramatic decrease in storage modulus starting at around 100 °C, where the material began to enter its viscoelastic region. The total drop of storage modulus was about two orders of magnitude. The material's T_g was identified as the onset temperature of the step-like decrease in the storage modulus, when the storage modulus was displayed logarithmically. As expected the glass transition was identified at around 110 °C, which matched the published T_g value of Plexiglas 99524. In the 10 Hz test the modulus values were mostly higher than those in the 1 Hz test. The point of glass transition was slightly different between 1 Hz and 10 Hz due to the frequency-dependent behaviour of the material. The loss modulus and complex modulus curves showed similar trends of decrease in the viscoelastic region, except that a hump was seen in the loss modulus versus temperature curve. This may be caused by the limitation of the test machine.

Figures 3.7 and 3.8 display the storage modulus, loss factor versus the sample temperature at 1 Hz and 10 Hz DMA frequency, respectively. In both curves, the storage modulus is much greater than the loss modulus at temperatures below 90 °C. The starting point of glass transition is at around 100 °C, while at 120 °C the loss factor reaches its maximum value.

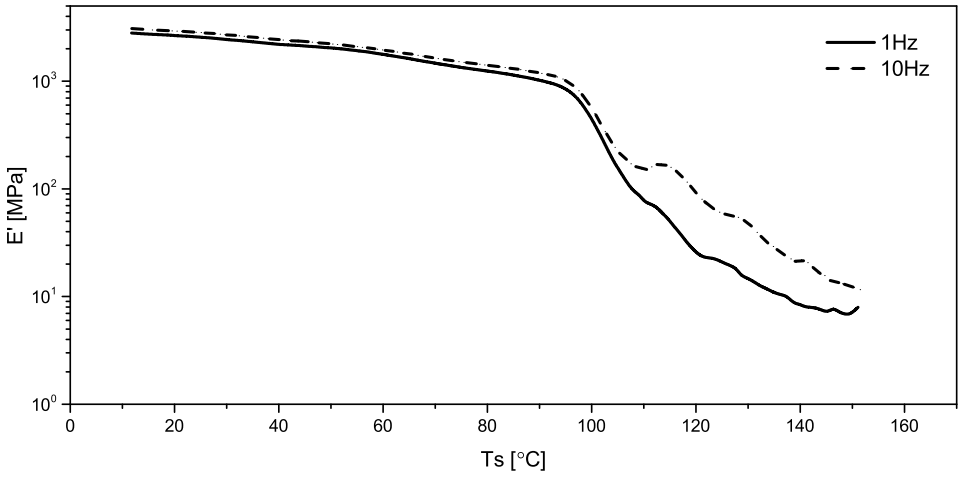

FIGURE 3.3: Storage modulus versus temperature at different frequencies.

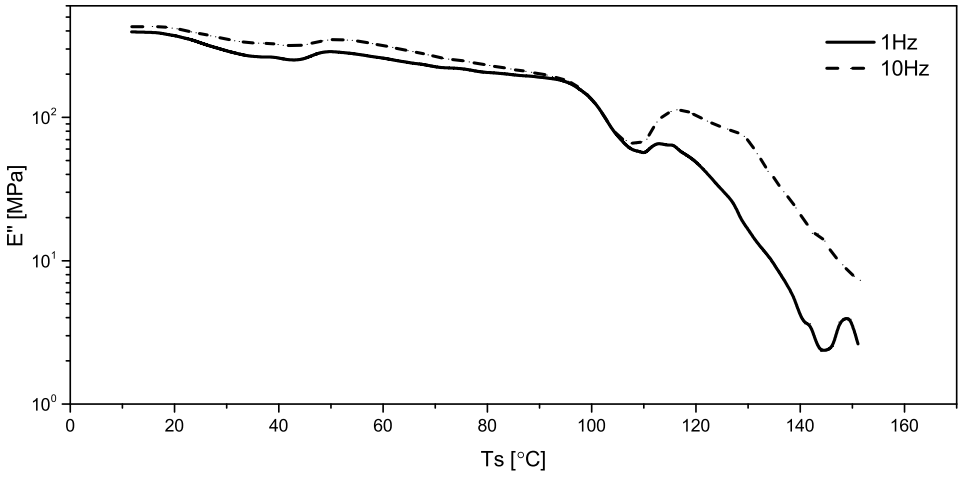

FIGURE 3.4: Loss modulus versus temperature at different frequencies.

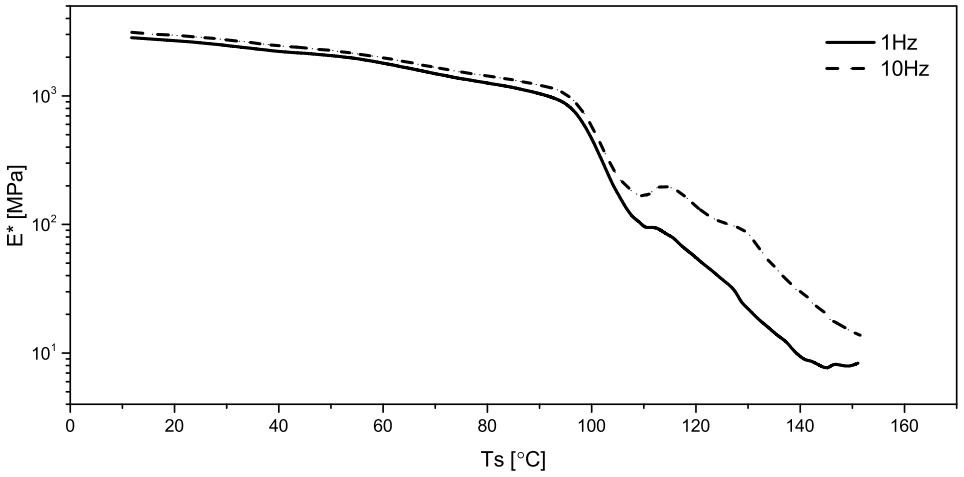

FIGURE 3.5: Complex modulus versus frequency at different temperatures.

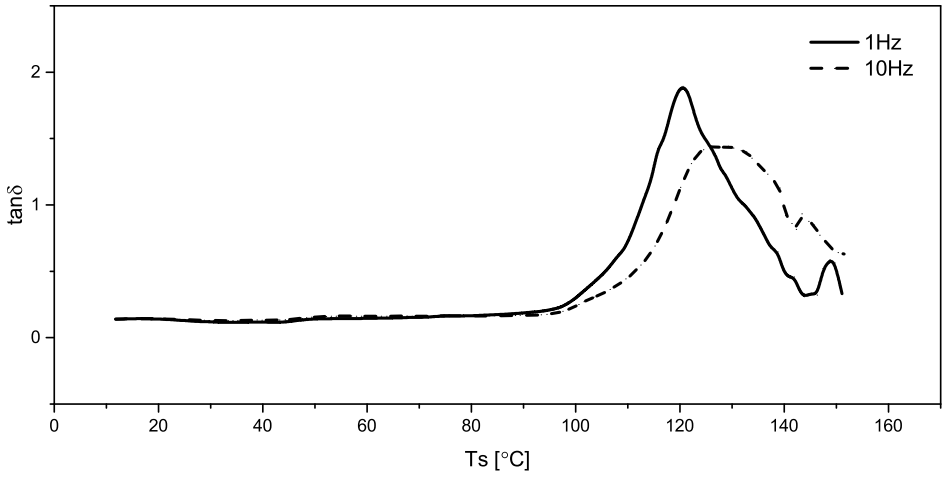

FIGURE 3.6: Loss factor versus temperature at different frequencies.

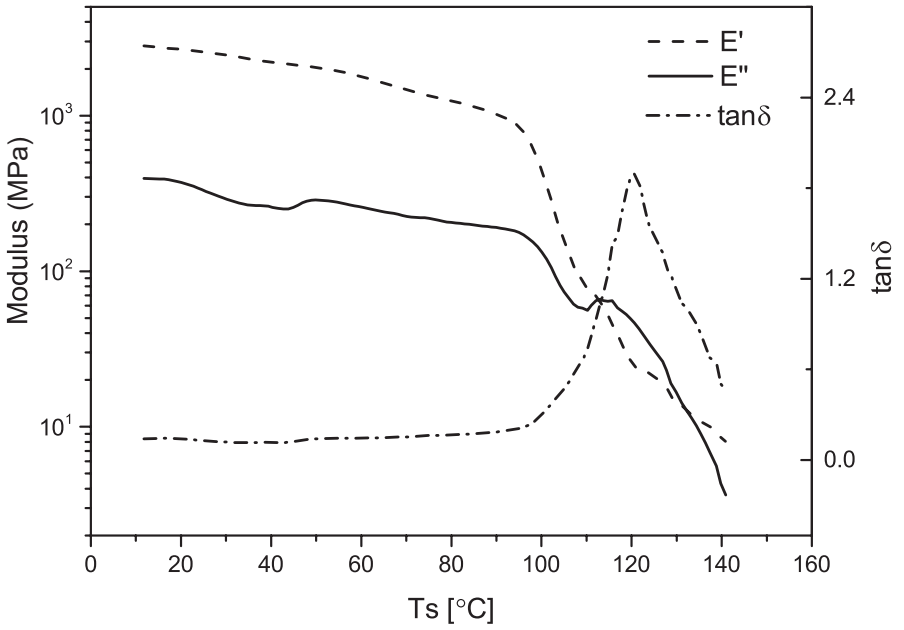

FIGURE 3.7: Storage modulus E', loss modulus E'', loss factor $\tan\delta$ versus temperature at 1 Hz.

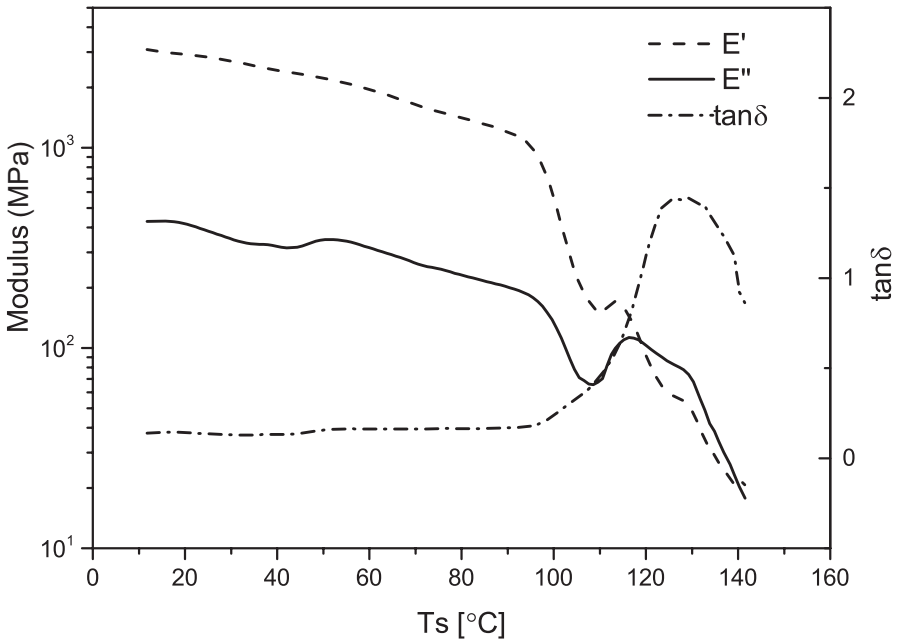

FIGURE 3.8: Storage modulus E', loss modulus E'', loss factor $\tan\delta$ versus temperature at 10 Hz.

3.2.4.2 Frequency Sweep

In the frequency sweep the material was tested from 0.02 to 200 Hz at fifteen temperature points in range between 20 and 150 °C. The measured temperature points were 23, 32, 41, 53, 62, 72, 81, 91, 101, 110, 120, 129, and 149 °C, respectively. The storage modulus results are shown in Figures 3.9 and 3.10. At temperatures lower than 100 °C, the storage modulus decreased slightly as the temperature increased. This indicated that in this temperature range the polymer material was solid-like. Meanwhile, at each temperature below T_g, the frequency-dependence was not significant. However, at 101 °C storage modulus decreased by one order of magnitude. This indicated that the material started to show rubber-like properties in this region. At temperatures higher than 101 °C the material was rubber-like, and the storage modulus data showed strong frequency dependence in this temperature range.

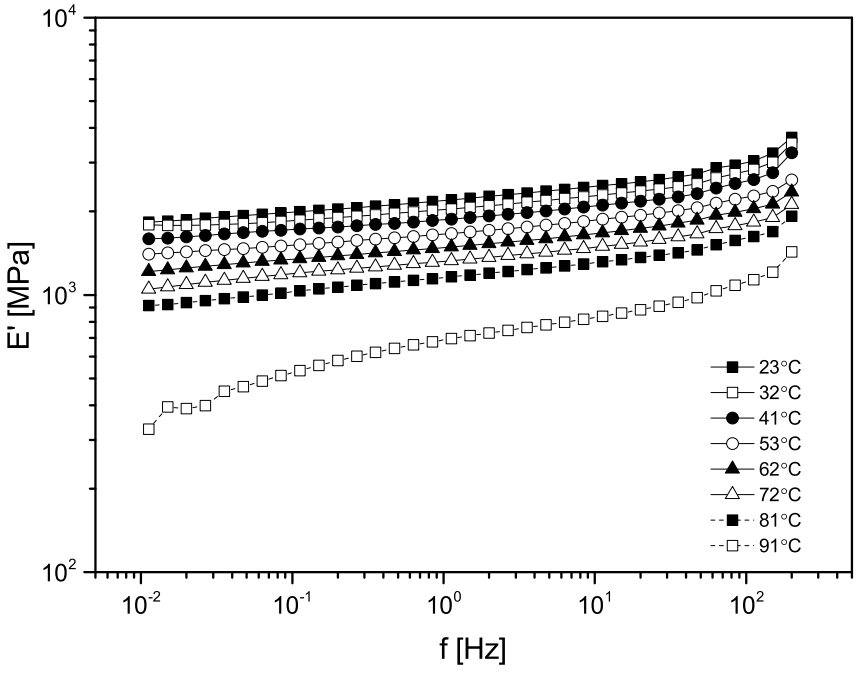

FIGURE 3.9: Storage modulus versus frequency (below T_g).

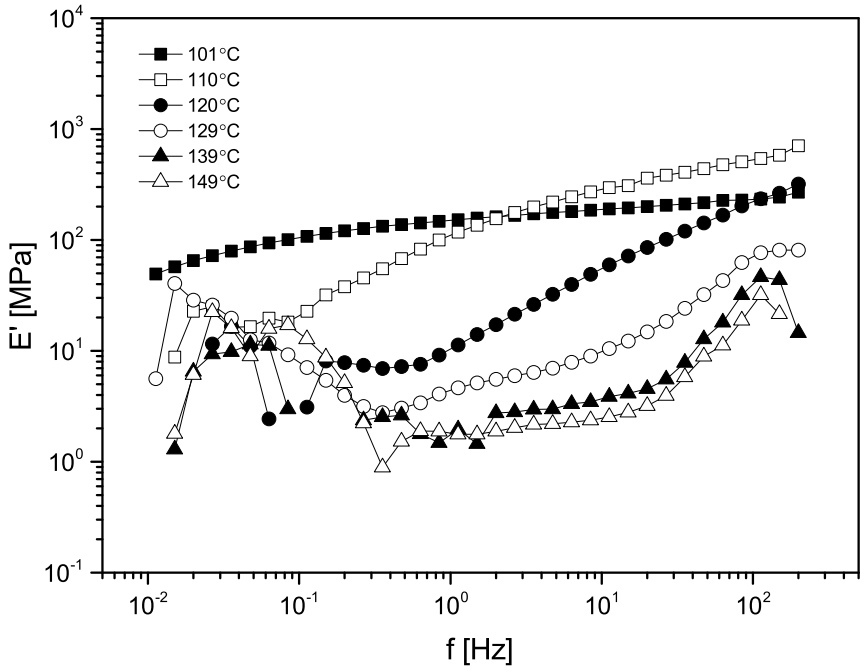

FIGURE 3.10: Storage modulus versus frequency (near and above T_g).

The results for complex modulus versus frequency at different temperatures from 23 to 149 °C are plotted in Figures 3.11 and 3.12. The frequency-dependence was insignificant for the temperature range from 23 to 101 °C, while at temperatures above 101 °C, the complex modulus varied dramatically with the increasing test frequency. Figure 3.12 was then used to construct a master curve by applying the time-temperature superposition principle and shifting the curves of temperatures above 101 °C [91] (Figure 3.13). This approach can be used to predict the rate-dependent viscoelastic behaviour of PMMA at a wide range of rates.

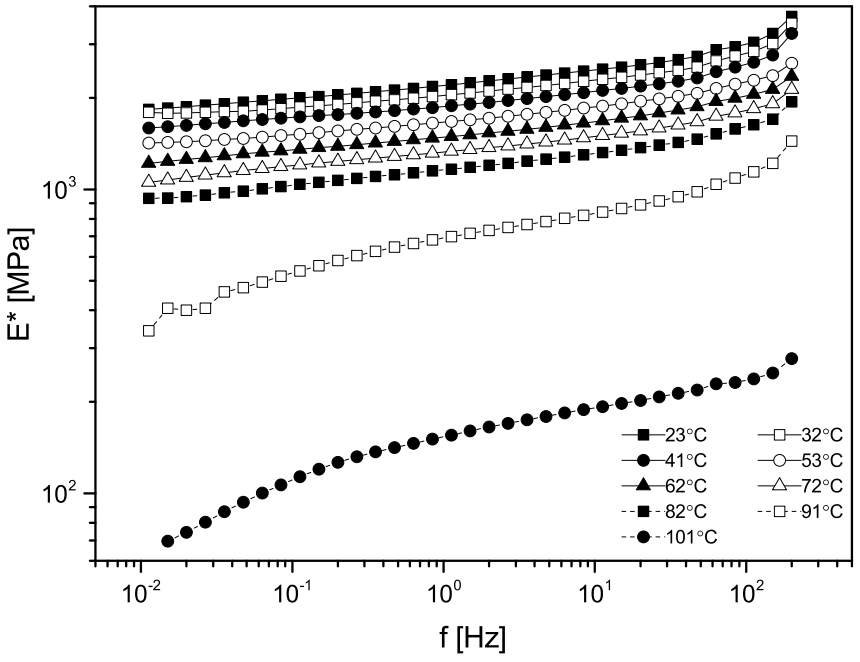

FIGURE 3.11: Complex modulus versus frequency at temperatures from 23 to 101 °C

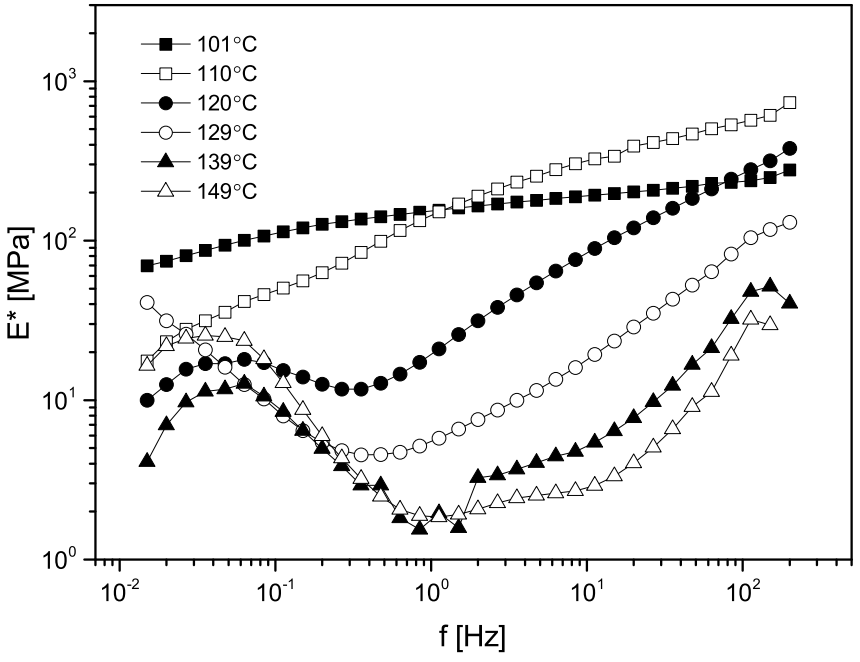

FIGURE 3.12: Complex modulus versus frequency at temperatures from 101 to 149 °C

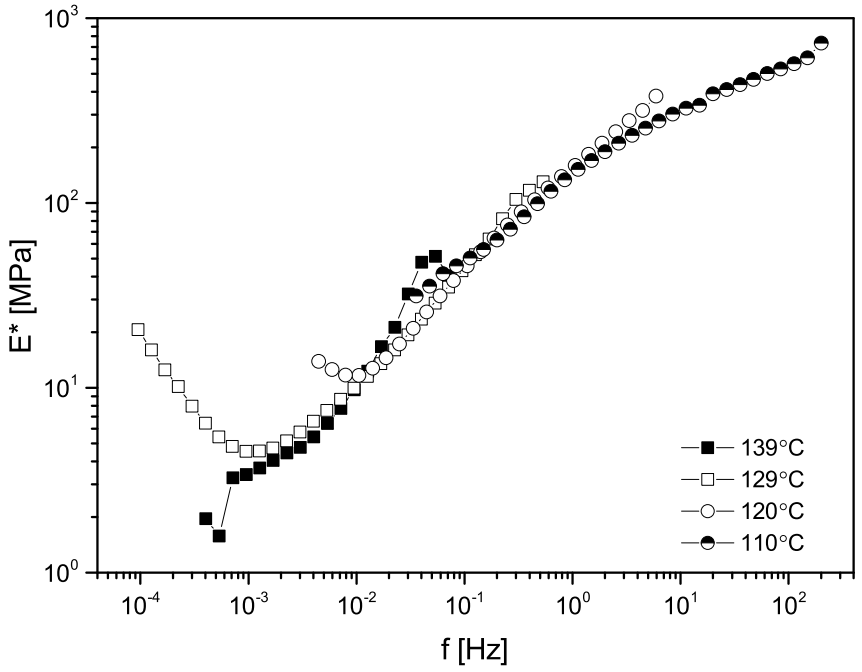

FIGURE 3.13: Master curve of complex modulus versus frequency.

The next frequency sweep was performed over the specific temperature range in R2R hot embossing experiments. It is advised that embossing any features below T_g is difficult, as elastic behaviour dominants in this temperature range. The viscoelastic region is most suitable for hot embossing, where the material is both viscous and elastic. To show the dependence of the T_g on frequency in R2R hot embossing, the specimens were tested in the frequency sweep at every degree from 103 °C to 110 °C. In each of the isothermal steps, 5 minutes of stabilisation time was set prior to data recording. The frequency range was from 0.02 to 200 Hz. The captured storage, loss and complex moduli are displayed in Figures 3.14, 3.15 and 3.16, respectively. Both storage and loss moduli were nearly frequency-independent below 105 °C. From 105 to 112 °C both E' and E'' increased with the increasing frequency. At higher frequencies (near 200 Hz) the moduli changed slightly with the increasing temperature. However, at lower frequencies the moduli increasing tendency became stronger with the increasing temperature. This indicates that PMMA tends to soften more significantly at low strain rates than for higher strain rates. The test data failed to fit in the time-temperature superposition,

which could be caused by non-isothermal conditions at each tested temperature.

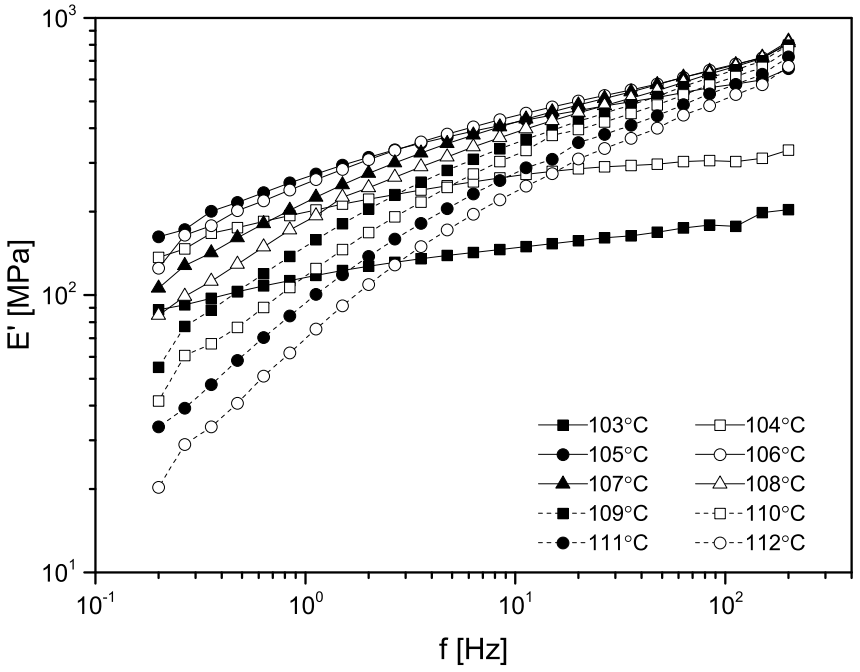

FIGURE 3.14: Storage modulus versus frequency at temperatures from 103 to 112 °C

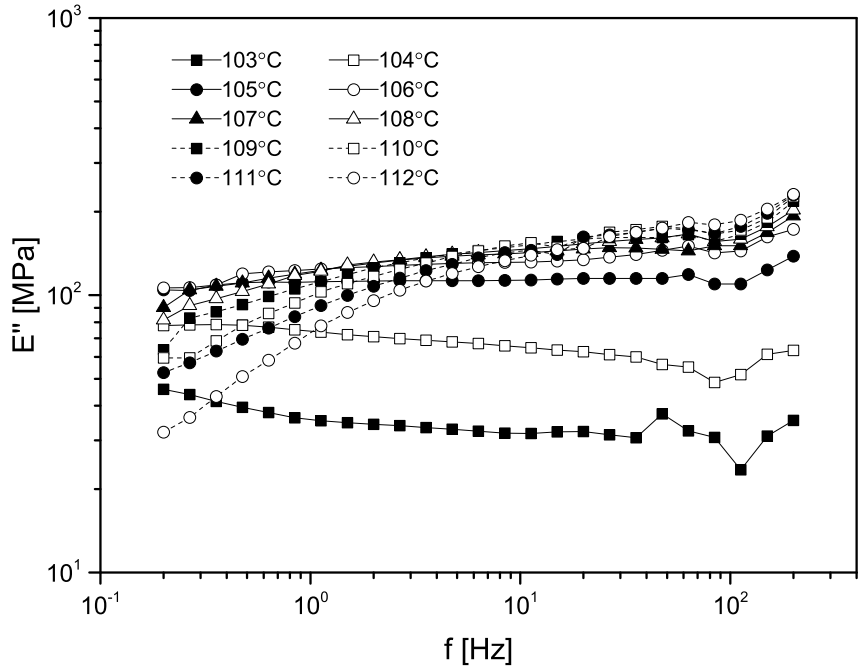

FIGURE 3.15: Loss modulus versus frequency at temperatures from 103 to 112 °C

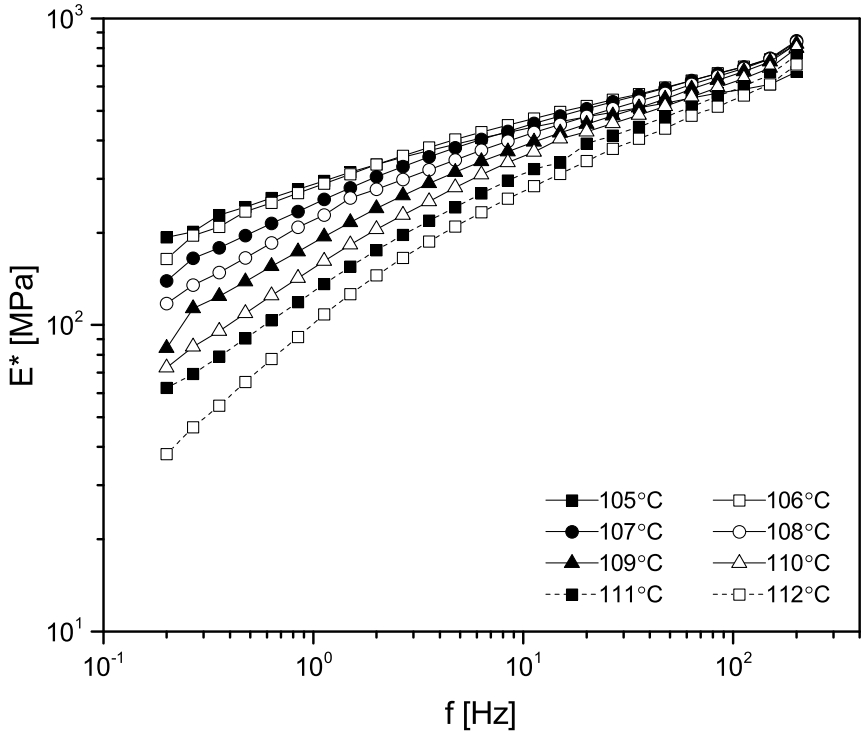

FIGURE 3.16: Complex modulus versus frequency at temperatures from 105 to 112 °C

3.3 Tensile Tests

3.3.1 Equipment

The tensile test machine used is an electromechanical, dual column tensometer having a load capacity of 10 kN (Instron 5569, Instron, USA). The principle of this tensile machine is that it uses an electrical motor and screws to control the crosshead's movement. A load cell measures the input load force. According to the mechanical properties of Plexiglas 99524 (Table 3.1), the yield stress is 54 MPa. Given the sample thickness (0.375 mm) and width (25.4 mm), the estimated maximum load was calculated to be around 500 N using Equation (3.2). To get the satisfactory testing resolution the preferred load cell is no greater than 10 kN so that the maximum load is no less than 5% of the load range.

All test samples were cut from the Plexiglas 99524 film using a carbon dioxide (CO_2) laser cutter (Synrad Laser, CadCam Technology, UK). A CO_2 laser cutter produces an infrared (IR) light with the principal wavelength bands centring on 9.4 and 10.6 µm. As PMMA absorbs IR light with a wavelength band ranging from 2.8 to 25 µm, the CO_2 laser can be used to cut PMMA samples [123].

To precisely measure the strains when the thin polymer deforms, a suitable extensometer have to be selected. A common type is the clip-on, strain gauge extensometer. However, this type does not meet the requirement for testing PMMA at higher temperatures, because the damage and distortion caused by the extensometer must be kept at minimum. The optimum choice is to use a non-contact extensometer, such as a video extensometer. It is recommended by Instron that two dots, each of 2 millimetres diameter, should be used to mark the gauge length using a white marker pen [124]. The video extensometer captures the movement of these white dots and calculates the axial strain as the source of tensile strain. The specimens were clamped with two screw side-action grips with a maximum load capacity of 10 kN. Sand papers were glued to the screw side-action grips to increase the friction between the grip and sample.

The tensometer was also equipped with an environmental chamber (Series 3119, Instron, USA) with a temperature range of -100 to 300 °C. The video extensometer was mounted near to a glass window of this environmental chamber (Figure 3.17 and 3.18).

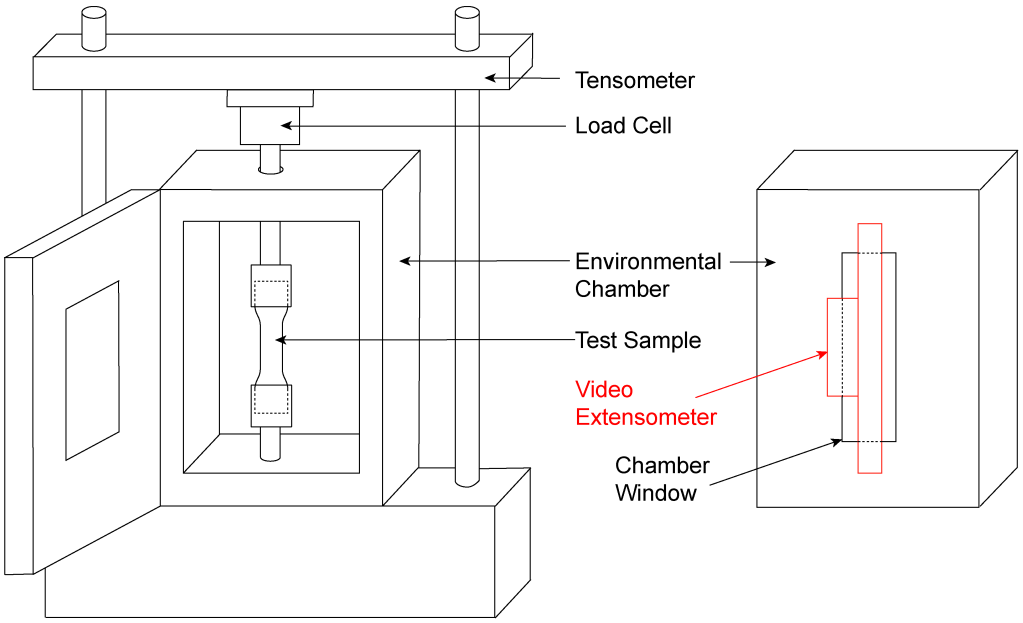

FIGURE 3.17: Schematic of the tensometer with an environmental chamber. The right graph shows that a video extensometer is mounted to the outside of the environmental chamber to measure the axial strain.

FIGURE 3.18: Pictures of a PMMA sample which was clamped in the environmental chamber. The two white dots setted the length of gauge length and were recorded by the video extensometer to calculate the axial strain (engineering strain).

3.3.2 Sample Preparation

The specimens were cut from the polymer film rolls using a CO_2 laser cutter following the British Standards Institute (BSI) standardised tensile testing guide [125, 126]. According to ISO 527-3 (Plastics - Determination of tensile properties - Part 3: Test conditions for films and sheets) [126], the specimen shape and dimensions should be as follows: the preferred specimen is dumbbell-shaped, with a gauge length of approximately 50 millimetres, and an initial distance (between two grips) of approximately 100 millimetres.

The dimensions of the dumbbell-shaped specimens are shown in Figure 3.19 and Table 3.2. The dumbbell shape is widely used in uniaxial compressive and tensile tests,

because it can avoid specimen fracture or excessive extension in the area being gripped. It has a gauge length of 25.4 millimetres (about 1 inch). The gauge section in the middle reduces stress since the stress is inversely proportional to the cross-sectional area of the specimen.

After cutting the dimensions of width and length of the specimen were measured with a caliper to ensure correct dimensions. The thermoplastic polymer materials were regarded isotropic; however the properties of certain materials may vary in different directions. Two groups of samples were made with their major axes perpendicular and parallel to the PMMA web moving direction.

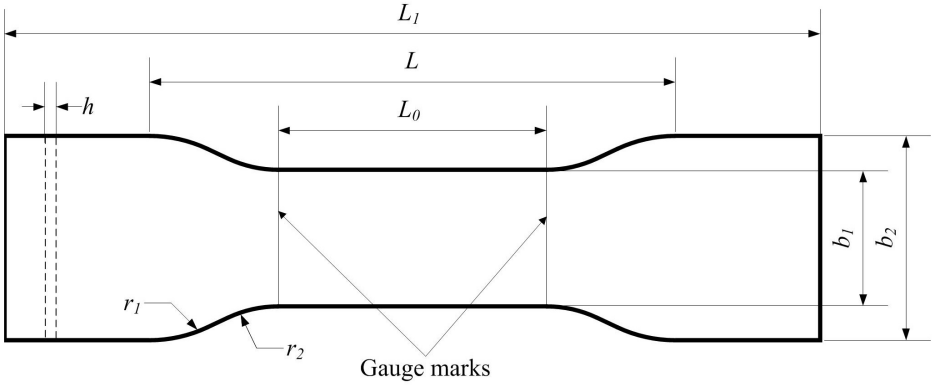

FIGURE 3.19: Tensile testing specimen type 2, reproduced from BSI [125].

TABLE 3.2: The dimensions of the tensile test specimen in millimetres, reproduced from BSI [125].

Symbol	Meaning	Value
b_1	Width of parallel-sided portion	25.4
b_2	Width at ends	38
h	Thickness	0.375
L_0	Gauge length	50
L	Initial distance between grips	98
L_1	Overall length	152
r_1	Small radius	22
r_2	Large radius	25.4

3.3.3 Testing Procedure

Initial trials were made at room temperature before testing at higher temperatures. This was to determine whether the tensile testing instrument is precise enough to capture the stress-strain data. The testing strain rates were quasi-static strain rates (0.001, 0.01 and 0.1/s), following Ames *et al.*'s work in the characterisation of amorphous polymers [108]. The testing temperatures were 90, 100, 105, 107, 110 and 120 °C. These temperatures were selected according to the temperatures on the embossing roller and counter pressure roller during R2R hot embossing. All tensile tests were conducted at constant true strain rates to tensile true strains exceeding 50%. All strain measurements were made using the video extensometer.

3.3.4 Results and Interpretation

Here we explain the strain softening, hardening and recovery with a true stress - true strain test curve in Figure 3.21. Upon loading the material exhibits hyperelastic behaviour and then yields. Strain softening occurs after the yield point, followed by increasing strain hardening. Finally insufficient strain recovery is shown during the unloading process. This example will be used to describe the experimental results of tensile tests. The tensile tests data was compared with compressive test results made by Ames [108], as shown in Figure 3.20.

The results of tensile tests on PMMA at different strain rates (0.001, 0.01 and 0.1/s) at each temperature ranging from 90 to 120 °C are shown in Figures 3.22, 3.23, 3.24, 3.25, 3.26 and 3.27, respectively. At temperatures below 105 °C (90 and 100 °C), the yield strength increased by almost 5 MPa when the strain rate increased from 0.001 to 0.01 and to 0.1/s. Strain-hardening was observed at all strain rates. This was caused by the limited extensibility of the polymer chains, as suggested by Ames *et al.* [108]. The strain recovery was about 12% in this temperature range. Softening effect was also found at these temperatures and it was more significant at higher strain rates. As suggested by Mulliken *et al.* [119], softening was caused by increased sample temperature in tensile

tests when the strain rate was increased. When heat was generated by the material's plastic deformation, and materials exhibited more significant softening when this heat could not be dissipated at higher strain rates. In the temperature range above 105 °C, the yield peak started to disappear at 0.001/s strain rate, which indicated a rubber-like response in this region. At 107 °C, this rubber-like behaviour was observed at the lowest strain rate of 0.001/s and the strain recovery rate reached to around 40%, however at 0.01 and 0.1/s the material response was still glass-like. At 120 °C the material deformed in a ductile manner at all three strain rates. The highest strain recovery rate was about 50% at a strain rate of 0.001/s.

The true stress versus true strain results at each strain rate (0.001 , 0.01 and 0.1/s) and temperatures ranging from 90 to 120 °C are presented in Figures 3.28, 3.29 and 3.30. The true stress versus true strain curves from low to high temperatures were different at all tested strain rates. All these figures show that the yield strength decreased and then disappeared with increasing temperature spanning PMMA's T_g, while the initial elastic modulus dropped dramatically at 110 and 120 °C. Strain softening was observed at all temperatures below 110 °C at the strain rates 0.01 and 0.1/s.

Figure 3.31 compares the tensile test data at a strain rate of 0.01/s at 110 °C in two perpendicular directions. It was found that the stress-strain curves of two perpendicular directions were nearly identical.

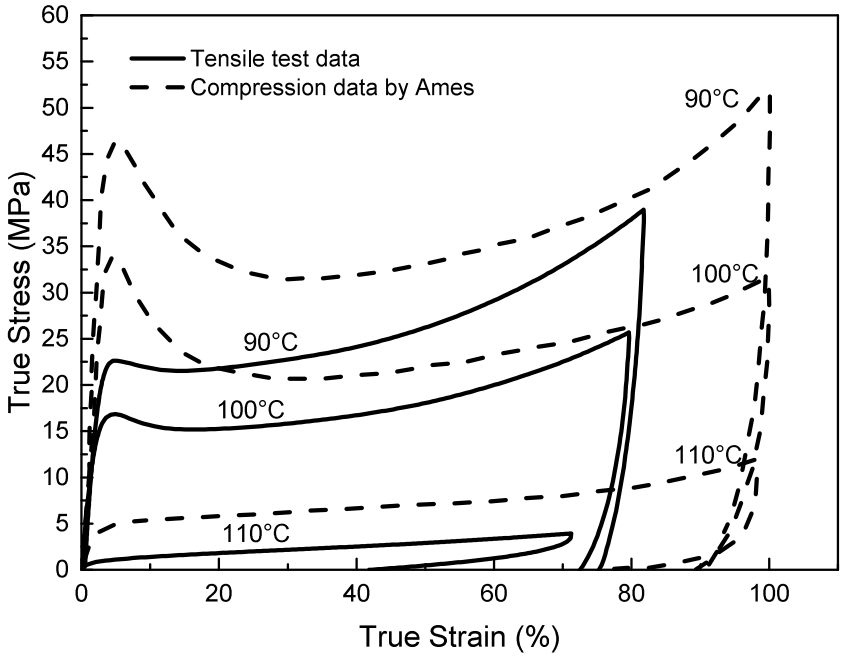

FIGURE 3.20: Comparison between the tensile and compressive test results at 0.1/s.

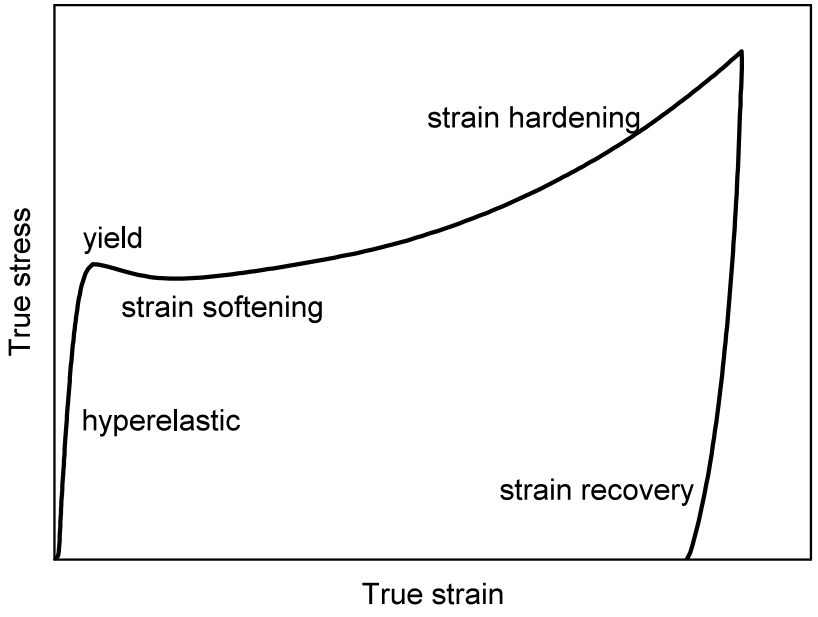

FIGURE 3.21: Yield, strain softening, hardening and recovery.

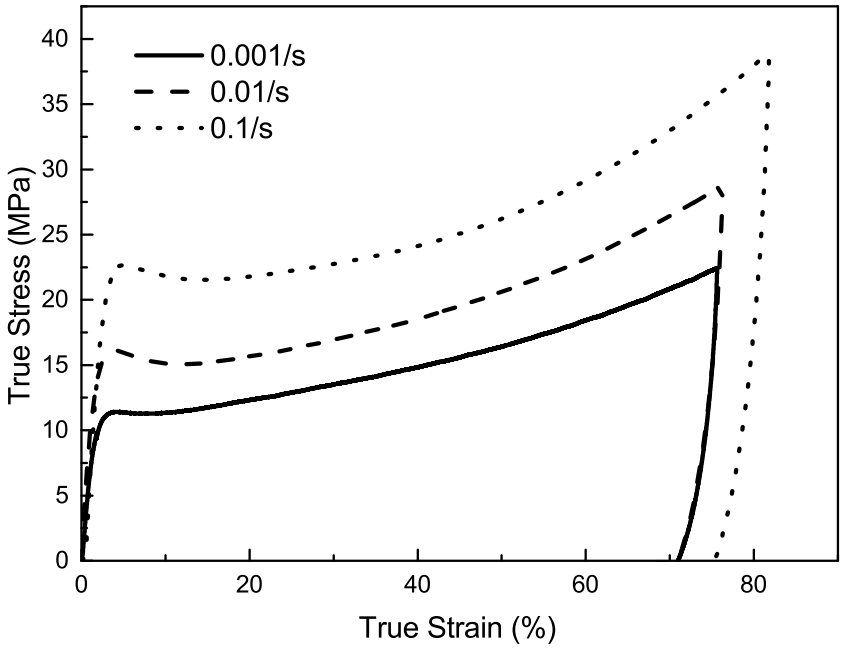

FIGURE 3.22: Tensile tests at 90 °C and different strain rates.

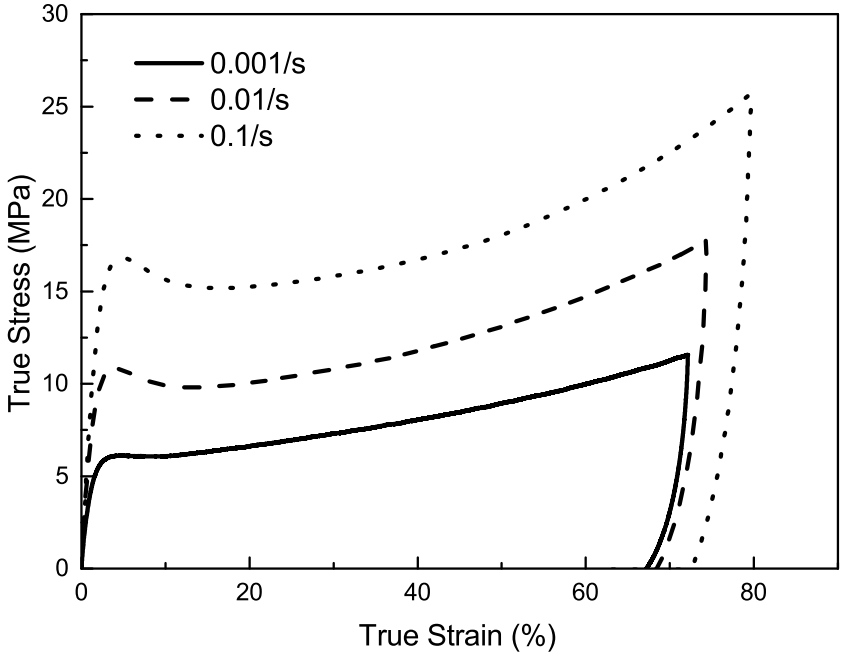

FIGURE 3.23: Tensile tests at 100 °C and different strain rates.

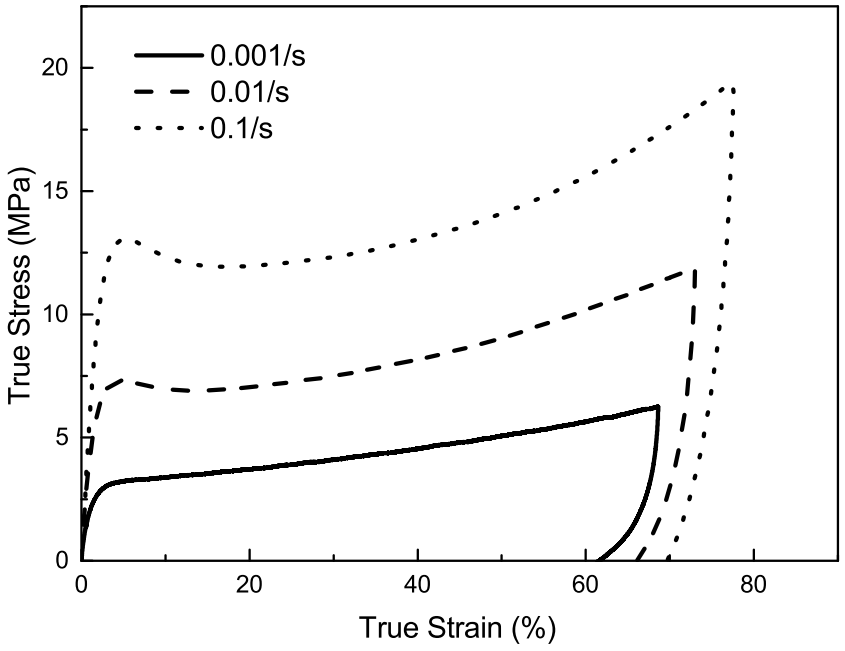

FIGURE 3.24: Tensile tests at 105 °C and different strain rates.

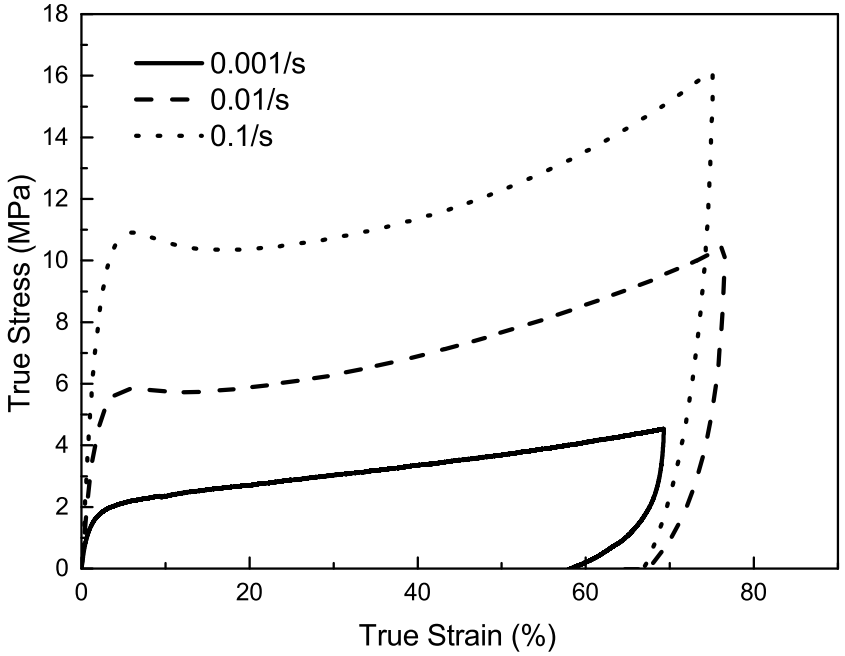

FIGURE 3.25: Tensile tests at 107 °C and different strain rates.

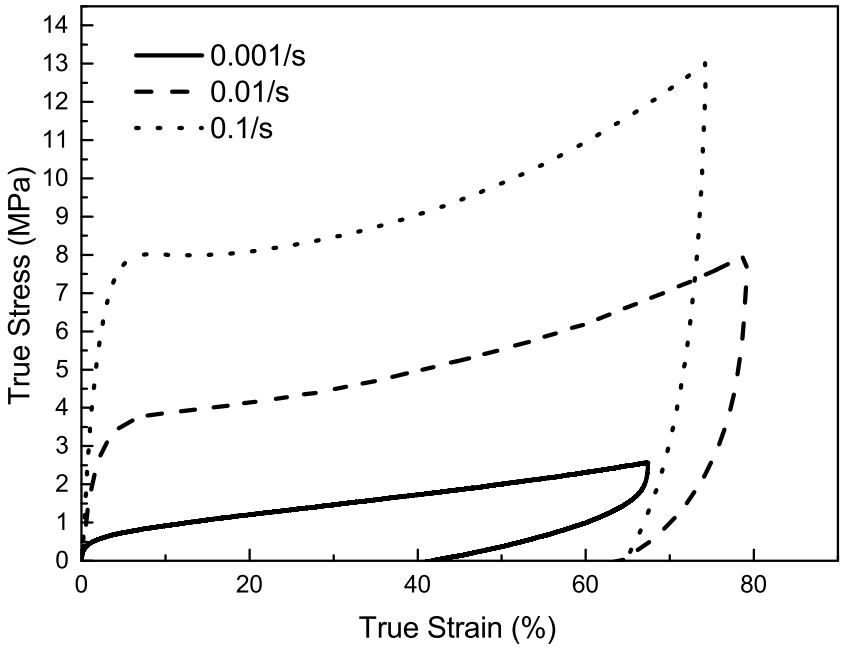

FIGURE 3.26: Tensile tests at 110 °C and different strain rates.

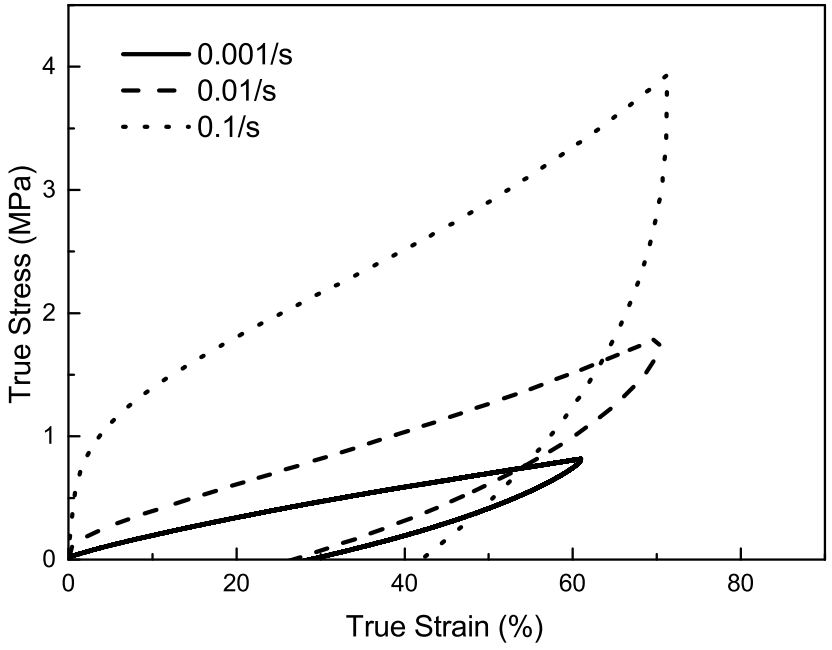

FIGURE 3.27: Tensile tests at 120 °C and different strain rates.

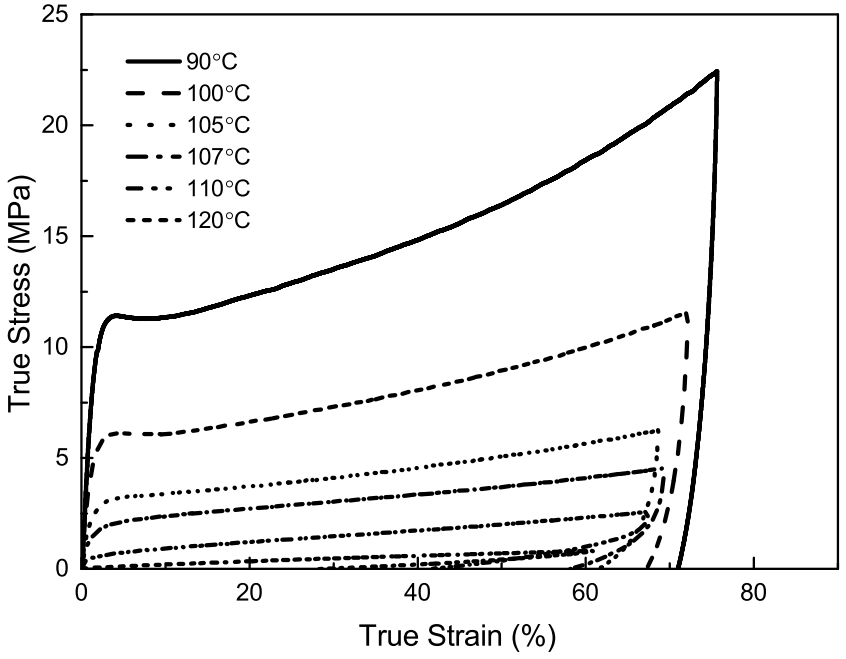

FIGURE 3.28: Tensile tests at a strain rate of 0.001/s and temperatures ranging from 90 to 120 °C.

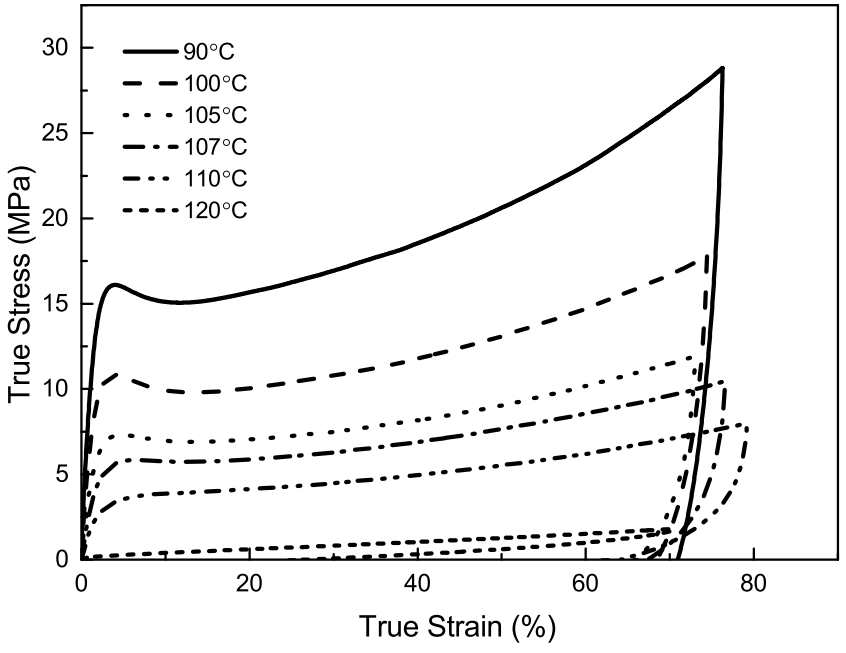

FIGURE 3.29: Tensile tests at a strain rate of 0.01/s and temperatures ranging from 90 to 120 °C.

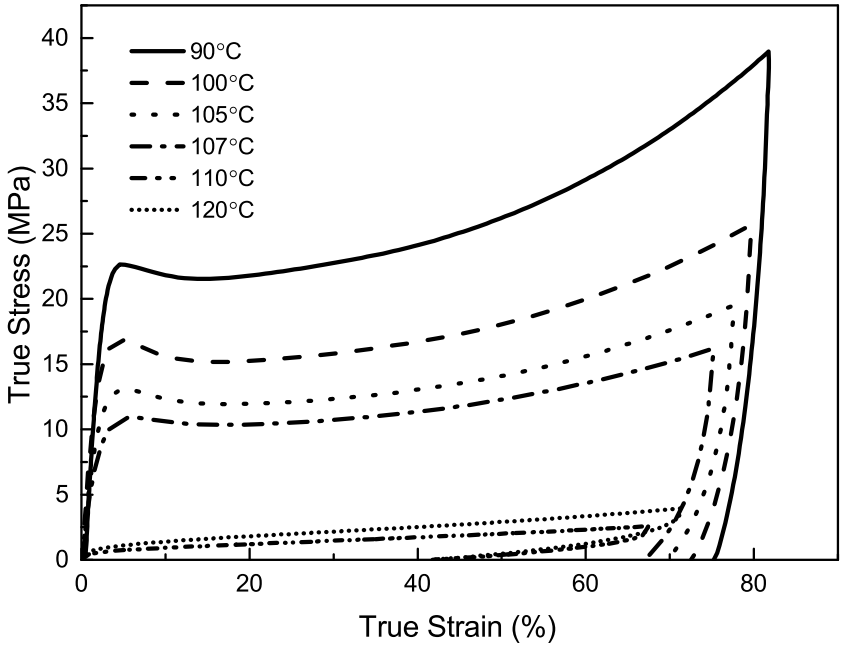

FIGURE 3.30: Tensile tests at a strain rate of 0.1/s and temperatures ranging from 90 to 120 °C.

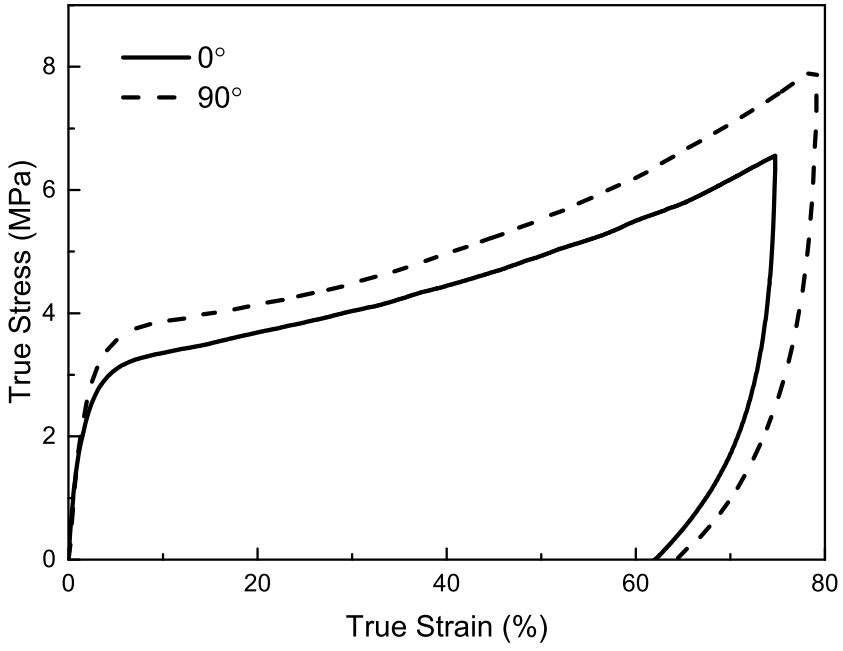

FIGURE 3.31: Tensile tests at 110 °C and 0.01/s strain rate in two perpendicular directions.

Both tensile test and DMA results indicated that temperature had a significant influence on the thermo-mechanical behaviour of PMMA. Below T_g the material response was glass-like and above T_g the material response was rubber-like.

Generally, the storage and loss moduli decreased with increasing temperature. When temperature increased from below T_g to above T_g, the reduction in the material's moduli were from 1 to 3 orders of magnitude. The frequency dependence during DMA was insignificant until the temperature was rose to the temperature near T_g. During the tensile tests, the yield peak decreased and then disappeared as the temperature increased to T_g and higher temperatures. Additionally, the strain recovery rate increased with the temperature.

However, the effects of temperature varied at different frequencies. Therefore they should be studied together with the effects of strain rate. The effects of strain rate were influenced by the temperature. Generally, the initial moduli at the low strain rate were much higher than those at higher strain rates. Strain hardening could be seen at strain rates of 0.001 and 0.01/s at temperatures below and near T_g, along with post-yield softening at these temperatures and strain rates.

Another important thermo-mechanical behaviour observed was that at temperatures below T_g the effect of strain rate on the storage modulus, loss modulus and complex modulus were insignificant, however at temperatures near and above T_g the strain rate effect was very dramatic as these moduli decreased by at least one order of magnitude. The strain rate-dependent behaviour over a wide temperature range above T_g was summarised with a master curve using the time-temperature superposition technique.

3.4 Material Calibrations

After undertaking empirical analysis on the thermo-mechanical behaviour of PMMA using DMA and tensile tests, a quantitative description of the thermo-mechanical behaviour of PMMA at temperatures across its T_g is essential for the simulation of hot

embossing processes. From the existing literature reviewed we selected a few constitutive models to for the calibration of test data covering a range of strain rates and temperatures. Here we selected viscoelastic and viscoplastic models for such calibration steps.

3.4.1 Viscoelasticity

We start by employing a widely used model for the simulation of hot embossing, the generalised Maxwell model, which is a linear viscoelastic model. The generalised Maxwell model benefits from its simple definitions.

For the generalised Maxwell model, the storage modulus E′ and loss modulus E″ are:

$$E'(\omega) = E_0 \left[1 - \sum_{i=1}^{N} e_i \right] + E_0 \sum_{i=1}^{N} \frac{e_i \eta_i^2 \omega^2}{1 + \eta_i^2 \omega^2} \tag{3.6}$$

$$E''(\omega) = E_0 \sum_{i=1}^{N} \frac{e_i \eta_i \omega}{1 + \eta_i^2 \omega^2} \tag{3.7}$$

where a dimensionless complex modulus e_i is defined as:

$$e_i = \frac{E_i}{E_0} \tag{3.8}$$

Four relaxation times (0.001, 0.01, 0.1, 1 s) were selected at every decade on the logarithmic scale to represent four parallel branches [127]. The material parameters were obtained by calibrating the DMA curves of complex modulus versus frequency at temperatures from 106 to 112 °C.The least-square method was implemented to and the curve of each temperature was optimised with simplex method and fitted with user-defined function in the graphing and data analysis software, Origin Pro 2015 (OriginLab, USA), as shown in Figure 3.32. The fitted parameters of each temperature are shown in Table 3.3.

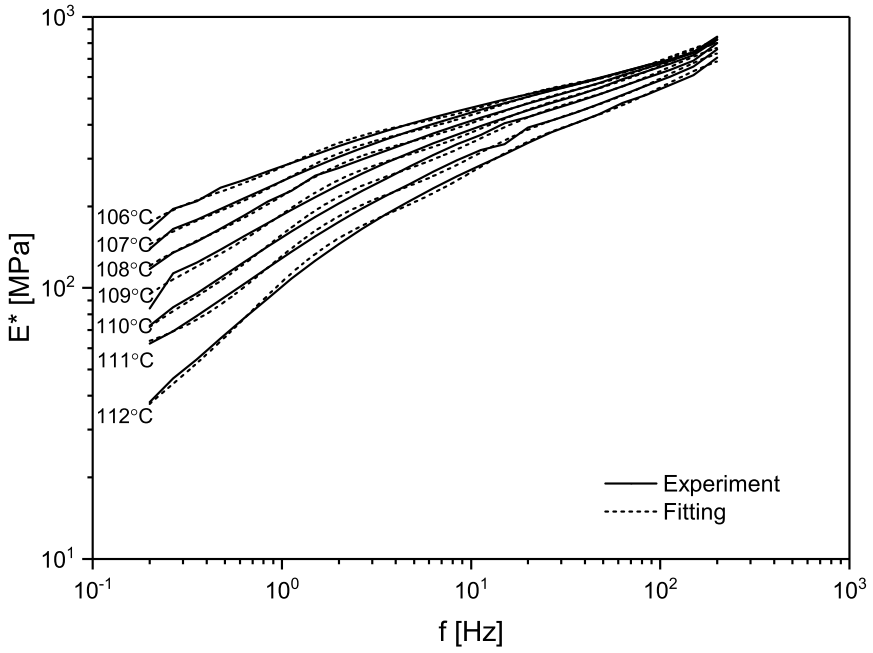

FIGURE 3.32: Experimental data (–) and fitting data (- -) of complex modulus versus frequency at temperatures from 106 to 112 °C.

TABLE 3.3: Prony series coefficients of PMMA at temperatures from 105 to 112 °C.

Temperature	E_0	$e_1(\eta$=0.001 s)	$e_2(\eta$=0.01 s)	$e_3(\eta$=0.1 s)	$e_4(\eta$=1 s)
105 °C	727.29265	0.29101	0.18401	0.21864	0.26656
106 °C	920.9335	0.38915	0.1904	0.20529	0.21499
107 °C	943.11653	0.41399	0.20777	0.21033	0.1677
108 °C	950.1843	0.44909	0.21068	0.20604	0.13407
109 °C	940.7643	0.47231	0.22618	0.20051	0.10074
110 °C	902.82374	0.47981	0.25099	0.1961	0.07305
111 °C	869.72068	0.51663	0.24804	0.16662	0.01106
112 °C	815.88808	0.53471	0.26378	0.17026	0.03122

3.4.2 Viscoplasticity

For the viscoplastic behaviour of PMMA we employed a parallel network model with viscoplastic branches, which is included in the PolyUMod library. The model was a combination of hyperelastic model and a power-law flow with strain-dependence. After some trial calibrations we selected the Yeoh model from a number of hyperelastic models.

The Cauchy stress for the Yeoh model is [99]:

$$\sigma = \frac{2}{J}\left\{C_{10} + 2C_{20}\left(I_1^* - 3\right) + 3C_{30}\left(I_1^* - 3\right)^2\right\}\mathrm{dev}\left[\mathbf{b}^*\right] + K(J-1)\mathbf{I} \tag{3.9}$$

where $\mathbf{b}^*$ is the distortional left Cauchy-Green tensor.

The flow rate is given by:

$$\dot{\gamma}^p = \left(\frac{\tau}{f_p f_{\varepsilon^p} f_\theta \hat{\tau}}\right)^{m^{eff}} \tag{3.10}$$

where $\hat{\tau}$ is the shear flow resistance, m_i and m_f are the strain exponents at small strains and large strains respectively, $\hat{\varepsilon}$ is the transition strain. m^{eff} is given by:

$$m^{eff} = \left[m_i - m_f\right] e^{-\varepsilon^p/\hat{\varepsilon}} + m_f \tag{3.11}$$

The flow evolution factor f_{ε^p} is:

$$f_{\varepsilon^p} = \frac{1}{2}\left\{f_1 + (1-f_1)\exp\left[\frac{-\varepsilon_p}{e_1}\right] + f_2 + (1-f_2)\exp\left[\frac{-\varepsilon_p}{e_2}\right]\right\} \tag{3.12}$$

f_1 and f_2 are final value of f_{ε^p} for exponential 1 and 2 respectively. e_1 and e_2 are characteristic transition strain for exponential 1 and 2 respectively.

We used MCalibration 5.0 (Veryst Engineering, USA) to fit the stress-strain curves obtained from tensile tests to the parallel network model. The software uses nonlinear search algorithms to find the material parameters from experimental data curves. The calibrated parameters are listed in Table 3.4.

To verify the parallel network model, we conducted two-dimensional, plane stress simulations following the previous tensile tests at different temperatures (90, 100, 105, 107, 110 and 120 °C and strain rates (0.001, 0.01 and $0.1/s$). The finite element geometry and boundary conditions of tensile test simulations are shown in Figure 3.33. Encastre boundary condition was applied at one clamping area of the dumbbell-shaped specimen,

TABLE 3.4: Parameters of the parallel network model.

Parameter	90°C	100°C	105°C	107°C	110°C
$C_{10,1}$ (MPa)	1.6368	1.7510	1.2155	0.5776	0.4384
$C_{20,1}$ (MPa)	0.1858	-0.2432	-0.1967	0.08679	0.06152
$C_{30,1}$ (MPa)	-0.02298	0.06062	0.04500	-0.01105	-0.00851
K_1 (MPa)	500	500	500	500	500
$C_{10,2}$ (MPa)	136.4482	143.6066	96.1229	78.8249	32.8180
$C_{20,2}$ (MPa)	3.5740	3.0121	2.1271	3.6361	3.7188
$C_{30,2}$ (MPa)	-1.5382	1.0861	1.2766	1.2655	0.9729
K_2 (MPa)	500	500	500	500	500
$\hat{\tau}$ (MPa)	25.2948	19.2010	15.7778	15.3764	11.5646
m_i	7.0627	5.3912	5.0968	3.9836	3.3787
m_f	6.5368	3.5709	3.3329	2.6764	1.8091
$\hat{\varepsilon}$	0.03925	0.1867	0.1101	0.5536	0.6134
f_1	6.0426	8.9248	12.6190	16.2593	24.5750
e_1	7.1099	5.8839	5.2358	4.6574	4.3271
f_2	-0.9015	-0.5550	-0.3950	-0.9274	-1.2335
e_2	1.3371	1.3710	0.8649	0.5671	0.7724

and coupling constraints were applied at the other clamping area. The free end of the specimen was set to move at an extension rate of v.

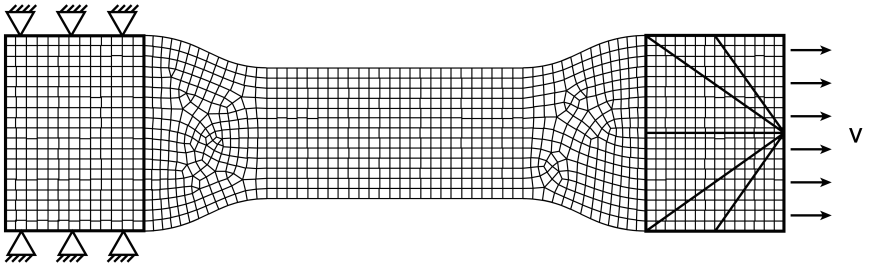

FIGURE 3.33: Finite element geometry and boundary conditions for tensile test simulations.

Figure 3.34 is an example of the deformed shape and von Mises stress distribution for the tensile test simulation at 107 °C and a strain rate of 0.1/s. The contour graph showed a uniform stress distribution across the center part of the test specimen.

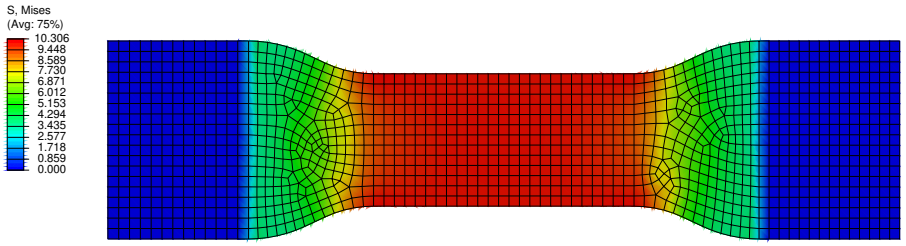

FIGURE 3.34: Von Mises stress distribution of tensile test simulations at 107 °C and a strain rate of 0.1/s.

Figures 3.35, 3.36, 3.37, 3.38 and 3.39 demonstrate the numerical and experimental results at 90, 100, 105, 107 and 110 °C, respectively. It can be seen that at 90 and 100 °C the simulations correlate well with the experimental data at all three strain rates. However, at other temperature ranges there is a large discrepancy between numerical and experimental results at the lowest strain rate 0.001/s. This may be caused by the thermal softening effects which are not considered in this isothermal constitutive model. Nonetheless, the parallel network model has proved its ability to predict the stress-strain curves across a wide range of temperatures and strain rates.

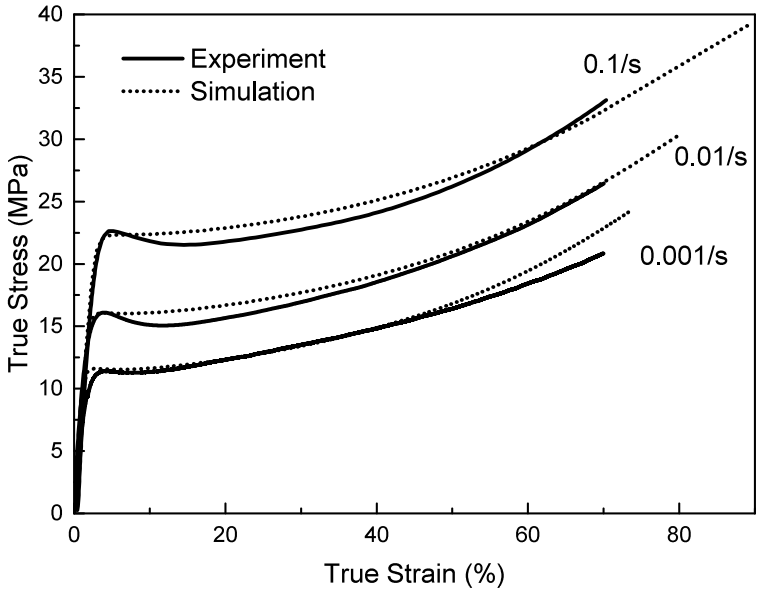

FIGURE 3.35: Simulation results versus tensile stress-strain curves at 90 °C.

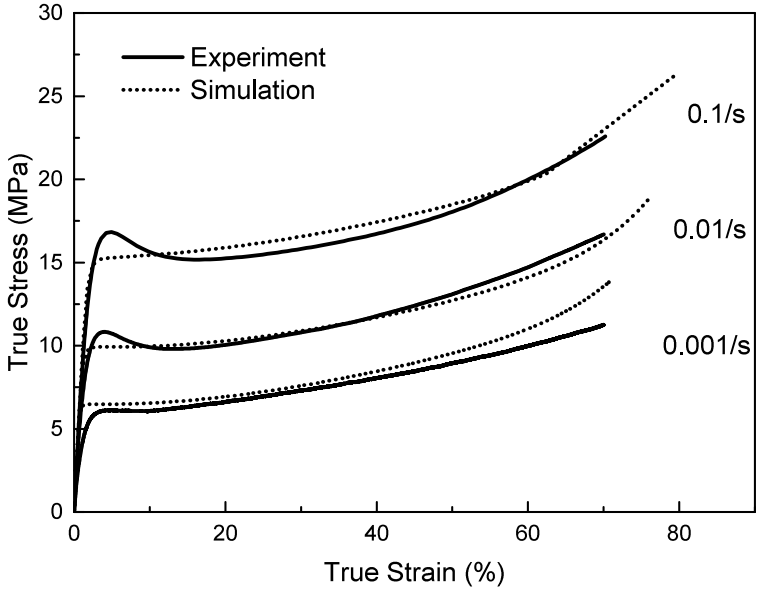

FIGURE 3.36: Simulation results versus tensile stress-strain curves at 100 °C.

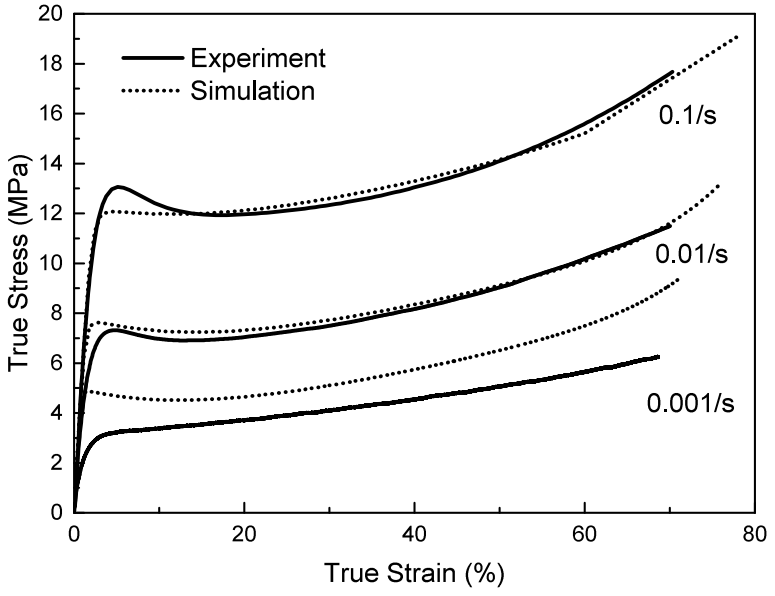

FIGURE 3.37: Simulation results versus tensile stress-strain curves at 105 °C.

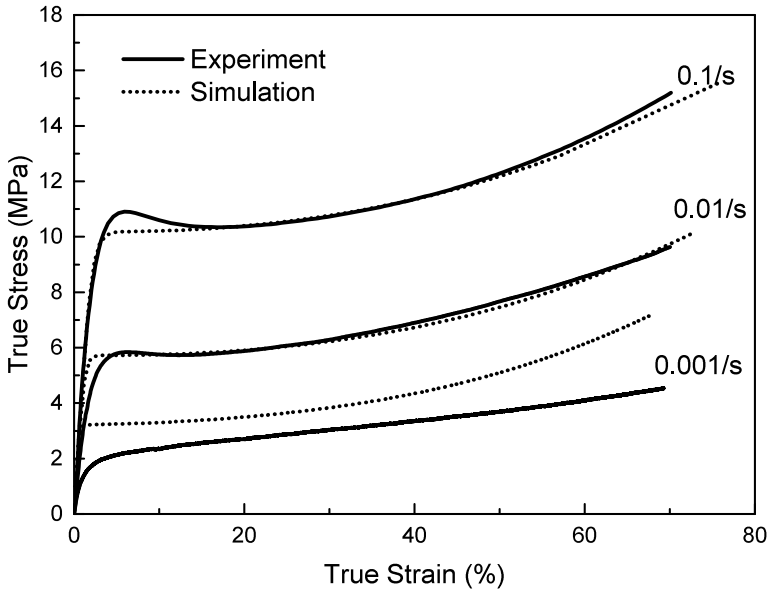

FIGURE 3.38: Simulation results versus tensile stress-strain curves at 107 °C.

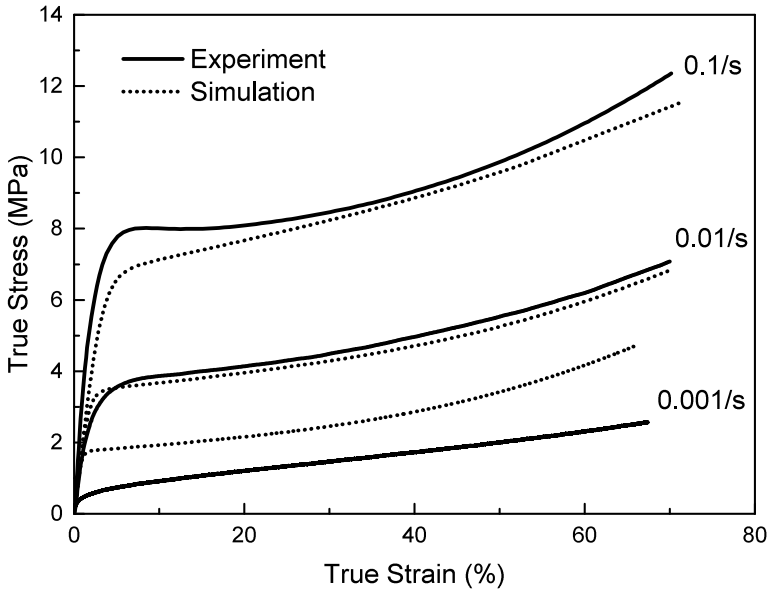

FIGURE 3.39: Simulation results versus tensile stress-strain curves at 110 °C.

3.5 Conclusions

DMA and tensile tests over a wide range of temperatures and strain rates have been used to investigate the influence of glass transitions on the thermo-mechanical behaviour of PMMA. It can be concluded that temperature and strain rate both significantly affect the thermo-mechanical behaviour of PMMA. These effects should be considered when optimising the parameters of R2R hot embossing.

For material calibrations, the DMA data was fitted with a generalised Maxwell viscoelastic model for temperatures ranging from 106 to 112 °C and frequencies ranging from 0.02 to 200 Hz. Moreover, the tensile test data for the temperatures ranging from 90 to 110 °C at strain rates of 0.001, 0.01 and 0.1/s were fitted to a parallel network model with viscoplastic components. The calibrated data agreed well with the experimental data. These calibrated parameters will be imported into simulations of R2R hot embossing.

Chapter 4

Experimental Trials of R2R Hot Embossing

4.1 Introduction

This chapter explores how process parameters affect the results of R2R hot embossing conducted on the Plexiglas 99524 PMMA films. Due to the variety of hot embossing processes and their requirements, it is difficult to define a general hot embossing cycle for all kinds of hot embossing processes. For each hot embossing cycle, the parameters need to be set up individually for different stamp designs and thermoplastics being embossed. The academic community has extensively explored the R2R hot embossing parameters for customised microfluidic chips [114, 128–131]. However, little research has been conducted to show how these parameters can be optimised for general microfluidic channel designs, such as straight channels and round reservoirs. We have conducted a set of R2R hot embossing experimental trials using our custom-designed generic shims and then evaluated the relevance of PMMA's thermo-mechanical behaviour to those process parameters.

4.2 Components of R2R Hot Embossing

The technical aspects of R2R hot embossing technique may vary with specific microfluidic platforms. The R2R hot embossing process has generally a few essential components:

- a flexible shim having features to be replicated
- an R2R hot embossing unit to integrate the heating unit
- a control unit to control process parameters and measure process values

These components affect the quality of R2R hot embossing in the different aspects:

- The surface roughness of the shim is important for ensuring uniform thickness over the entire embossing area. The type of stamp fabrication and polishing are vital factors to affect the surface roughness of the stamp.
- The influences of the R2R hot embossing unit includes heat- and force-induced strains and distortions, positioning accuracy of transverses.
- The precision of control and measurement can affect the final output of process parameters.

In addition, the choice of material in R2R hot embossing is dependent on several parameters, including the number of microfluidic chips, the optical, thermal and mechanical properties of the material being embossed. The process parameters of R2R hot embossing should be adjusted to different materials being used. In this project, process parameters were selected based on the experience from previous R2R hot embossing trials on the Plexiglas 99524 PMMA films [76].

The procedure of our R2R hot embossing trials is described as follows: First all the rollers start running at preset speed. The polymer film is fed into the R2R system through an unwinder roller. Afterwards the embossing roller and counter pressure roller are heated to the desired temperatures. When the temperatures on both rollers reach the correct

values, the embossing roller is moved vertically towards the counter pressure roller until a preset nip pressure is achieved. The nip pressure is provided by hydraulic pumps equipped with both embossing roller and counter pressure roller. The nip pressure is kept constant by a closed loop control system during the whole R2R hot embossing process. In our settings, 5 minutes of stabilisation time is given before the embossing step starts. Embossing and de-embossing work at the same time in R2R hot embossing because of the rolling movement. Cooling is achieved by setting a lower temperature on the counter pressure roller than the embossing roller in the healing step.

4.3 R2R Hot Embossing Facility at VTT

We have carried out all R2R hot embossing experimental trials at VTT Oulu, Ltd. using the pilot R2R production machines (Figure 4.1). The pilot machines consist of several R2R processing units, including a screen printing unit, a hot embossing unit, a lamination unit, a drying unit and a registration unit. Besides, there are several rollers to guide the film to roll in the correct direction.

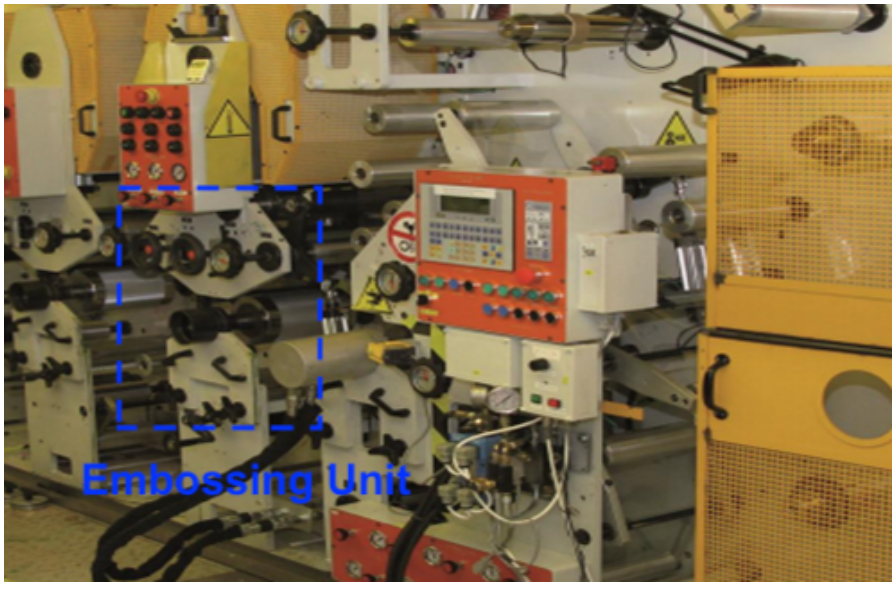

FIGURE 4.1: Picture of the 'PICO' pilot R2R production line, which includes an R2R hot embossing unit (indicated with blue dotted line). The machine is operated in an ISO7-standard clean room. Courtesy of VTT Oulu Ltd., Finland.

Prior research has substantiated the importance of preheating in the R2R hot embossing processes [70, 74]. Because the contact time between hot rollers and polymeric films is relatively short (in the order of a few milliseconds), a preheating process is always needed before the actual R2R hot embossing process. In this project, preheating was achieved by making contact between the hot roller and the polymer sheet before the polymer sheet was fed into the pressure nip. Figure 4.2 illustrates the roller arrangement which introduces preheating: Part (a) is an unwinder roller which unwinds the polymer sheet, and Part (c) is a winder roller which rewinds the polymer sheet to a roll. Part (b) contains an embossing roller and a counter pressure roller. The counter pressure roller was heated to around 85 °C, and the embossing roller was heated to approximately 107 °C. Part (d) is an additional set-up in the embossing unit. By changing the position of this roller, the preheating time can be adjusted. Figure 4.3 shows the actual image of the hot embossing unit. At an embossing speed of 0.5 m/min, the preheating time was 12 seconds [76]. The red marking line in Figure 4.3 indicates the first line of contact between the PMMA film and the embossing roller.

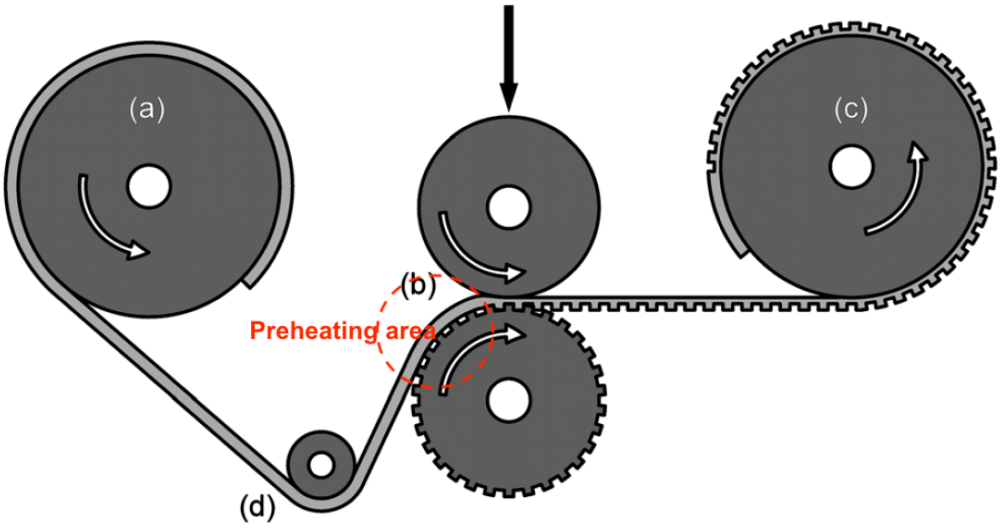

FIGURE 4.2: Schematic of the R2R hot embossing process flow by Liedert *et al* [76].

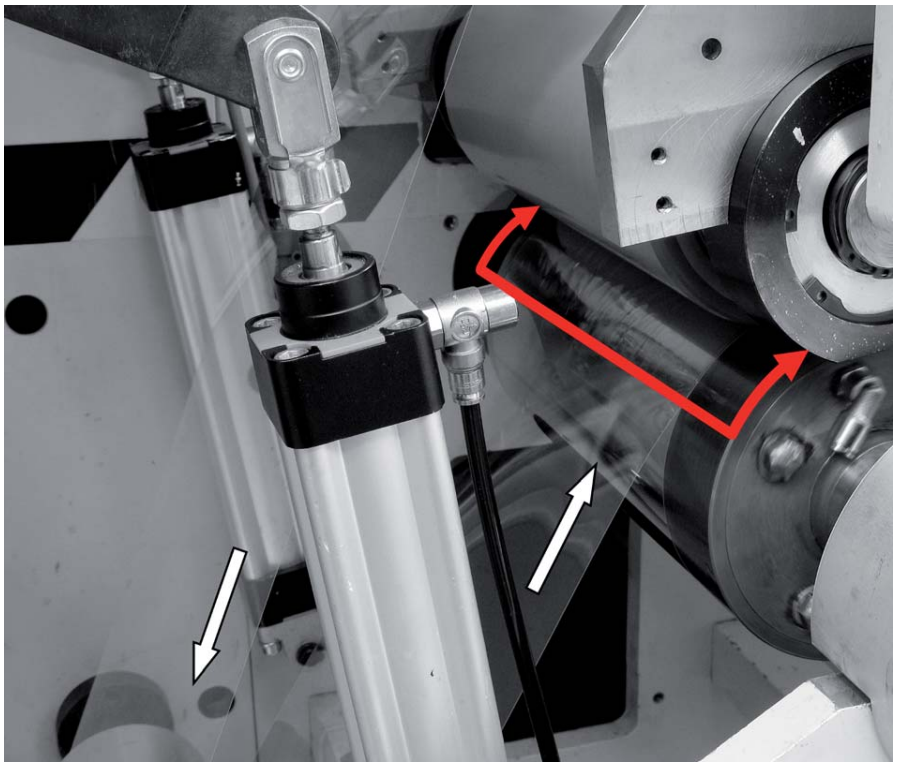

FIGURE 4.3: The hot embossing unit set of the 'MAXI' pilot R2R line at VTT Oulu, Ltd. *et al.* The white arrows indicate the polymer film's moving direction, and the red arrows indicate to the nip area where the polymer film is embossed.

4.4 R2R Hot Embossing on the PMMA Films

4.4.1 Generic Shim Fabrication

For this study, we made generic shims from stainless steel sheets by wet etching. All shims were cut into an area of 400 mm × 200 mm. The thickness was adjusted to 110 µm to meet the mechanical flexibility requirements in the following laser welding step. the shim pattern layout was drawn with a commercial CAD package (Rhino3D, McNeel, Spain). The features on the generic shims were designed to be positive so that microfluidic channels with the same layout could be embossed on the PMMA films.

Initially, two generic shims with the same feature layout were made during the fabrication process, one with 40 µm heights for all features and the other 80 µm. The shims we designed have explored four shapes for different microfluidic channel designs:

- Type A (Figure 4.4): Straight lines with different widths, which are the most simple geometries.
- Type B (Figure 4.5): V-shaped channels, to investigate the filling process at different directions.
- Type C (Figure 4.6): Coin-shaped, with two types of holes: round- and arc-shaped, to investigate the filling capability for circular geometries.
- Type D (Figure 4.7): Ladder-shaped, with increasing ladder heights, to show polymer flows in ascending stamp sizes.

Type A features include two sets of 15-mm-long, parallel, straight lines which were placed on the shim, one in the web moving direction and the other perpendicular to the web moving direction (see Figure 4.4). Each set consisted of 6 lines which were 20 µm, 50 µm, 100 µm, 200 µm, 500 µm, 1 mm wide, respectively, with a spacing of 9 times of each channel's width.

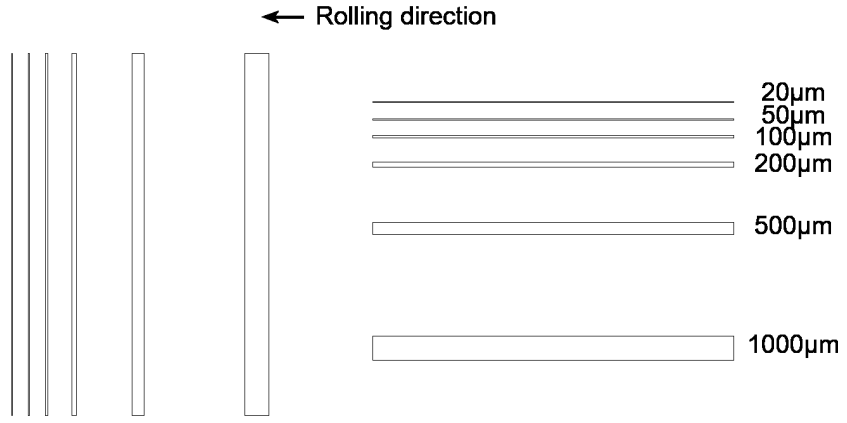

FIGURE 4.4: Layout of the generic shim showing Type A line feature widths. The microfluidic chip layout is the mirror image of the generic shim.

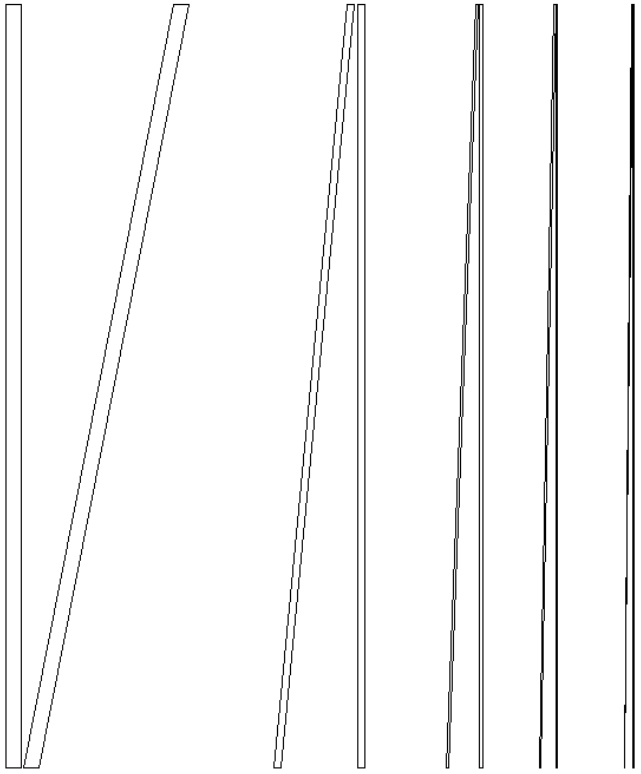

FIGURE 4.5: Schematic of Type B: V-shaped shim feature.

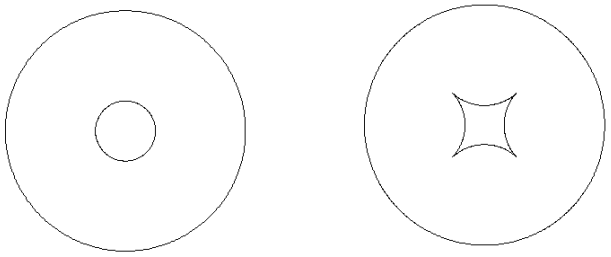

FIGURE 4.6: Schematic of Type C: coin-shaped shim feature.

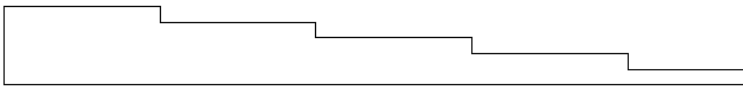

FIGURE 4.7: Schematic of Type D: ladder-shaped shim feature.

The surface profile data was collected with a stylus profilometer (Dektak 150, Veeco, USA). The data showed that the root-mean-square (Rq) roughness was 646.44 nm on the top surface of the 1-mm-wide line feature, which was acceptable for the fabrication of microfluidic channels. Figure 4.8 is a contour plot showing the top surface profile of the 1-mm-wide line feature. The flat surfaces between shim features were polished by hand for 4 hours with aluminium oxide powders. Figure 4.9 shows the profile of the flat shim surface. The Rq roughness of flat surfaces was measured as 351.42 nm. Then the generic shim was laser-welded into a cylindrical sleeve and attached to the embossing cylinder so that it could be used as the stamp for R2R hot embossing.

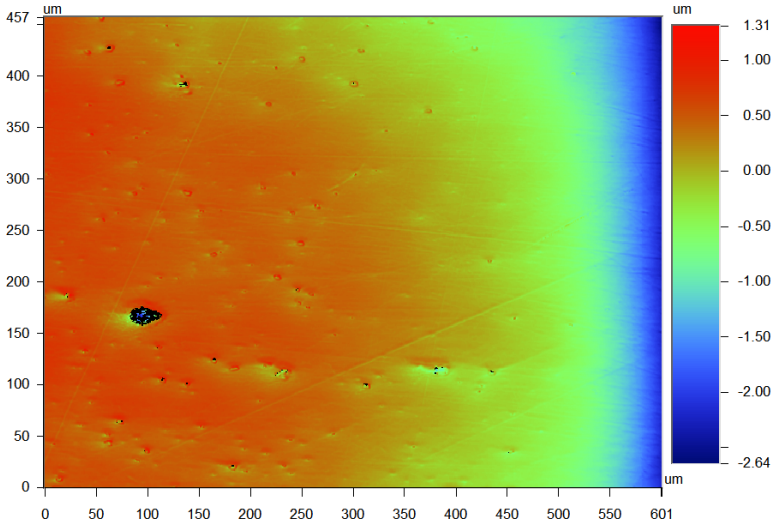

FIGURE 4.8: Contour plot showing the top surface profile of the 1-mm-wide line feature.

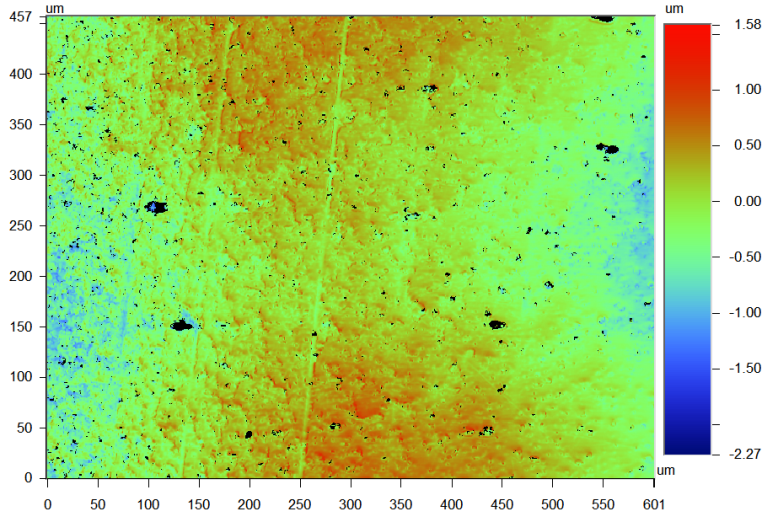

FIGURE 4.9: Contour plot showing the profile of the flat shim surface.

4.4.2 Experimental Parameters of R2R Hot Embossing Trials

A conventional, planar hot embossing cycle is defined with the following parameters [56]:

- heating rate
- touch force, moulding force
- moulding velocity
- holding time
- cooling time, cooling rate
- de-embossing temperature, de-embossing rate

Similarly, a R2R hot embossing cycle is defined with these parameters except that the holding time can be neglected. R2R hot embossing shares some parameters as above, however, there are a few differences. When the contact area becomes smaller while the pressure remains the same, the total force decreases. Since the contact area in R2R hot embossing is a straight line, the embossing force in R2R hot embossing is much lower than that in planar hot embossing. The de-moulding direction is not perpendicular to the stamp, which may cause the embossed parts to deform. The deformation is a function of the height of the embossing stamp and the diameters of the embossing roller.

The main R2R hot embossing unit dimensions were listed in Table 4.1:

TABLE 4.1: Main dimensions of the R2R hot embossing unit.

Properties		Value
Radius of the embossing roller	(mm)	65.186
Radius of the counter pressure roller	(mm)	65.186
Thickness of the steel shim	(µm)	110
Thickness of the PMMA film	(µm)	375
Height of all features on the shim	(µm)	40 / 80

4.4.3 Measurement Methods

Temperatures on the rollers were measured with an infrared thermometer. Stamp and embossed channel profiles were characterised with profilometers, either optical or stylus type.

The heights of the stamp features were characterised with an optical interferometer as shown in Figure 4.10 (Wyko NT3300, Veeco, USA). Optical interferometry is a technique in which two waves are superimposed with the same frequency to detect the patterns on the combined waveforms. The relative phase difference can be identified to show the distance between two channel planes. The interferometer measures the heights between different surfaces (bottom and top surfaces). In our study, the distance between the bottom and top surfaces were measured by the optical interferometer. Other information, such as the 'slope' lines were not captured by interferometry, because the previous etching step resulted in uneven surfaces being made on the slope. Several points were selected at the centre, starting and ending point of the channels. The polished area was then measured with the optical interferometer Wyko NT330 to evaluate the roughness information.

The stylus profilometer Dektak 150 was used to characterise the profiles of the embossed channels. The stylus head has a radius of 12.5 µm, which is mostly neglected as it is much smaller than the dimensions of the micro-channels. The scanning speed was 1 mm

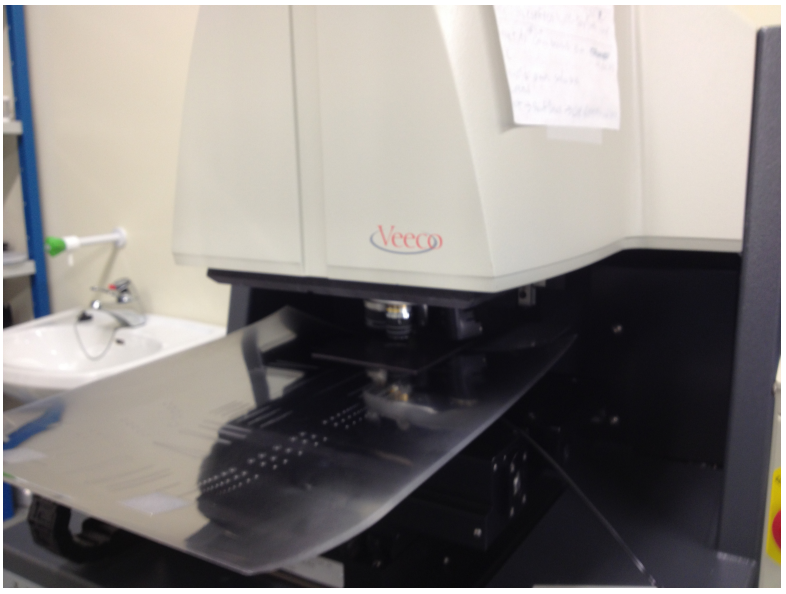

FIGURE 4.10: Steel shim characterisation using an optical interferometer (Wyko NT3300, Veeco, USA).

per second, with a scanning distance of 2 mm per scanning step. Stamp transfer rate was calculated by dividing the feature height on by the corresponding feature depth of the channel.

4.5 R2R Hot Embossing Experimental Trials on the PMMA Films

Prior studies of the R2R hot embossing processes on PMMA films were generally conducted at a range of temperatures from T_g ($\sim$ 105 °C) to 40-50 °C above T_g [37, 70, 83, 132]. However, our previous research showed that to get higher than 50% transfer rate, the temperatures need to be kept from T_g to 10 °C above T_g [76]. This is because at lower temperatures the PMMA is stiffer while at higher temperatures the PMMA's deformation may recover. We selected temperatures of the embossing roller to vary from 105 to 110 °C at every 1 °C, while the temperature of the counter pressure cylinder was kept at 85 °C. The embossing speed was 1.0 m/min, and the nip pressure between the two rollers was 30 bars following our previous settings [76].

Under the process parameters discussed above, a series of R2R hot embossing experimental trials were conducted on the 375-µm-thick Plexiglas 99524 PMMA films with the pilot R2R production line 'MAXI'. 6 minutes of stabilisation time was set at each isothermal embossing step to ensure that the temperatures of both rollers reached the preset values.

After these R2R hot embossing experimental trials, the PMMA web was cut into pieces of an area of 400 mm × 200 mm with a guillotine cutter and cleaned with a nitrogen gun. Then the PMMA pieces were cut into smaller pieces covering individual channel design types so that they could be measured with the stylus profilometer, Dektak 150.

4.6 Results and Discussions

4.6.1 Profiles of Shim Features

The average feature height on the shim was determined by 5 points along the edge of each feature. Figure 4.11 showed the 80-µm-high line feature profile compared to shim feature designs. The missing data for the sidewalls was due to the limitation of the optical profilometer measurements. The shim fabrication method we used failed to achieve the 80-µm-high relief target for the line features and other features, with an average relief height of approximately 103 µm. This may be caused by inappropriate etching time control during the wet etching process. Therefore, we did not further investigate the shim profiles of 80-µm-high shim and R2R hot embossing results.

For the 40-µm-high shim design, the actual heights of the wet-etched line features have been kept close to the target values (see Figure 4.12). The average measured heights of Type A line features are illustrated in Figure 4.13. The largest average height results were at 200 µm and perpendicular to the rolling direction. The maximum height was 43.35 µm at 100 µm and parallel to the rolling direction. Nevertheless, most of the results were between 40 and 43 µm.

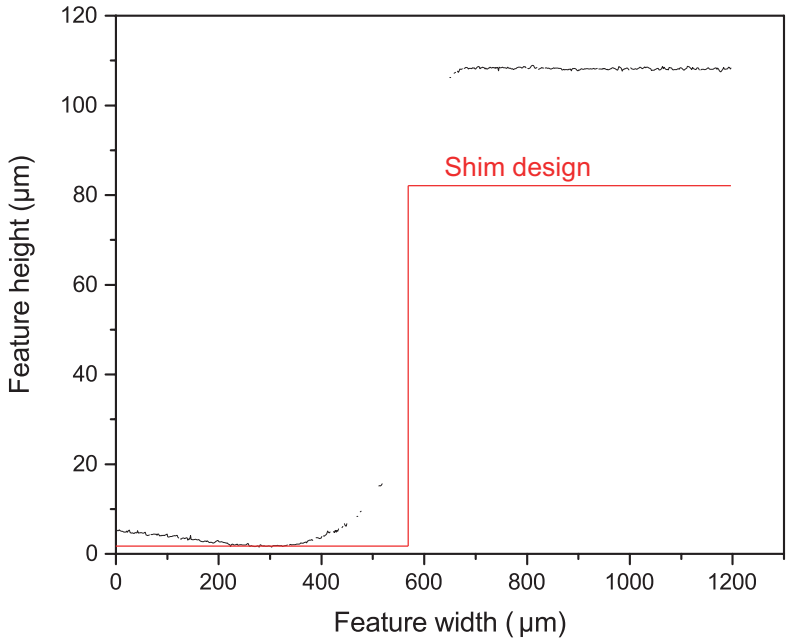

FIGURE 4.11: One selected profile of 80-µm-high line feature measured by optical interferometry.

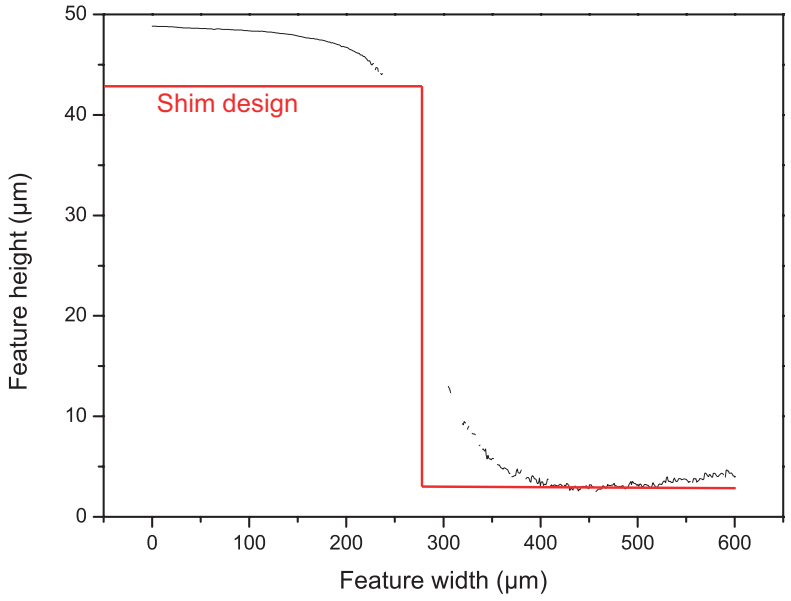

FIGURE 4.12: One selected profile of 40-µm-high line feature measured by optical interferometry.

Figure 4.14 and Figure 4.15 present the measured feature heights on the generic shim including 20 µm, 50 µm, 100 µm, 200 µm, 500 µm and 1 mm feature widths in the directions perpendicular and parallel to the web rolling direction, respectively. Generally, all stamp line features no narrower than 50 µm were etched to the designed 40 µm relief height, while the 20-µm-wide channels were etched to around 12.65 µm (Figure 4.16), and the

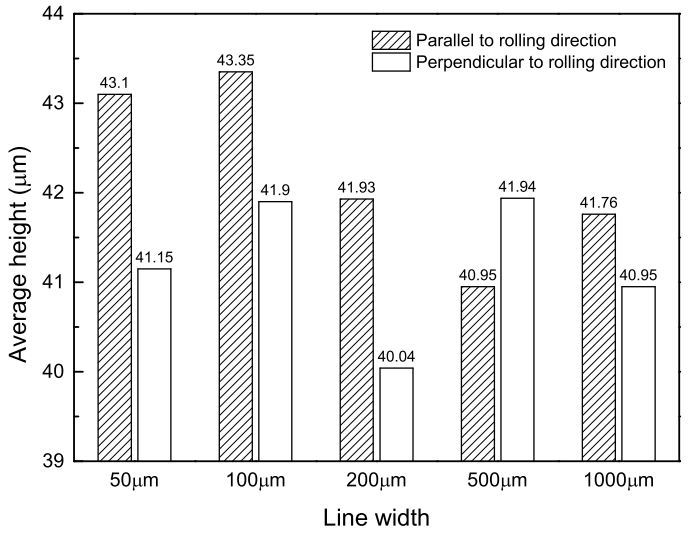

FIGURE 4.13: Average feature heights of Type A line features.

top surface was not flat as in other line features. There is no significant difference in depths between stamp features perpendicular and parallel to the rolling directions. The optical profilometer could not capture the whole profiles of feature walls, however we can get limited information from the interferometry data that the etched feature walls are not vertical but in a slope.

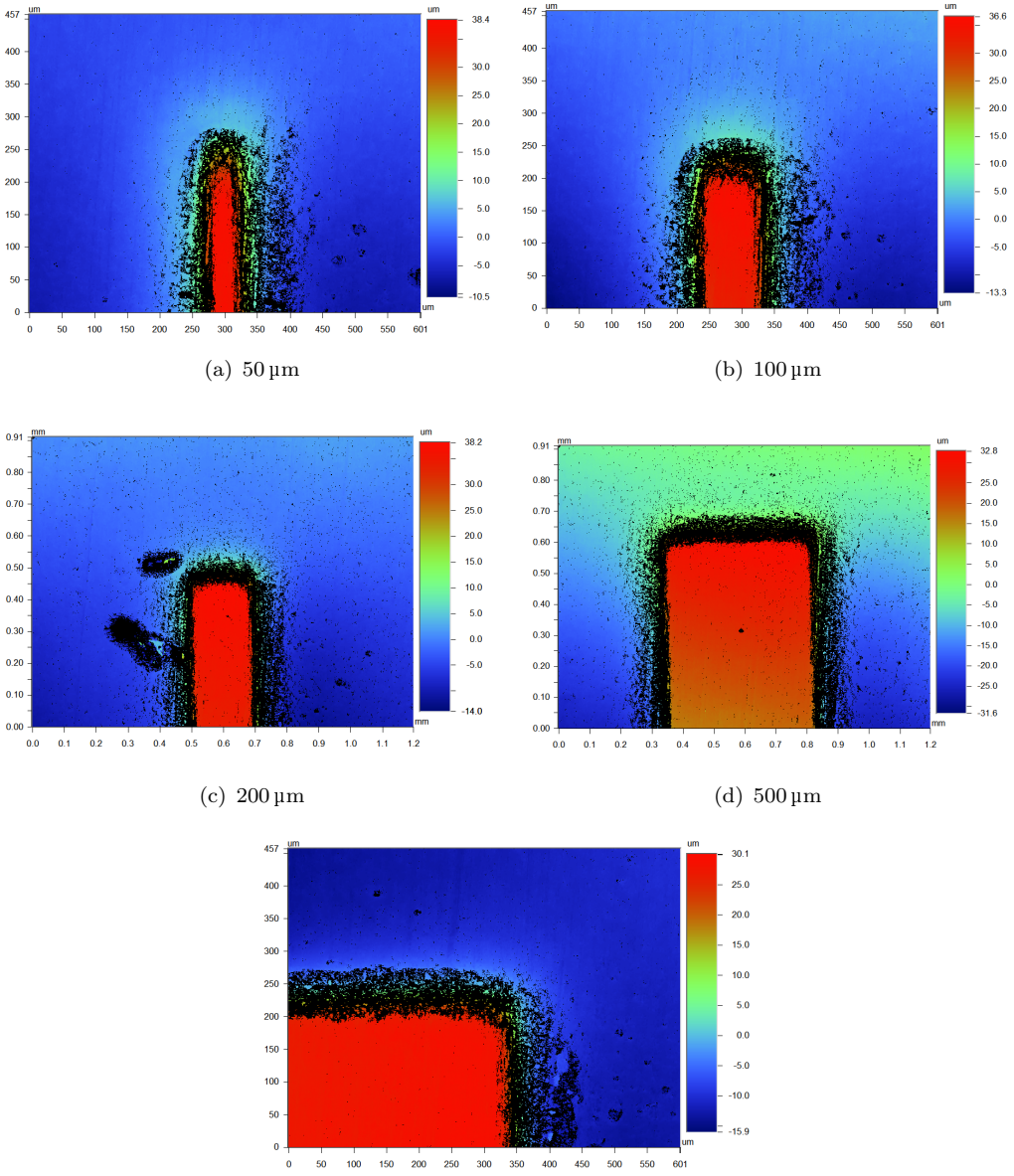

(a) 50 µm (b) 100 µm

(c) 200 µm (d) 500 µm

(e) 1 mm

FIGURE 4.14: Contour plot showing the surface profile of line features parallel to the rolling direction.

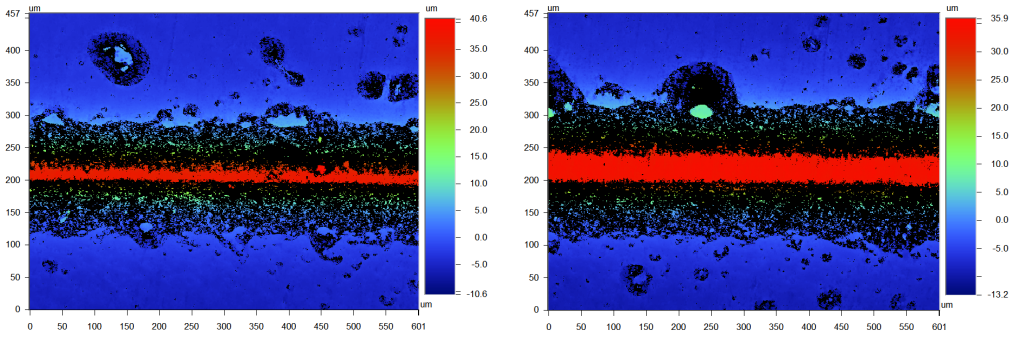

(a) 50 µm

(b) 100 µm

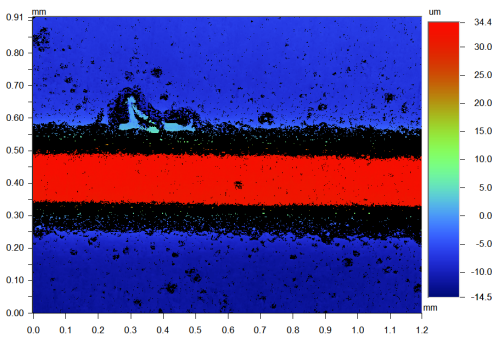

(c) 200 µm

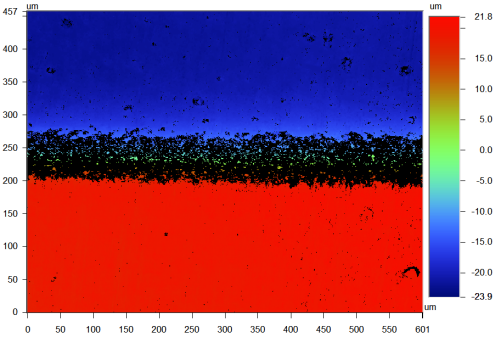

(d) 500 µm

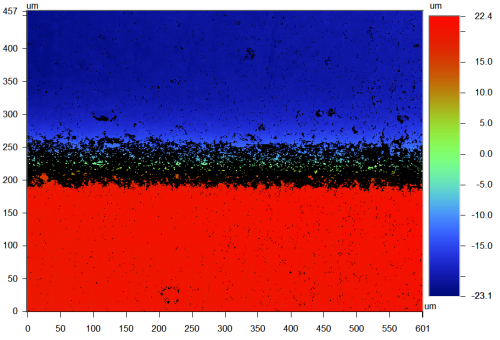

(e) 1 mm

FIGURE 4.15: Contour plot showing the surface profile of line features perpendicular to the rolling direction.

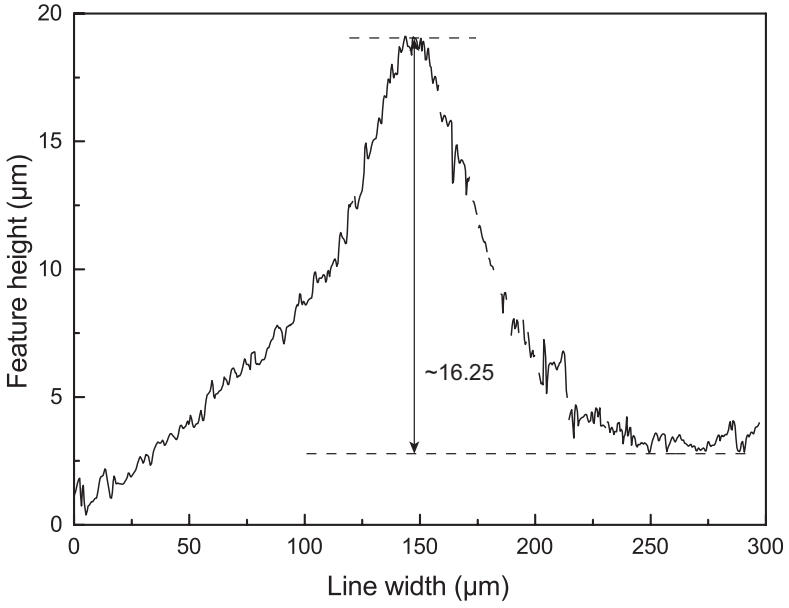

FIGURE 4.16: Cross-sectional profile of 20-μm-wide line feature.

For Type B, C and D shim features, the feature relief heights are shown in Figure 4.17, 4.18 and 4.19. In the planar surface, all these features showed good replication of the designed shape. In the vertical direction, only V-shaped Type C line features had achieved the 40 µm height target. However, for Type C and D features, the etched feature height were below 20 µm.

The height differences between 40- and 80-µm features could be attributed to the limitation of our current wet etching process. The profile differences between different feature shapes to etching time may only be attributed to the etching time, as it takes more time to etch through a closed feature (such as a hole in the 'coin' shape) than an open feature (such as a line feature).

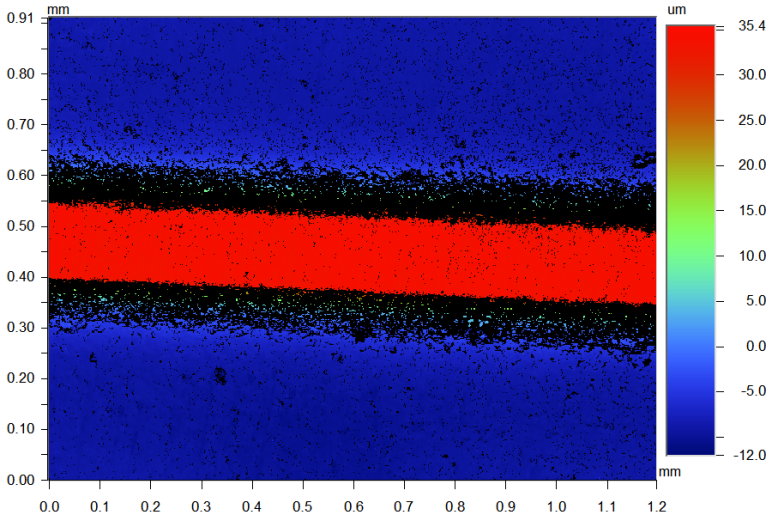

FIGURE 4.17: Contour plot showing the surface profile of Type B.

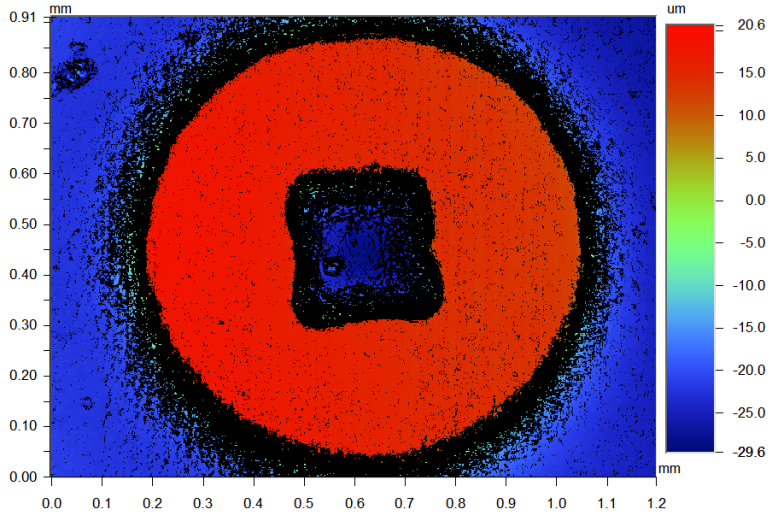

FIGURE 4.18: Contour plot showing the surface profile of feature Type C.

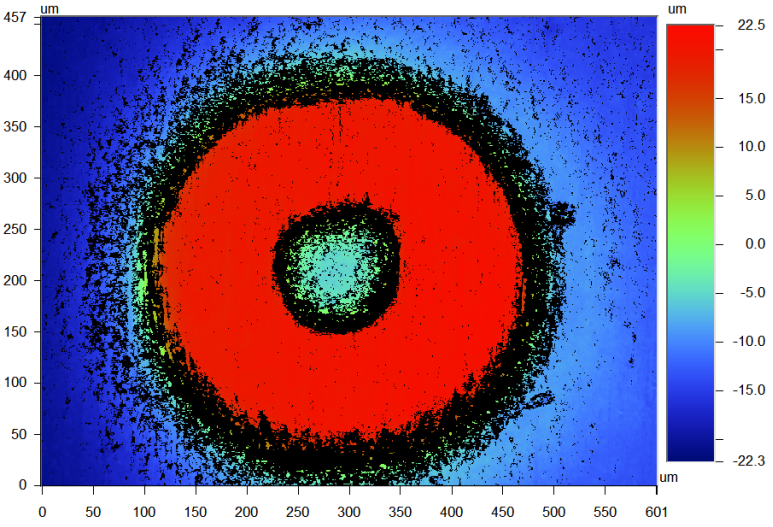

FIGURE 4.19: Contour plot showing the surface profile of feature Type C.

4.6.2 Profiles of R2R-Hot-Embossed Features

Figure 4.20 displays the profile of embossed channel profiles including features of 20-, 50-, 100-, 200-, 500- and 1000-µm-wide. The channel depth of 500- and 1000-µm-wide channel were fabricated to a depth of around 17 µm. The 200-µm-wide channel was approximately 12 µm deep, the 50-µm- and 100-µm-wide channel were approximately 10 µm deep.

Only the channel of 1 mm width had the clear, straight profile, while other five line features were interfering with each other. This phenomenon applies to the features both

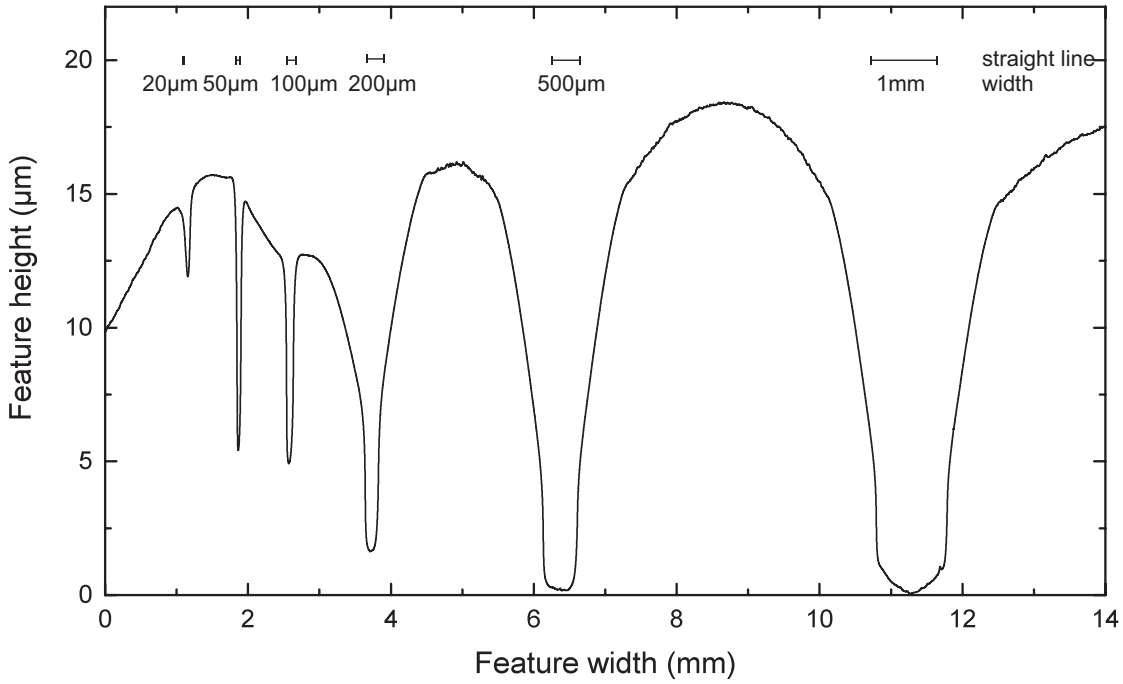

FIGURE 4.20: Profile of embossed line features at 107 °C.

parallel and perpendicular to the rolling direction. The embossed feature depths of 1-mm-wide channels were measured as 12.5 to 20.5 µm (Figure 4.21). We found that there was a difference in heights between the features in both directions. With the same designed channel width, the depths of features parallel to the rolling direction were higher than those perpendicular to the rolling direction. The difference in feature depths could be caused by the difference in the pressure distribution between features in different directions.

The profiles of features parallel to the rolling directions are displayed in Figure 4.22. From 105 °C the channel depth increased with temperature. At 109 °C the embossed profile reached the highest cavity depth of 20.5 µm. As the temperature continued to increase, at 110 °C, the depth decreased to slightly below the depth at 108 °C. It indicates that one-degree change in the temperature can result in a significant change in the embossing depth while other process parameters remain the same. In current experimental settings, 109 °C is the optimum temperature. This is because at lower temperatures the filling stage is more difficult than that at higher temperatures, and at higher temperatures PMMA recovers too much after the R2R hot embossing. None of the four temperature settings achieved a transfer rate of more than 51.3%, compared

to 58% transfer rate in Liedert *et al.*'s work. In the planar hot embossing process, the transfer rate can reach 100% when the embossing time is long enough for the material to fill the stamp cavity. It should be taken into consideration that the contact time is much shorter in R2R hot embossing than that in planar hot embossing.

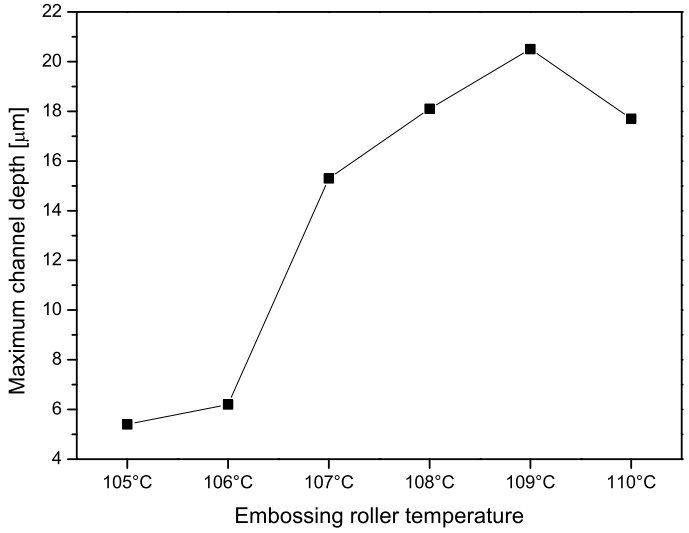

FIGURE 4.21: 1-mm-wide channel depths at different embossing roller temperatures.

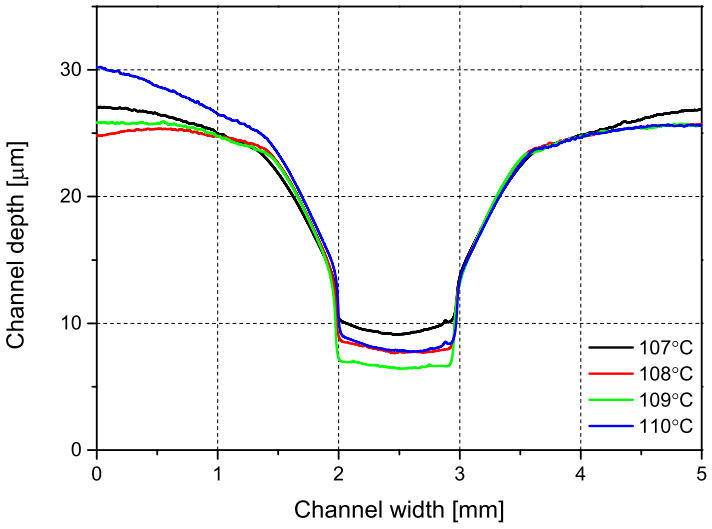

FIGURE 4.22: Profiles of embossed channels parallel to the rolling direction versus different embossing roller temperatures.

It has been found that there is a slight difference in heights between the features on directions parallel and perpendicular to the rolling direction. With the same designed

channel width, the depths of features parallel to the rolling direction were 1 - 2 µm higher than those perpendicular to the rolling direction. This can be caused by the pressure difference in the pressure distribution between features in different directions.

For the current R2R hot embossing setting, the transfer rate has been achieved by no more than 51.3%. This is particularly low compared to the planar hot embossing. In planar hot embossing, 100% transfer rate can be achieved with long holding time. For R2R hot embossing, the contact time between the embossing stamp and the polymer film is relatively short, therefore the polymer may not fill the stamp cavity completely. In addition, the transfer rate depends on the parameters of the R2R hot embossing, including the temperature, nip pressure, rolling speed, and the pre-heating time. We expect the designed channel depth to be modified according to the transfer rate in the actual R2R hot embossing process. It should also be noted that the R2R hot embossing is not suitable for creating features of high aspect ratios.

The design rules for the forming tools are strongly based on experiences. The R2R hot embossing trial results suggest that the spacing and shape of features should be adjusted so that the polymer can flow into the cavity. With a lot of features on the shim, it is hard to replicate every feature on the shim. The central region of the shim has higher transfer rate than those near the edge of the shim, as the central region gets the target nip pressure distribution. We suggest that process engineers consider putting main features in the centre region of the shim layout.

4.7 Conclusions

We have demonstrated a series of trial experiments of the R2R hot embossing process based on our custom-designed shims at different embossing temperatures from 105 to 110 °C. The results of such R2R hot embossing trials have shown the effects of embossing temperature and line widths on the final profile of embossed microfluidic channels. The highest transfer rate achieved was 51.3% at 109 °C.

Unfortunately, the R2R hot embossing trials failed to demonstrate the effects of specific geometries such as V-shaped and coin-shaped geometries on the profile of the embossed patterns. There remains much work to be done to design a new generic shim with lower pattern density. To further understand the thermo-mechanical behaviour of PMMA during R2R hot embossing, numerical methods can be used, which will be discussed in the following chapter.

Chapter 5

Finite Element Simulation of R2R Hot Embossing

5.1 Introduction

This chapter introduces the finite element (FE) simulations for fabricating microfluidic channels during R2R hot embossing. The FE simulations are aimed at solving three major issues. First, the experimental approach of finding the appropriate process parameters of R2R hot embossing is both time- and cost-consuming. Second, previously reported simulations are mostly for planar hot embossing and lack suitable definition of boundary conditions for the R2R hot embossing process. Third, according to our findings reported in Chapter 3, one degree change in the temperature could result in a significant change in PMMA's behaviour, however most existing simulations set a temperature increment of 10 °C or larger. We present the numerical results of FE simulations including the deformed shapes of PMMA film and highest cavity depth versus temperature curves, and compare these results against corresponding experimental results.

As a sophisticated engineering process, the R2R hot embossing has several challenges for simulations: (a) the material being embossed is usually rate-and temperature-dependent,

therefore suitable material models capable of representing the thermo-mechanical behaviours at certain strains, strain rates and temperatures are necessary; (b) the results of R2R hot embossing are affected by a lot of process parameters, such as the embossing temperatures, the nip pressure and the rolling speed, which increases the simulation complexity; (c) due to the rolling movement, there is no holding stage in the R2R hot embossing process, and the simulation time should be adjusted according to the contact time between the flexible stamp and the thermoplastic film. To obtain a basic understanding of the mechanics of R2R hot embossing, we made the following simplifications: (a) the embossing roller welded with the generic shim and the counter pressure roller were treated as rigid parts; (b) the PMMA film was assumed to have uniform thickness and mechanical properties; (c) the PMMA film was heated to the temperature at the beginning of simulations, and the temperature remained constant during embossing; (d) the simulation time step was set to match the contact time between the shim features and the PMMA shim.

5.2 Methods

In the planar hot embossing, the stamp is pressed into the thermoplastic film with an embossing pressure and held for a period of time until the thermoplastic material completely fills in the stamp cavity. Then the stamp is released from the thermoplastic film. The R2R hot embossing process differs from the planar hot embossing process in the registration method of the features on the master. A constant nip pressure ensures that the thermoplastic film is sandwiched between the embossing roller and the counter pressure roller. The de-embossing stage in R2R hot embossing is also different due to the rolling movement of the roller, thus there is no holding stage in the R2R hot embossing process.

For the FE simulation of such process, we began by simulating the embossing process of a straight line feature on the generic shim. The shim features (stamps) had a height of around 40 µm in the vertical direction, which was substantially lower than the radius

of the rollers (65.186 mm). Therefore we modelled the relative movement between the stamp feature and the PMMA film in the vertical direction. The contact time between the stamp and the PMMA film was calculated by dividing the feature width (in the rolling direction) by the web moving speed.

As listed in Table 3.1, the Young's modulus of the PMMA film is 2.2 GPa, while the stainless steel stamp (of which the Young's modulus is around 200 GPa) is ∼100 times stiffer. As a result, the stamp was modelled as an analytical rigid part, while the PMMA layer was modelled as a deformable solid part.

The feature dimensions were in the order of ∼10 to 100 µm, while the PMMA film was 200 mm wide. For ease of investigation, we considered a plane strain, symmetric model in which a rectangular-shaped stamp (cross-section of a line feature) was pressed into the PMMA film to create a cavity, as shown in Figure 5.1. The stamp was modelled with a vertical wall and a rounded lower corner. The stamp was constrained in the horizontal direction and free to move in the vertical direction. For the PMMA layer, the right and left edges (AB and CD) were constrained in the vertical direction, while the bottom edge (BC) was fixed in both horizontal and vertical directions.

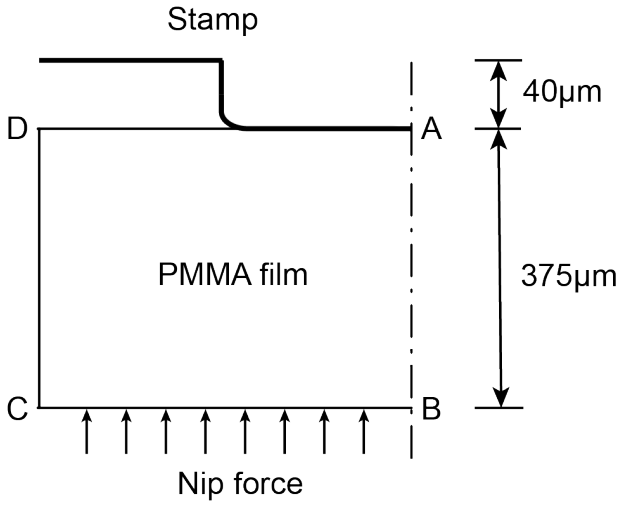

FIGURE 5.1: Schematic of the plane strain, symmetric model.

The line force F_L applied on the stamp can be calculated as follows:

$$F_L = \frac{F_{tot}}{L_N}[N/mm] \tag{5.1}$$

$$F_{tot} = P \cdot L_N \cdot W_N \tag{5.2}$$

Therefore the line force F_L is:

$$F_L = P \cdot W_N \tag{5.3}$$

where P is the nip pressure, F_{tot} is the total force which is applied to the rollers, L_N is the contact length, W_N is the contact width. In this case $P = 30$ bars $= 3$ MPa, $W_N = 1$ mm, $L_N = 15$ mm. The line force is 3 N/mm, and the total force is 45 N.

Frictional contact between the stamp and polymer film was defined in the FE model following previous work made by Worgull *et al.* [30] and Ames *et al.* [116]. For all FE simulations we assumed a friction coefficient of 0.75. The results were compared to those using different friction coefficients (0.25, 0.5) and frictionless contact.

Isothermal simulations were conducted for the temperatures 90, 100, 105, 107 and 110 °C. It should be noted that thermal expansion takes place during the heating process, however, in the simplified isothermal simulations, the effect of thermal expansion was then omitted.

For the material model implementation we employed the Polymer User Model (PolyUMod) library developed by Veryst Engineering, USA. The PolyUMod acted as a built-in material model library in Abaqus/Standard. The deformed shapes of the channels and the measured maximum channel depth from the deformed shapes were exported and compared to the experimental results of R2R hot embossing. A summary of the FE simulations were presented followed by suggestions for optimising the process parameters of R2R hot embossing.

5.3 Procedures

The FE program Abaqus/Standard together with the PolyUMod library were used to simulate the R2R hot embossing of PMMA. A Python script was written to automatically generate Abaqus input files, including definitions of geometries, materials, meshes, steps, interactions, boundary conditions and other related simulation components.

First we import all the necessary Abaqus modules into the Python working environment:

```
from part import *
from material import *
from section import *
from assembly import *
from step import *
from interaction import *
from load import *
from mesh import *
from optimization import *
from job import *
from sketch import *
from visualization import *
from connectorBehavior import *
```

Next we need to create two parts for the 2D symmetric model, one named 'Stamp' and the other named 'Film'. We define the line feature width w, line feature height h, simulation time t and friction coefficient k.

```
w = 1.0  # Line feature width in millimetres
h = 0.04  # Line feature height in millimetres
t = 0.06  # Simulation time, in seconds
k = 0.75  # Friction coefficient
```

The geometries were created based on the generic shim designs. For different straight lines, the PMMA layer widths ('BC' side as indicated in Figure 5.1) were double the width of the straight line feature. The stamp feature height was fixed to 40 µm, while

the thickness of the PMMA layer was fixed to 375 µm ('AB' side as indicated in Figure 5.1). The width of the 5 models were created with respect to the 5 line features having a width of 50, 100, 200, 500 and 1000 µm, respectively.

```
# Part 1: Stamp
mdb.models['Model-1'].ConstrainedSketch(name='Sketch-1', sheetSize=0.5)
mdb.models['Model-1'].sketches['Sketch-1'].Line(point1=(0.0, h), point2=(
        w/2, h))
mdb.models['Model-1'].sketches['Sketch-1'].HorizontalConstraint(
        addUndoState=False, entity=
        mdb.models['Model-1'].sketches['Sketch-1'].geometry[2])
mdb.models['Model-1'].sketches['Sketch-1'].Line(point1=(w/2, h), point2=(
        w/2, 0.0))
mdb.models['Model-1'].sketches['Sketch-1'].VerticalConstraint(addUndoState=
        False, entity=mdb.models['Model-1'].sketches['Sketch-1'].geometry[3])
mdb.models['Model-1'].sketches['Sketch-1'].PerpendicularConstraint(
        addUndoState=False, entity1=
        mdb.models['Model-1'].sketches['Sketch-1'].geometry[2], entity2=
        mdb.models['Model-1'].sketches['Sketch-1'].geometry[3])
mdb.models['Model-1'].sketches['Sketch-1'].Line(point1=(w/2, 0.0), point2=(
        w+0.02, 0.0))
mdb.models['Model-1'].sketches['Sketch-1'].HorizontalConstraint(
        addUndoState=False, entity=
        mdb.models['Model-1'].sketches['Sketch-1'].geometry[4])
mdb.models['Model-1'].sketches['Sketch-1'].PerpendicularConstraint(
        addUndoState=False, entity1=
        mdb.models['Model-1'].sketches['Sketch-1'].geometry[3], entity2=
        mdb.models['Model-1'].sketches['Sketch-1'].geometry[4])
mdb.models['Model-1'].sketches['Sketch-1'].FilletByRadius(curve1=
        mdb.models['Model-1'].sketches['Sketch-1'].geometry[3], curve2=
        mdb.models['Model-1'].sketches['Sketch-1'].geometry[4], nearPoint1=(
        w/2, 0.01), nearPoint2=(w/2+0.01,
        0), radius=0.01)
mdb.models['Model-1'].Part(dimensionality=TWO_D_PLANAR, name='Stamp', type=
        ANALYTIC_RIGID_SURFACE)
mdb.models['Model-1'].parts['Stamp'].AnalyticRigidSurf2DPlanar(sketch=
        mdb.models['Model-1'].sketches['Sketch-1'])
del mdb.models['Model-1'].sketches['Sketch-1']
```

```
# Part 2: Film
mdb.models['Model-1'].parts['Stamp'].ReferencePoint(point=
        mdb.models['Model-1'].parts['Stamp'].vertices[0])
mdb.models['Model-1'].ConstrainedSketch(name='Sketch-1', sheetSize=0.5)
mdb.models['Model-1'].sketches['Sketch-1'].rectangle(point1=(0.0, 0.0),
        point2=(w, -0.375))
mdb.models['Model-1'].Part(dimensionality=TWO_D_PLANAR, name='Film', type=
        DEFORMABLE_BODY)
mdb.models['Model-1'].parts['Film'].BaseShell(sketch=
        mdb.models['Model-1'].sketches['Sketch-1'])
del mdb.models['Model-1'].sketches['Sketch-1']
```

We employed two models, the generalised Maxwell viscoelastic model and the parallel network model to describe the material properties, as discussed in Chapter 3. For the generalised Maxwell model we input the Prony series as listed in Table 3.3. The following script sets an example of the calibrated viscoelastic parameters at 105 °C:

```
mdb.models['Model-1'].Material(name='PMMA-Viscoelastic-105C')
mdb.models['Model-1'].materials['PMMA-Viscoelastic-105C'].Density(table=((
        1.16e-09, ), ))
mdb.models['Model-1'].materials['PMMA-Viscoelastic-105C'].Elastic(table=((
        727.29265, 0.37), ))
mdb.models['Model-1'].materials['PMMA-Viscoelastic-105C'].Viscoelastic(domain=
        TIME, time=PRONY, table=((0.29101,0.0, 0.001),
        (0.18401,0.0, 0.01), (0.21864,0.0,0.1), (0.26656, 0.0,1)))
```

The following script is another example which specifies the parameters required to define the parallel network model within the PolyUMod library as listed in Table 3.4:

```
mdb.models['Model-1'].Material(name='PN_105C')
mdb.models['Model-1'].materials['PN_105C'].Density(table=((1.16e-09, ), ))
mdb.models['Model-1'].materials['PN_105C'].UserMaterial(mechanicalConstants=(
        14,0,0,0,0,1,0,0,0,0,36,13,1,500,0,0,
        5,1.21549950907072,-0.1967068953001,0.04499627910002,500,
        5,96.12293968124,2.12712195472232,
        1.27662085509362,500,507,15.7778420738468,5.09681684308724,
```

```
        3.33293350743603,0.11009666681041,803,
        12.6189935164014,5.23577744443703,-0.3950461695593,0.86487469334328))
mdb.models['Model-1'].materials['PN_105C'].Depvar(n=13)
```

For each model there were 5 isothermal simulations jobs, each was implemented with the calibrated viscoplastic model parameters for temperatures 90, 100, 105, 107 and 110 °C, as listed in Table 3.4, Chapter 3.

For the process steps, at first the stamp was in contact with the PMMA layer and ready for hot embossing. Then a pressure load was applied to the contact area between the stamp and the PMMA layer. As the stamp moved into the PMMA layer, a channel was formed, and as time went on, the pressure was released from the stamp. The PMMA channel may encounter some recovery after the stamp was released. Similarly, the simulation process was composed of two steps. In the initial step, the substrate and stamp were instanced and assembled. The bottom edge of the stamp initially rested on the top surface of the PMMA layer. The next step included nonlinear geometry and was to simulate the embossing and de-embossing processes in R2R hot embossing. The step time was calculated by dividing the line width by the web moving speed. We started with the web moving speed of 1.0 m/min following the R2R hot embossing experiments (Table 5.1).

TABLE 5.1: Simulation step time versus line width.

Step time (seconds)	Line width (µm)
0.06	1000
0.03	500
0.012	200
0.006	100
0.003	50

The PMMA layer was meshed with 4-node plane strain quadrilateral, reduced integration (CPE4R) elements. The model consisted of 210, 430, 820, 1901, 3801 CPE4R elements for the 50 µm, 100 µm, 200 µm, 500 µm and 1 mm lines. Figure 5.2 demonstrates one of the automatically generated geometries and meshes for our FE simulations.

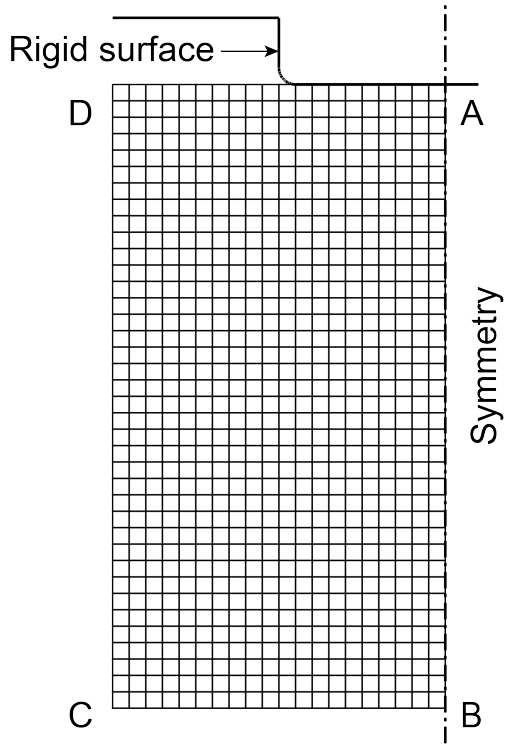

FIGURE 5.2: Geometry and finite element meshes for the FE simulation. This example is for a 200 µm line feature.

All FE simulations were conducted on a 3.7 GHz dual-core (Intel Core i3-6100) computer with 8 GB of RAM. The solving time was between 400 and 450 seconds for each line feature.

The following the Python codes define the section, sets, surfaces, mesh, assembly, steps, interactions, boundary conditions, output requests and jobs as previously discussed:

```
# Section
mdb.models['Model-1'].HomogeneousSolidSection(material='PN_90C'
        , name='PMMASection', thickness=None)
mdb.models['Model-1'].parts['Film'].SectionAssignment(offset=0.0, offsetField=
        '', offsetType=MIDDLE_SURFACE, region=Region(
        faces=mdb.models['Model-1'].parts['Film'].faces.findAt(((0.0, 0.0,
        0.0), (0.0, 0.0, 1.0)), )), sectionName='PMMASection',
        thicknessAssignment=FROM_SECTION)

# Sets & Surfaces
mdb.models['Model-1'].parts['Film'].Set(edges=
        mdb.models['Model-1'].parts['Film'].edges.findAt(((0.0, -0.01, 0.0), )),
```

```
        name='Left edge')
mdb.models['Model-1'].parts['Film'].Set(edges=
        mdb.models['Model-1'].parts['Film'].edges.findAt(((w, -0.01, 0.0), )),
        name='Right edge')
mdb.models['Model-1'].parts['Film'].Set(edges=
        mdb.models['Model-1'].parts['Film'].edges.findAt(((0.01, -0.375, 0.0), )),
        name='Bottom edge')
mdb.models['Model-1'].parts['Film'].Set(edges=
        mdb.models['Model-1'].parts['Film'].edges.findAt(((0.01, 0.0, 0.0), )),
        name='Top edge')
mdb.models['Model-1'].parts['Film'].Surface(name='Top surface', side1Edges=
        mdb.models['Model-1'].parts['Film'].edges.findAt(((0.01, 0.0, 0.0), )))
mdb.models['Model-1'].parts['Film'].Surface(name='Bottom surface', side1Edges=
        mdb.models['Model-1'].parts['Film'].edges.findAt(((0.01, -0.375, 0.0), )))
mdb.models['Model-1'].parts['Stamp'].Surface(name='Stamp surface', side2Edges=
        mdb.models['Model-1'].parts['Stamp'].edges.findAt(((0.01, h, 0.0), )))

# Mesh
mdb.models['Model-1'].parts['Film'].setMeshControls(elemShape=QUAD, regions=
        mdb.models['Model-1'].parts['Film'].faces.findAt(((0.01, -0.01, 0.0),
        )), technique=STRUCTURED)
mdb.models['Model-1'].parts['Film'].setElementType(elemTypes=(ElemType(
        elemCode=CPE4R, elemLibrary=STANDARD, secondOrderAccuracy=OFF,
        hourglassControl=ENHANCED, distortionControl=DEFAULT), ElemType(
        elemCode=CPE3, elemLibrary=STANDARD)), regions=(
        mdb.models['Model-1'].parts['Film'].faces.findAt(((0.01, -0.01, 0.0),
        )), ))
mdb.models['Model-1'].parts['Film'].seedPart(deviationFactor=0.1,
        minSizeFactor=0.1, size=0.01)
mdb.models['Model-1'].parts['Film'].generateMesh()

# Assembly
mdb.models['Model-1'].rootAssembly.DatumCsysByDefault(CARTESIAN)
mdb.models['Model-1'].rootAssembly.Instance(dependent=ON, name='Film-1', part=
        mdb.models['Model-1'].parts['Film'])
mdb.models['Model-1'].rootAssembly.Instance(dependent=ON, name='Stamp-1', part=
        mdb.models['Model-1'].parts['Stamp'])

# Steps
mdb.models['Model-1'].StaticStep(initialInc=t/10, maxNumInc=1000, minInc=t*1e-05
        , name='Apply pressure', nlgeom=ON, previous='Initial',timePeriod=t)
```

```
# Interactions
mdb.models['Model-1'].ContactProperty('Friction')
mdb.models['Model-1'].interactionProperties['Friction'].TangentialBehavior(
        dependencies=0, directionality=ISOTROPIC, elasticSlipStiffness=None,
        formulation=PENALTY, fraction=0.005, maximumElasticSlip=FRACTION,
        pressureDependency=OFF, shearStressLimit=None, slipRateDependency=OFF,
        table=((k, ), ), temperatureDependency=OFF)
mdb.models['Model-1'].ContactProperty('Frictionless')
mdb.models['Model-1'].interactionProperties['Frictionless'].TangentialBehavior(
        formulation=FRICTIONLESS)
mdb.models['Model-1'].SurfaceToSurfaceContactStd(adjustMethod=NONE,
        clearanceRegion=None, createStepName='Initial', datumAxis=None,
        initialClearance=OMIT, interactionProperty='Friction', master=
        mdb.models['Model-1'].rootAssembly.instances['Stamp-1'].surfaces['Stamp surface']
        , name='Int-1', slave=
        mdb.models['Model-1'].rootAssembly.instances['Film-1'].surfaces['Top surface']
        , contactTracking=ONE_CONFIG, sliding=FINITE, thickness=ON)

# Boundary conditions
mdb.models['Model-1'].TabularAmplitude(data=((0.0, 0.0), (t/2, 1.0), (t, 0.0)),
        name='Amp-1', smooth=SOLVER_DEFAULT, timeSpan=STEP)
mdb.models['Model-1'].EncastreBC(createStepName='Initial', localCsys=None,
        name='BC-1', region=
        mdb.models['Model-1'].rootAssembly.instances['Film-1'].sets['Bottom edge'])
mdb.models['Model-1'].XsymmBC(createStepName='Initial', localCsys=None, name=
        'BC-2', region=
        mdb.models['Model-1'].rootAssembly.instances['Film-1'].sets['Right edge'])
mdb.models['Model-1'].DisplacementBC(amplitude=UNSET, createStepName=
        'Initial', distributionType=UNIFORM, fieldName='', localCsys=None, name=
        'BC-3', region=
        mdb.models['Model-1'].rootAssembly.instances['Film-1'].sets['Left edge'],
        u1=SET, u2=UNSET, ur3=UNSET)
mdb.models['Model-1'].rootAssembly.Set(name='Set-Stamp', referencePoints=(
        mdb.models['Model-1'].rootAssembly.instances['Stamp-1'].referencePoints[2],
        ))
mdb.models['Model-1'].DisplacementBC(amplitude=UNSET, createStepName=
        'Initial', distributionType=UNIFORM, fieldName='', localCsys=None, name=
        'BC-4', region=mdb.models['Model-1'].rootAssembly.sets['Set-Stamp'], u1=
        SET, u2=UNSET, ur3=SET)
mdb.models['Model-1'].boundaryConditions['BC-4'].setValuesInStep(amplitude=
```

```
        'Amp-1', stepName='Apply pressure', u2=-0.04)

# Field & history output requests
mdb.models['Model-1'].FieldOutputRequest(createStepName='Apply pressure', name=
        'F-Output-2', variables=('S', 'E', 'U', 'RF'))
mdb.models['Model-1'].FieldOutputRequest(createStepName='Apply pressure', name=
        'F-Output-3', variables=('MISESMAX', 'PS', 'E',
        'PE', 'PEEQ', 'PEEQT', 'EE', 'IE', 'LE', 'ER'))

# Job
mdb.Job(atTime=None, contactPrint=OFF, description='', echoPrint=OFF,
        explicitPrecision=SINGLE, getMemoryFromAnalysis=True, historyPrint=OFF,
        memory=90, memoryUnits=PERCENTAGE, model='Model-1', modelPrint=OFF,
        multiprocessingMode=DEFAULT, name='he_pn_105c',
        nodalOutputPrecision=SINGLE, numCpus=2, numDomains=2, numGPUs=0, queue=None,
        resultsFormat=ODB, scratch='', type=ANALYSIS, userSubroutine='', waitHours=
        0, waitMinutes=0)
mdb.jobs['he_pn_105c'].submit(consistencyChecking=OFF)
mdb.jobs['he_pn_105c'].waitForCompletion()
```

5.4 Results and Discussions

5.4.1 Generalised Maxwell Model

Figures 5.3, 5.4, 5.5, 5.6, 5.7 and 5.8 show results from the five isothermal simulations of R2R hot embossing of 1-mm-wide line feature using the generalised Maxwell viscoelastic model. Each figure displays the contour plots of von Mises stresses in the PMMA film during R2R hot embossing and after the embossing force was unloaded. One concern about the findings in these simulations was that the PMMA layer recovered after the embossing force was unloaded. Because of this limitation, the viscoelastic model may not be able to simulate the de-embossing process.

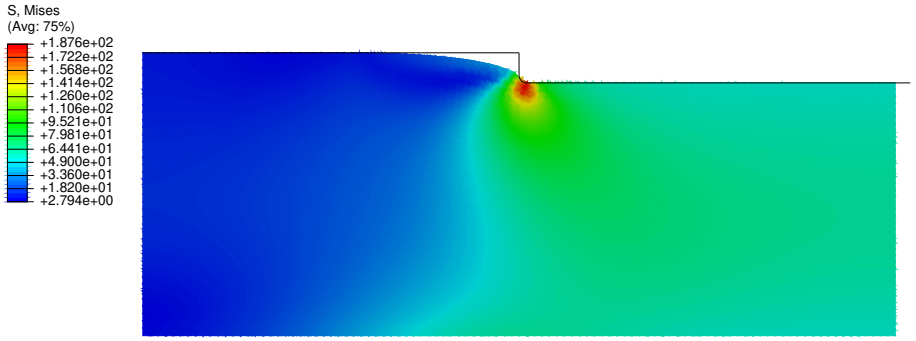

(a) During R2R hot embossing.

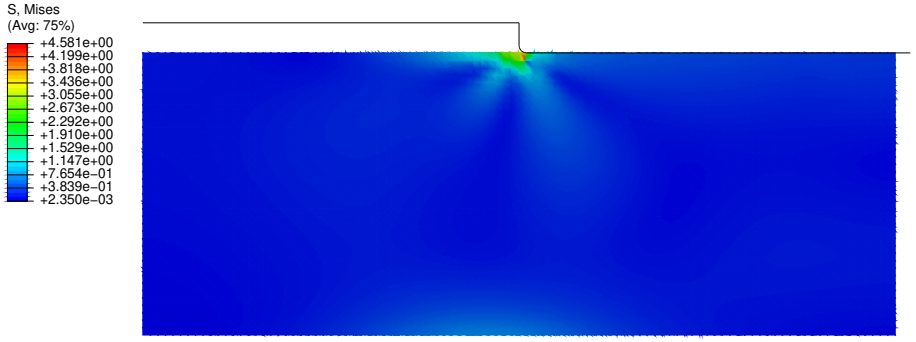

(b) After the embossing force was unloaded.

FIGURE 5.3: Numerical results of 1 mm line feature at 105 °C for the generalised Maxwell model.

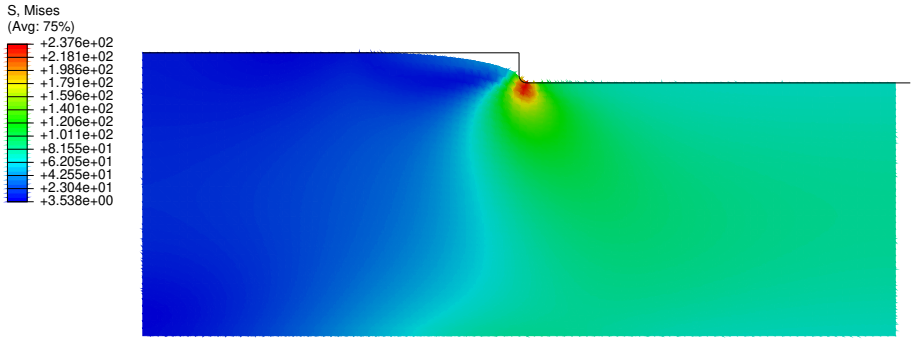

(a) During R2R hot embossing.

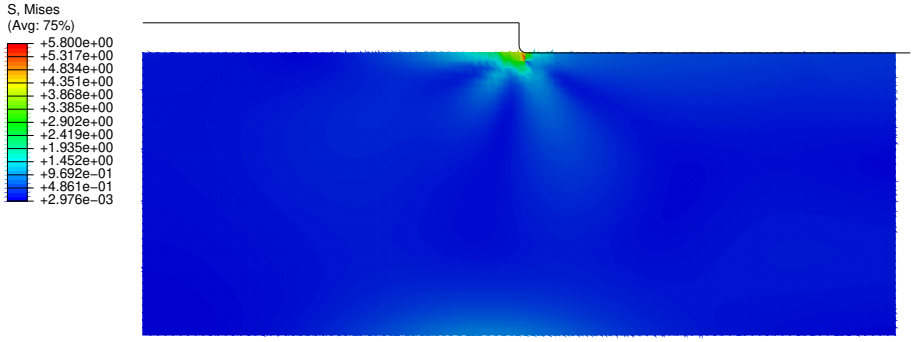

(b) After the embossing force was unloaded.

FIGURE 5.4: Numerical results of 1 mm line feature at 106 °C for the generalised Maxwell model.

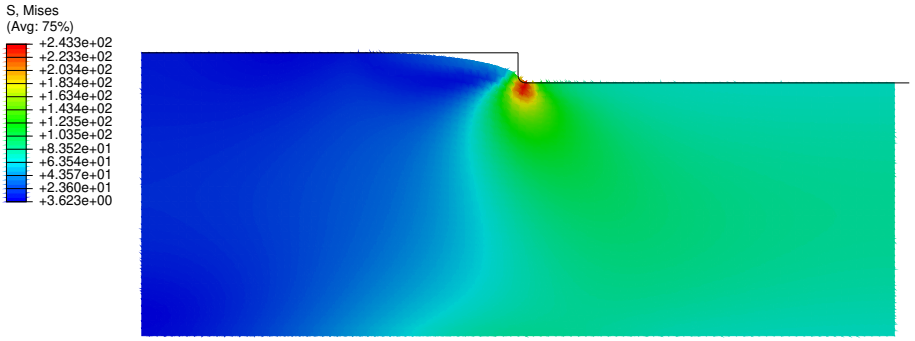

(a) During R2R hot embossing.

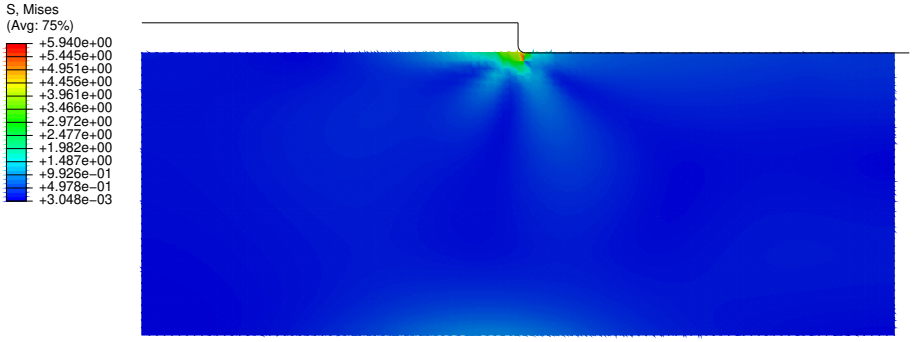

(b) After the embossing force was unloaded.

FIGURE 5.5: Numerical results of 1 mm line feature at 107 °C for the generalised Maxwell model.

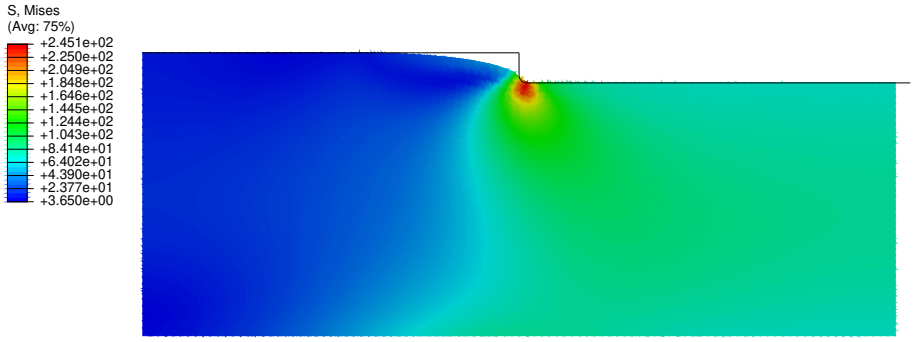

(a) During R2R hot embossing.

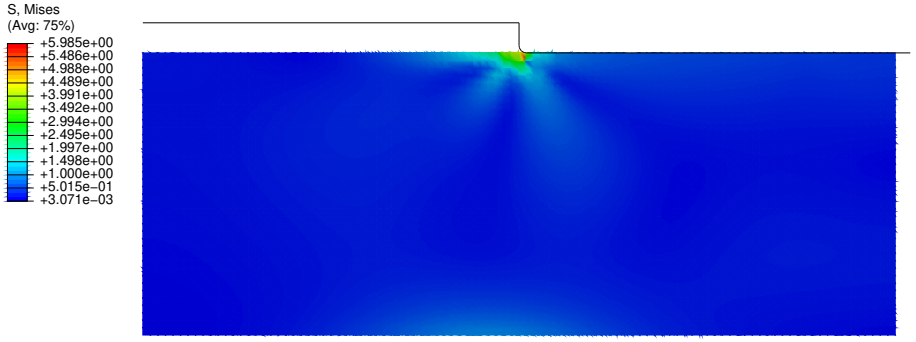

(b) After the embossing force was unloaded.

FIGURE 5.6: Numerical results of 1 mm line feature at 108 °C for the generalised Maxwell model.

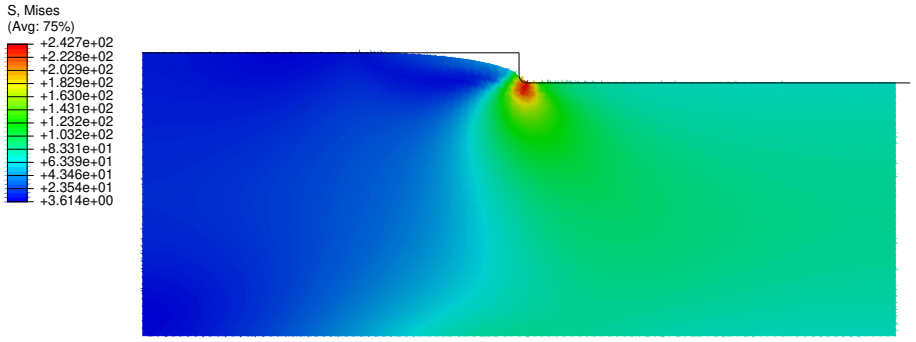

(a) During R2R hot embossing.

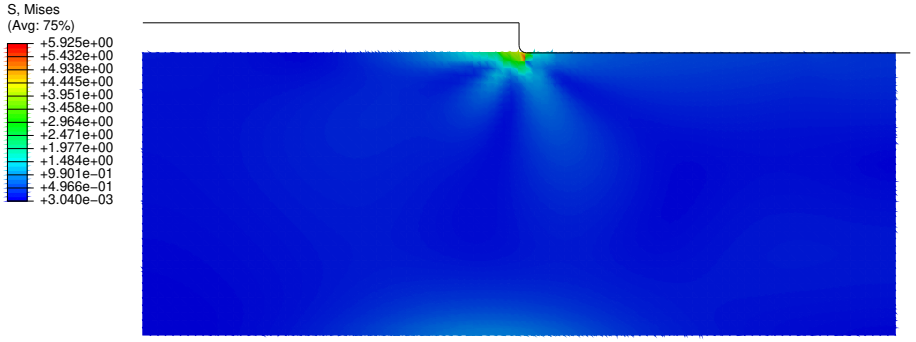

(b) After the embossing force was unloaded.

FIGURE 5.7: Numerical results of 1 mm line feature at 109 °C for the generalised Maxwell model.

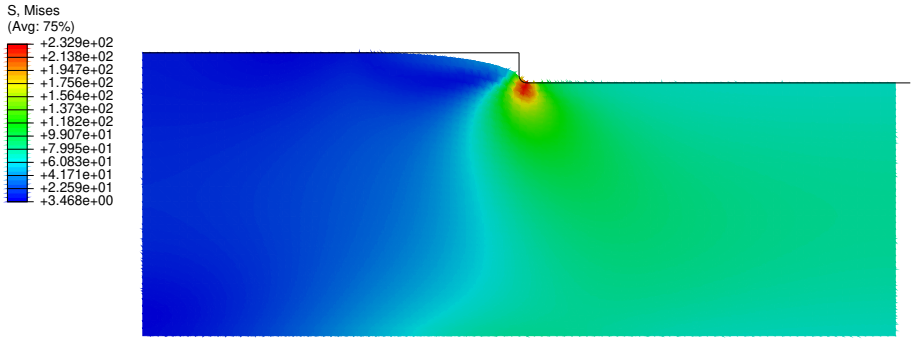

(a) During R2R hot embossing.

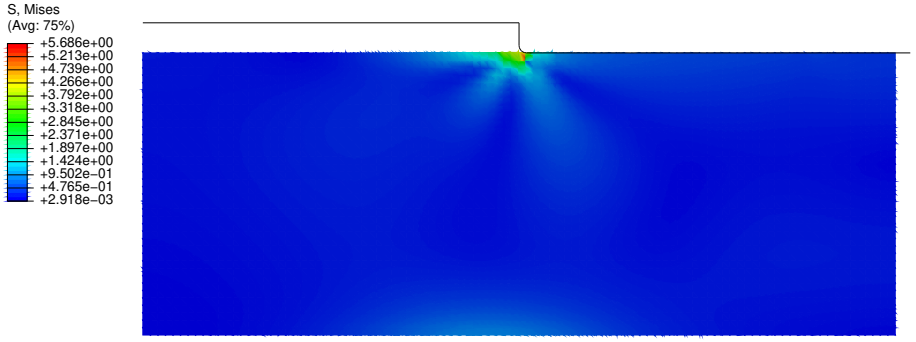

(b) After the embossing force was unloaded.

FIGURE 5.8: Numerical results of 1 mm line feature at 110 °C for the generalised Maxwell model.

5.4.2 Parallel Network Model

Figures 5.9, 5.10, 5.11, 5.12 and 5.13 display the contour plots of von Mises stress from the five isothermal simulations of R2R hot embossing of 1-mm-wide line feature using the parallel network model.

For the simulation at 90 °C, the filling stage was not complete when the PMMA film was moved away from the stamp. The highest stress occurred at the lower corner of the channel. After unloading the highest stress decreased from 53.336 to 32.560 MPa at the lower corner of the channel. The final deformed shape indicated that there was some recovery after the embossing force was released.

As we increased the temperature there were subtle changes in the deformation shape of the PMMA film. However, we observed that the residual stress in the lower corner of the embossed channel decreased with the increasing temperature.

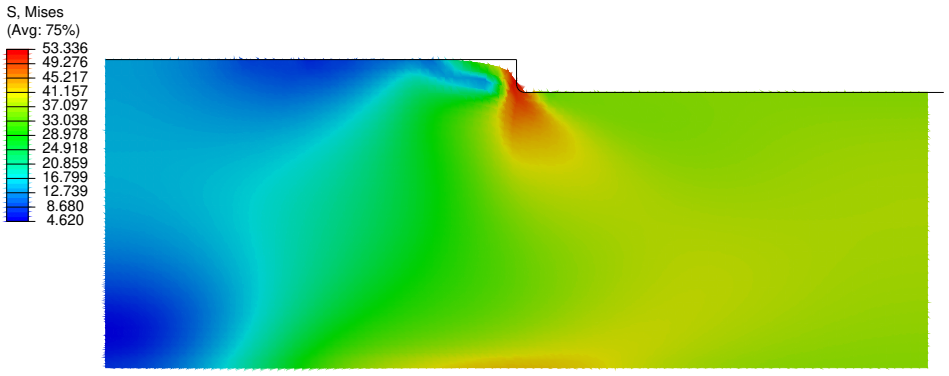

(a) During R2R hot embossing.

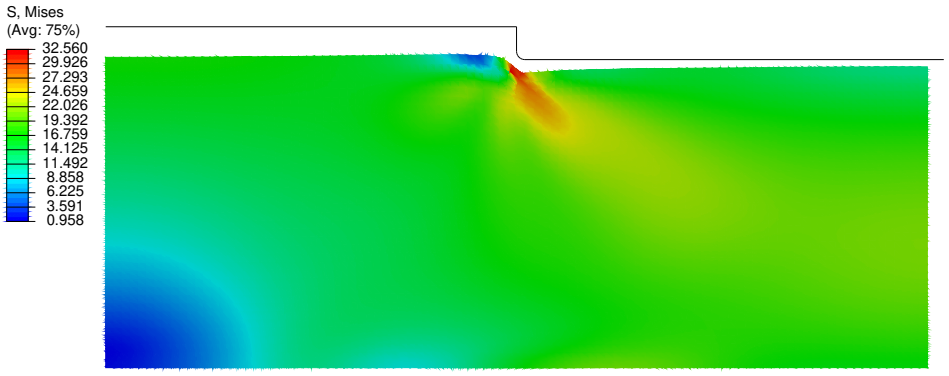

(b) After the embossing force was unloaded.

FIGURE 5.9: Numerical results of 1 mm line feature at 90 °C.

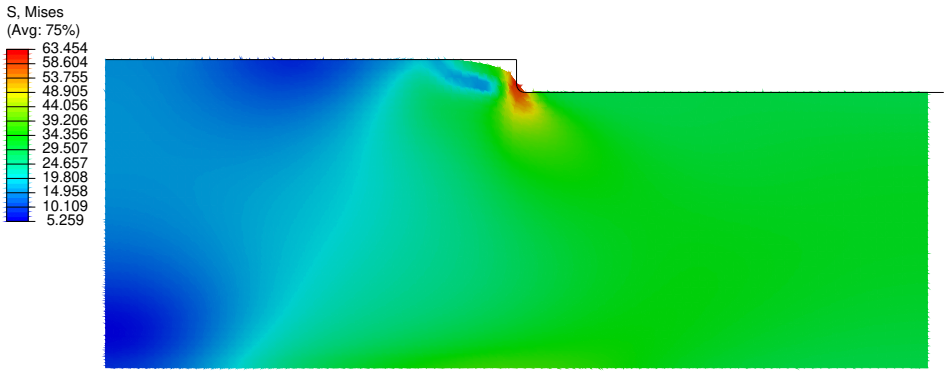

(a) During R2R hot embossing.

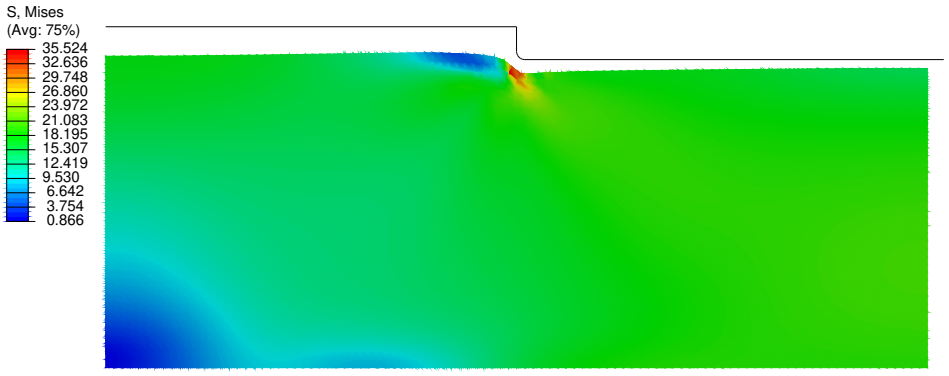

(b) After the embossing force was unloaded.

FIGURE 5.10: Numerical results of 1 mm line feature at 100 °C.

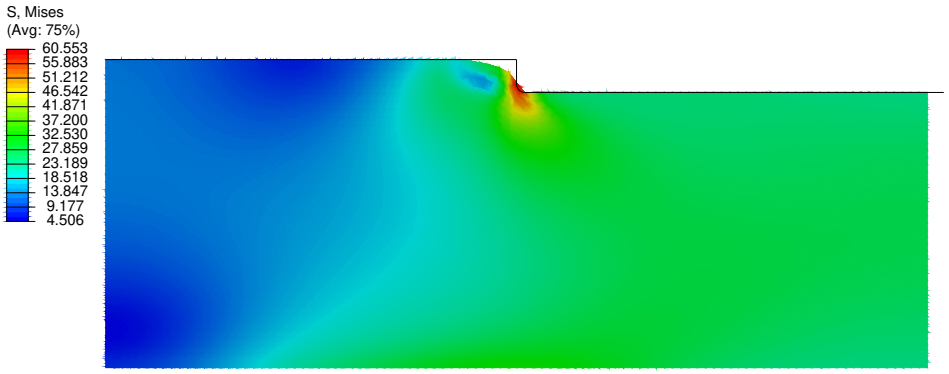

(a) During R2R hot embossing.

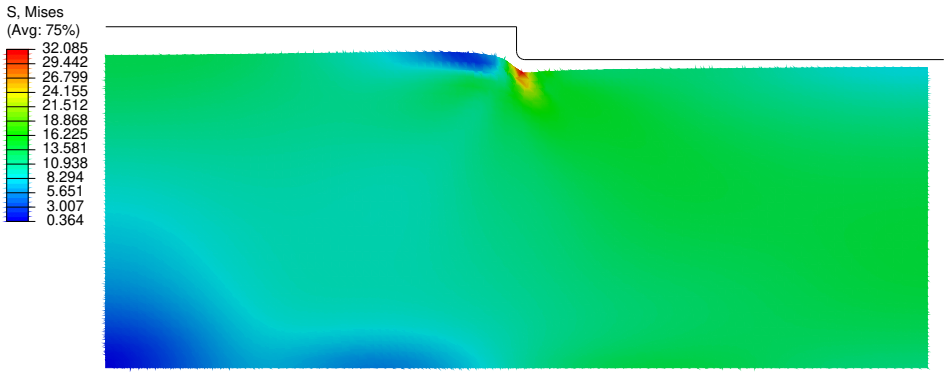

(b) After the embossing force was unloaded.

FIGURE 5.11: Numerical results of 1 mm line feature at 105 °C.

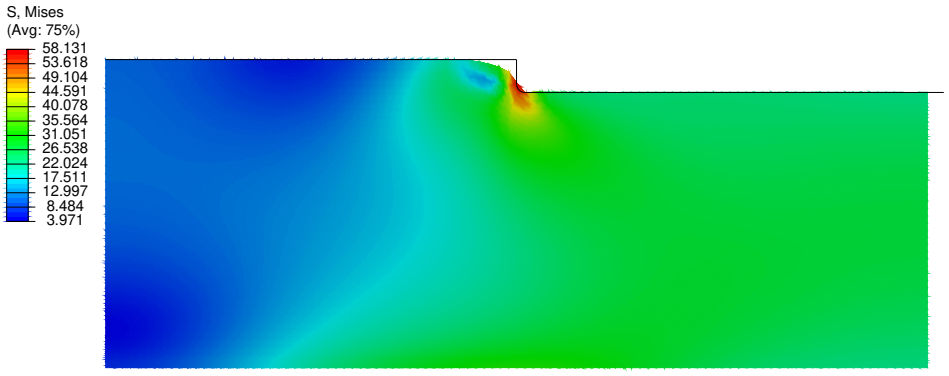

(a) During R2R hot embossing.

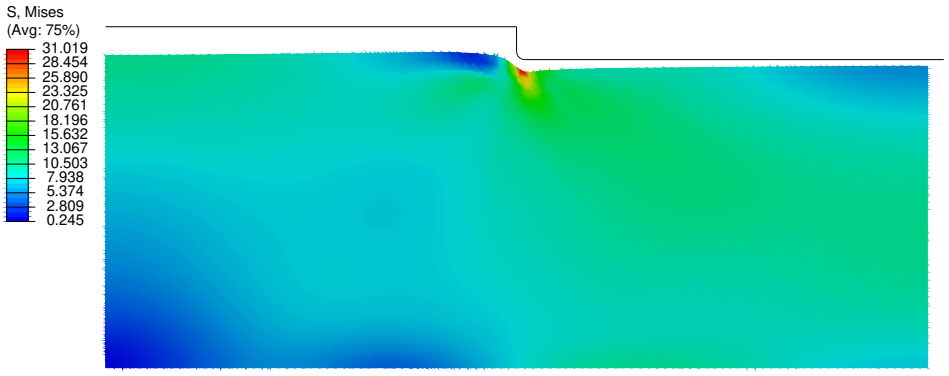

(b) After the embossing force was unloaded.

FIGURE 5.12: Numerical results of 1 mm line feature at 107 °C.

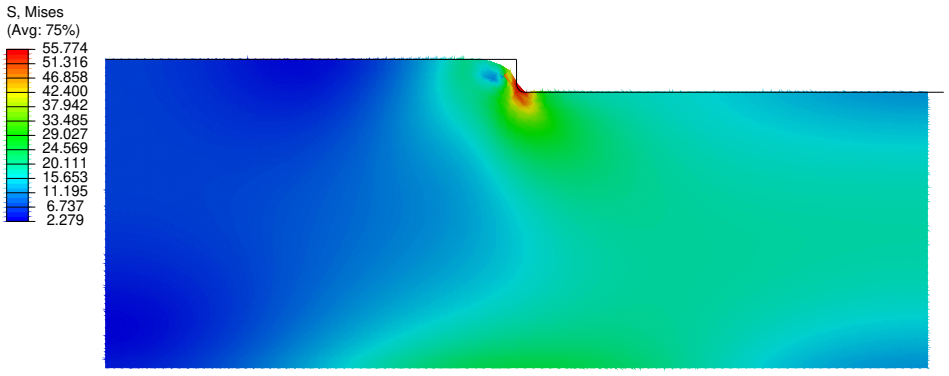

(a) During R2R hot embossing.

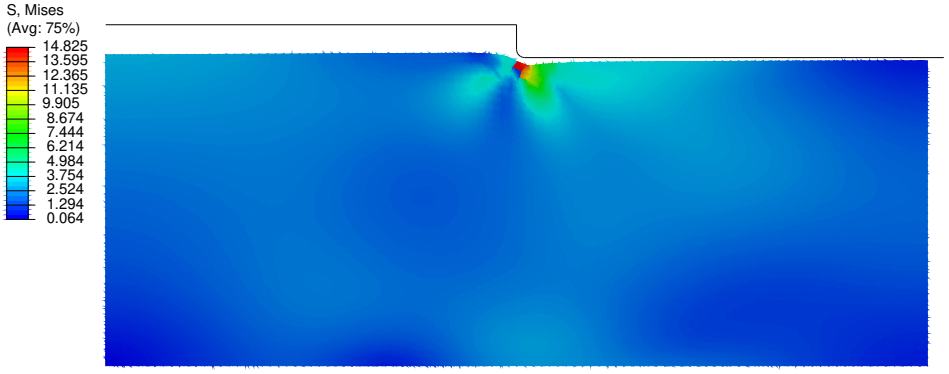

(b) After the embossing force was unloaded.

FIGURE 5.13: Numerical results of 1 mm line feature at 110 °C.

Figure 5.14 presents the deformed top surfaces of the PMMA film for frictionless contact and frictional contact with different friction coefficients (0.25, 0.5, 0.75). The results show very little differences between the 4 cases. For ease of investigation we fixed the friction coefficient to 0.75 for all other simulations.

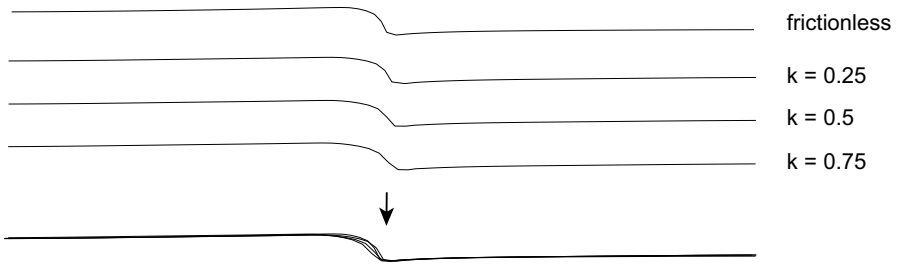

FIGURE 5.14: The deformed top surface of the PMMA at different friction coefficients (k).

For the case of 500-µm-wide lines, similar contour graphs were simulated, as displayed in Figure 5.15, 5.16, 5.17, 5.18 and 5.19. Furthermore, the contour plots for the 200-µm-wide line are presented in Figures 5.20, 5.21, 5.22, 5.23 and 5.24. Together, the present findings confirmed that the simulated channel depth reduced while the line width decreased from 1 mm to 500 µm and then 200 µm. The maximum channel depths were still lower than the stamp feature height of 40 µm.

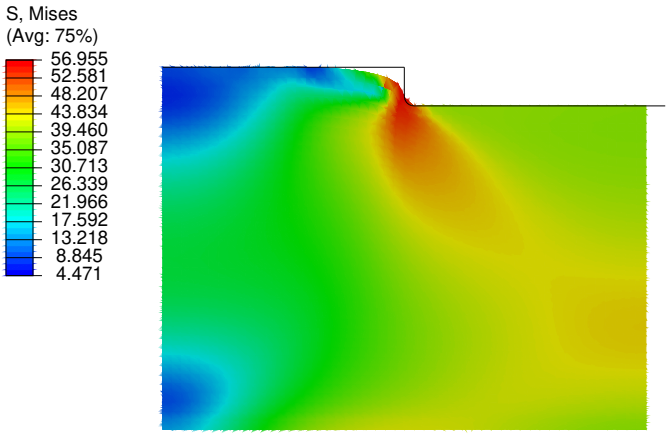

(a) During R2R hot embossing.

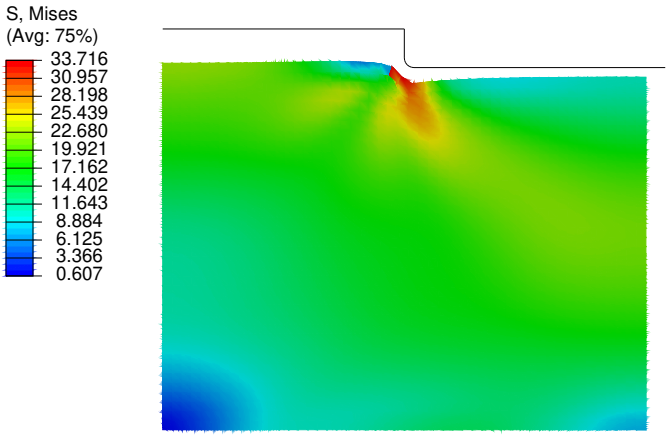

(b) After the embossing force was unloaded.

FIGURE 5.15: Numerical results of 500 µm line feature at 90 °C.

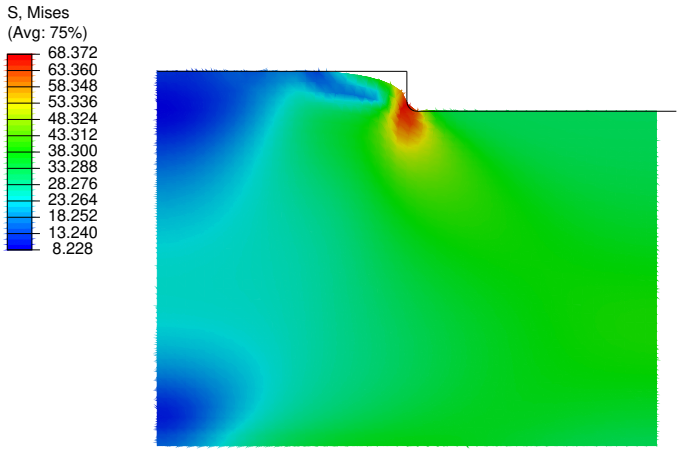

(a) During R2R hot embossing.

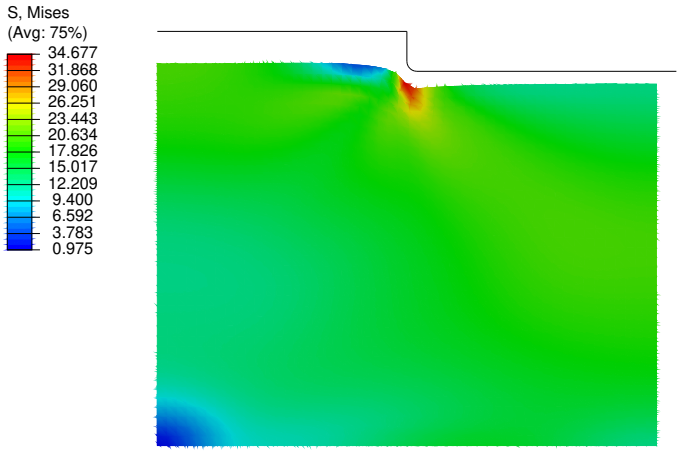

(b) After the embossing force was unloaded.

FIGURE 5.16: Numerical results of 500 µm line feature at 100 °C.

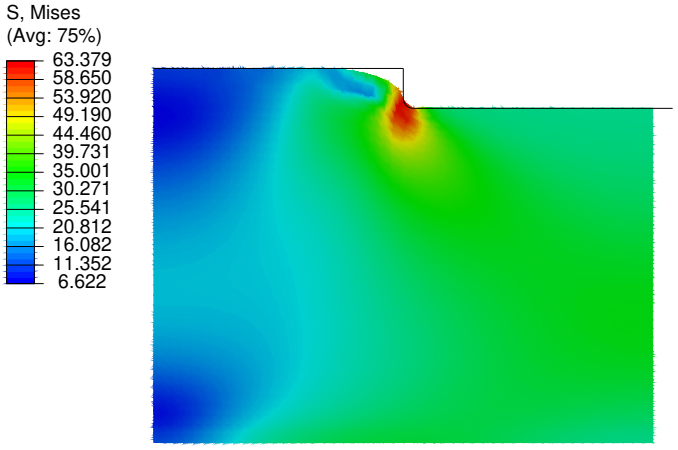

(a) During R2R hot embossing.

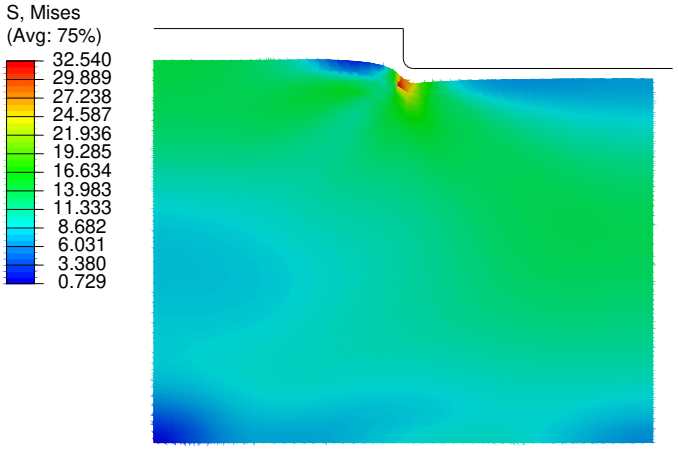

(b) After the embossing force was unloaded.

FIGURE 5.17: Numerical results of 500 µm line feature at 105 °C.

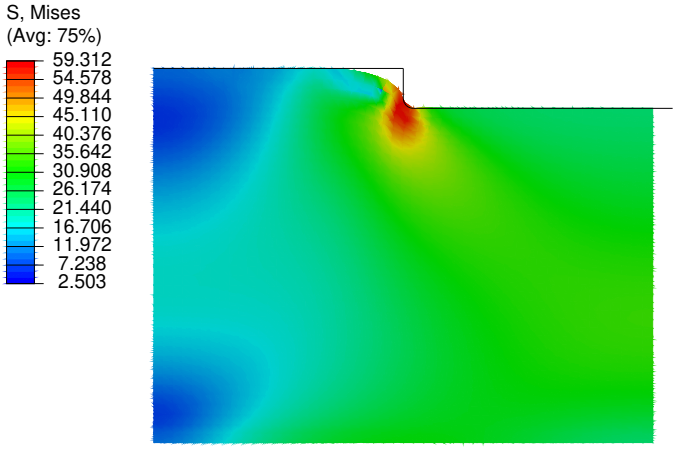

(a) During R2R hot embossing.

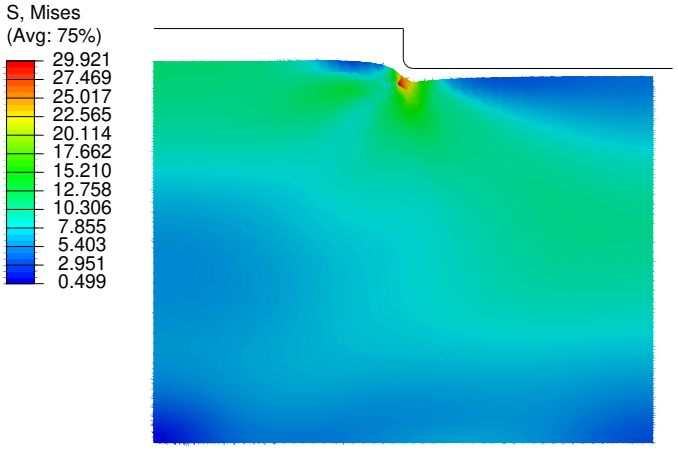

(b) After the embossing force was unloaded.

FIGURE 5.18: Numerical results of 500 µm line feature at 107 °C.

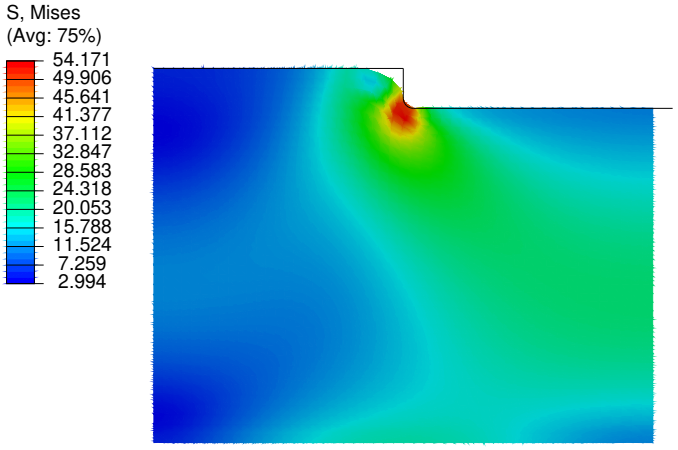

(a) During R2R hot embossing.

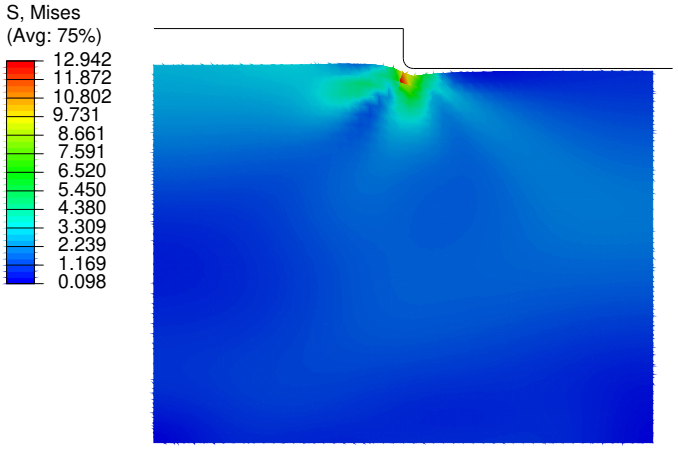

(b) After the embossing force was unloaded.

FIGURE 5.19: Numerical results of 500 µm line feature at 110 °C.

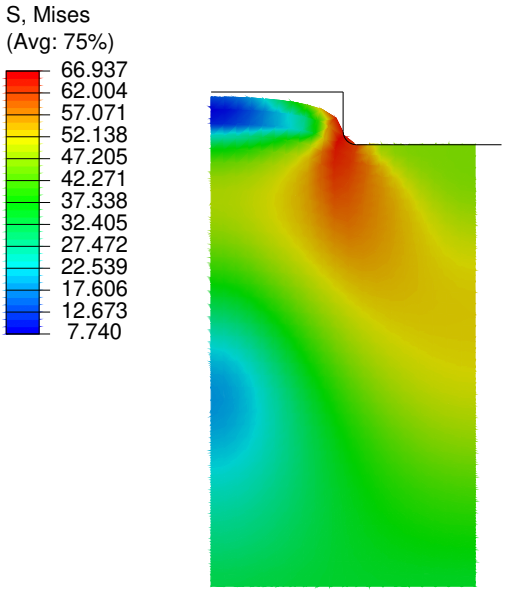

(a) During R2R hot embossing.

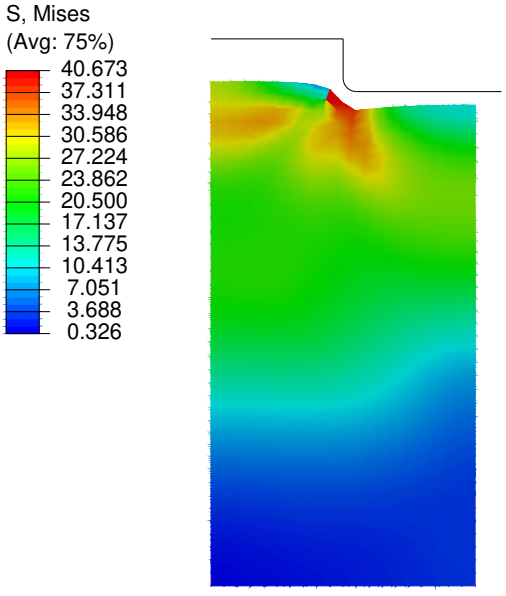

(b) After the embossing force was unloaded.

FIGURE 5.20: Numerical results of 200 µm line feature at 90 °C.

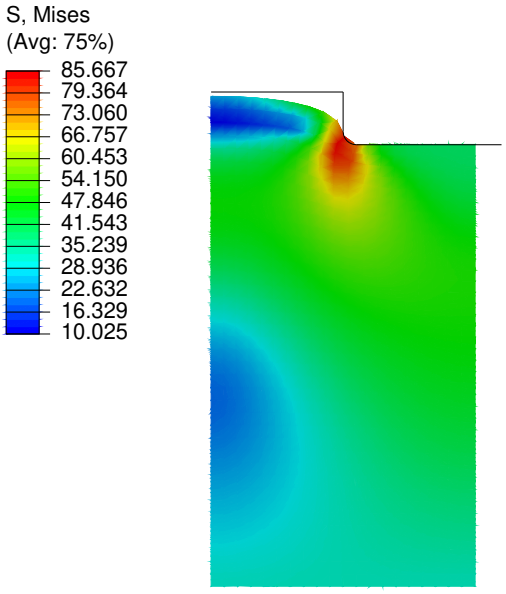

(a) During R2R hot embossing.

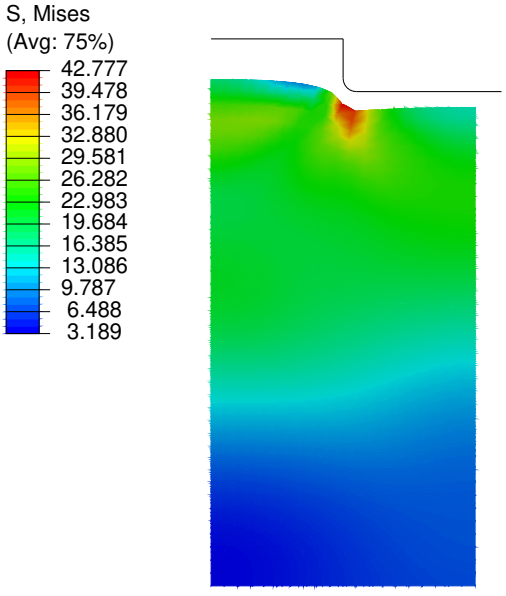

(b) After the embossing force was unloaded.

FIGURE 5.21: Numerical results of 200 µm line feature at 100 °C.

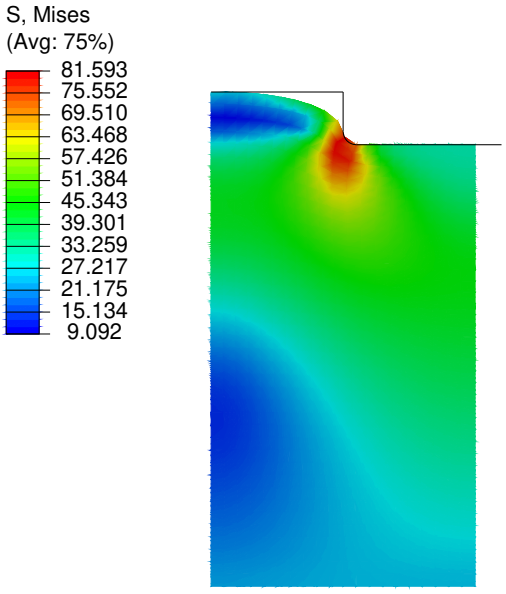

(a) During R2R hot embossing.

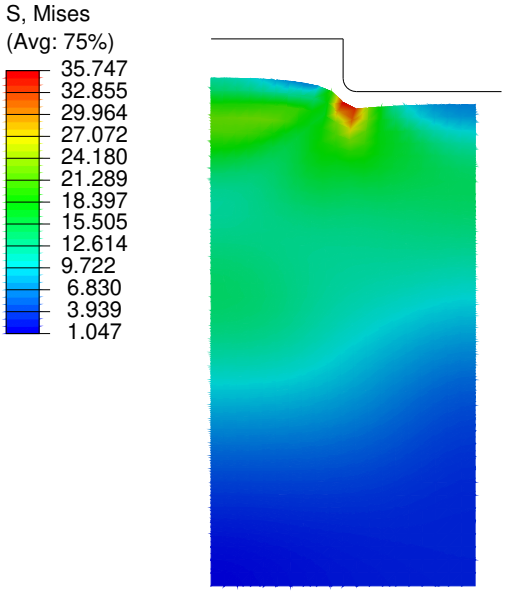

(b) After the embossing force was unloaded.

FIGURE 5.22: Numerical results of 200 µm line feature at 105 °C.

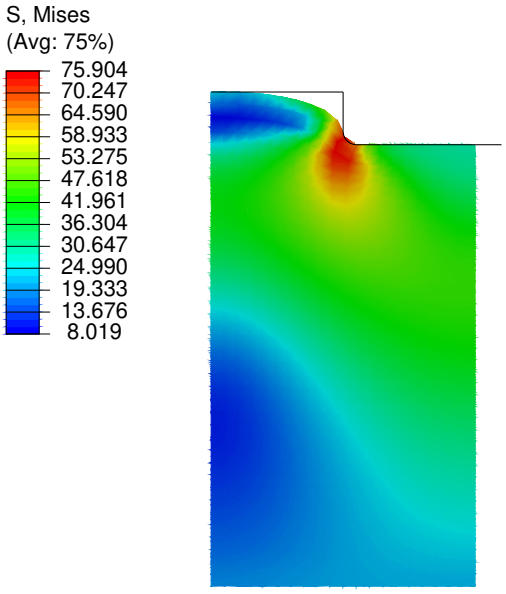

(a) During R2R hot embossing.

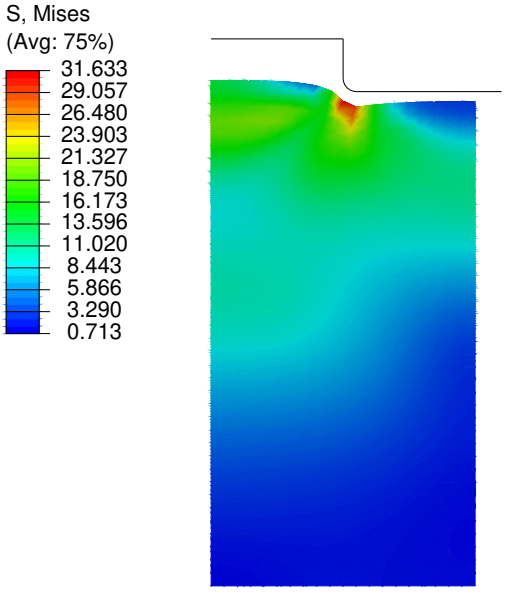

(b) After the embossing force was unloaded.

FIGURE 5.23: Numerical results of 200 µm line feature at 107 °C.

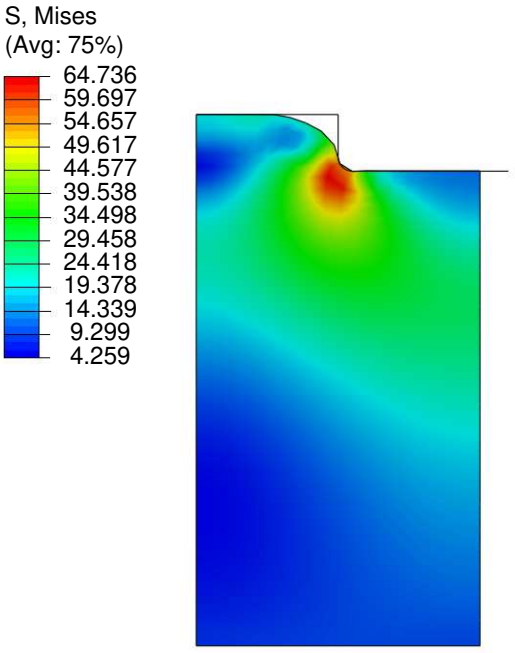

(a) During R2R hot embossing.

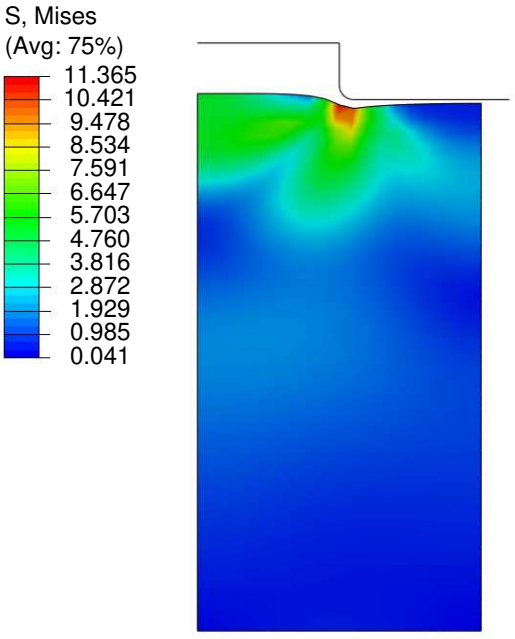

(b) After the embossing force was unloaded.

FIGURE 5.24: Numerical results of 200 µm line feature at 110 °C.

Figure 5.25 summarises the measured maximum channel depths from simulations and compares the results to the experimental results of 1-mm-wide line feature. The highest value for the maximum channel depth was 21.19 µm for the 200 µm line feature embossed at 100 °C. For all line designs the maximum channel depth increased from 90 to 100 °C and decreased from 100 to 110 °C. The discrepancy between the numerical and experimental results may be caused by too much recovery at temperatures from 100 to 110 °C. Nonetheless, the numerical results were close to the experimental value of 15 µm at 107 °C. At 110 °C all simulation results were lower than 10 µm.

Additionally, the maximum channel depth was influenced by the feature design. For the 50 µm line, all values were lower than other cases due to the narrow opening for PMMA to fill in. For the 1 mm line, the material filling process took longer than other cases, which lowered the filling ratio. In all cases the feature of 200 µm wide achieved the highest results.

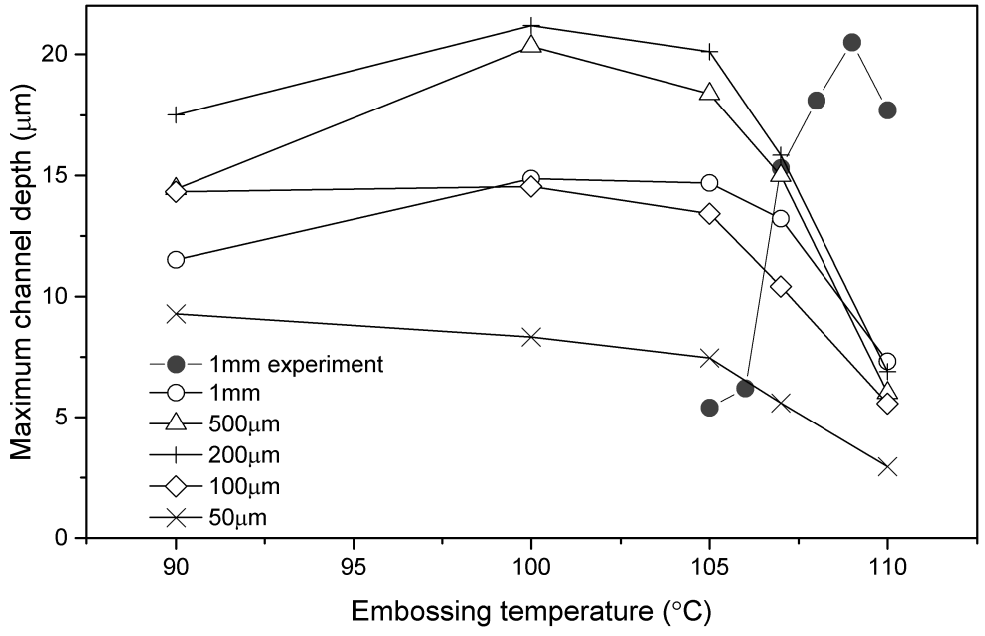

FIGURE 5.25: Maximum channel depth versus embossing temperature for different line features.

We further investigated the effects of rolling speed by changing the speed settings in the Python code. For the 1-mm-wide line, we changed the rolling speed from 1.0 m/min to

0.5 m/min and 1.5 m/min. For the rolling speed of 0.5 m/min, the deformed contour plots of von Mises stress at different temperatures are shown in Figures 5.26, 5.27, 5.28, 5.29 and 5.30. The peak channel depth was seen at 105 °C. However at the rolling speed of 1.5 m/min, the peak channel depth was at 100 °C, as presented in the contour plots displayed in Figures 5.31, 5.32, 5.33, 5.34 and 5.35. We compared the maximum channel depth at different embossing temperatures between the three rolling speeds in Figure 5.36. From these results, it is clear that the depth of embossed channels increased when the rolling speed decreased. Therefore, there should be a trade-off between rolling speed and embossing quality.

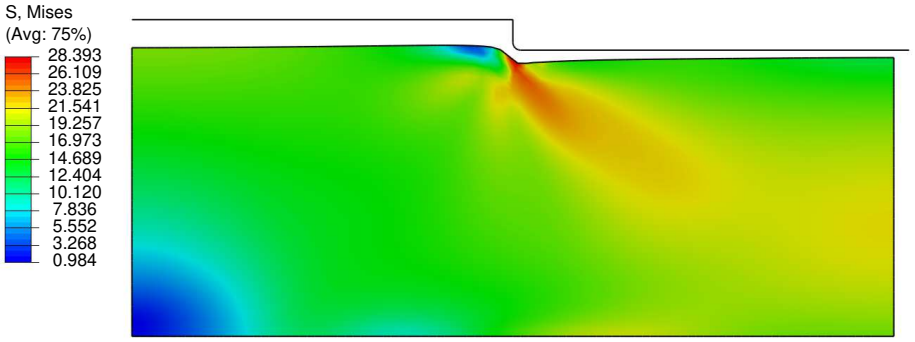

FIGURE 5.26: Numerical results of 1 mm line feature at 90 °C and rolling speed of 0.5 m/min.

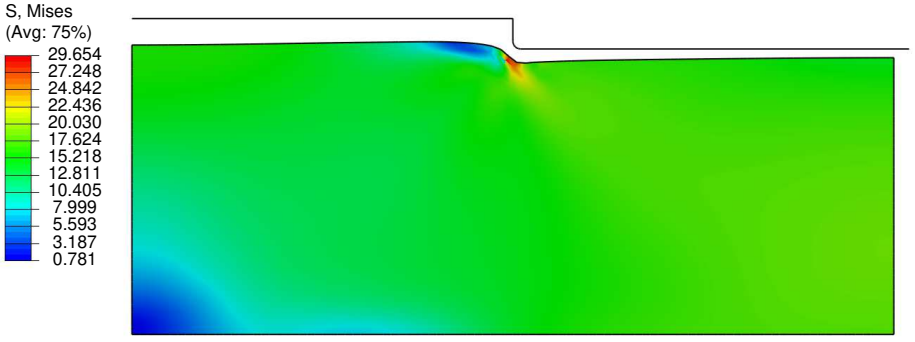

FIGURE 5.27: Numerical results of 1 mm line feature at 100 °C and rolling speed of 0.5 m/min.

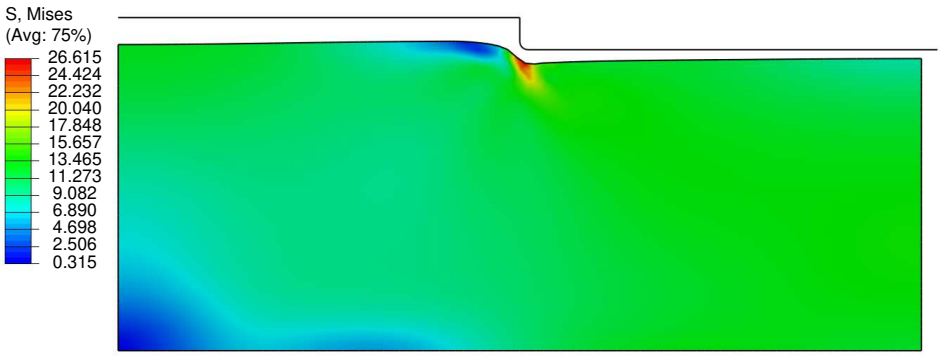

FIGURE 5.28: Numerical results of 1 mm line feature at 105 °C and rolling speed of 0.5 m/min.

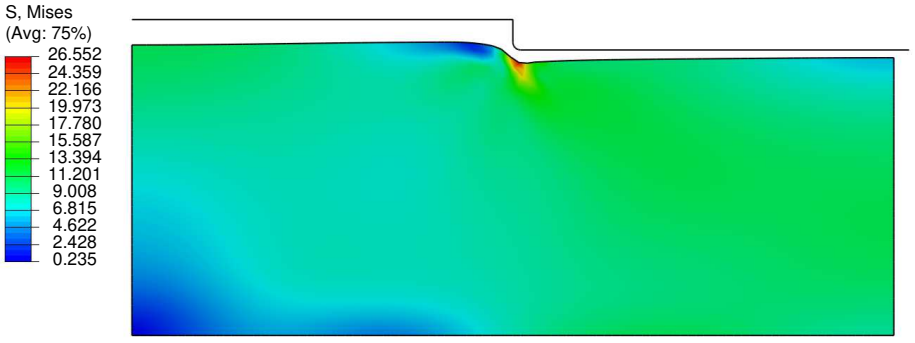

FIGURE 5.29: Numerical results of 1 mm line feature at 107 °C and rolling speed of 0.5 m/min.

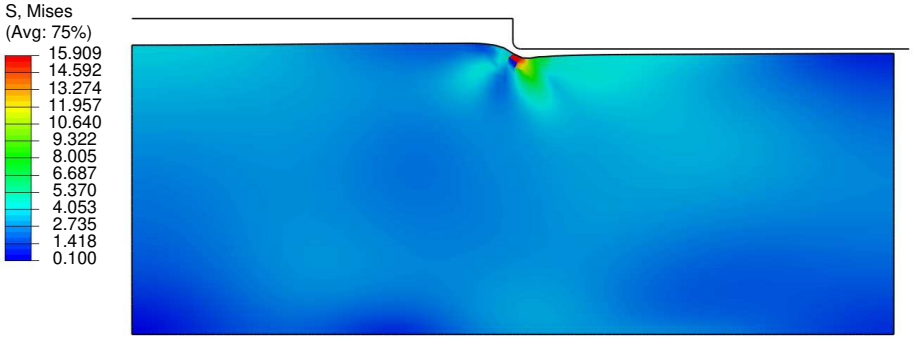

FIGURE 5.30: Numerical results of 1 mm line feature at 110 °C and rolling speed of 0.5 m/min.

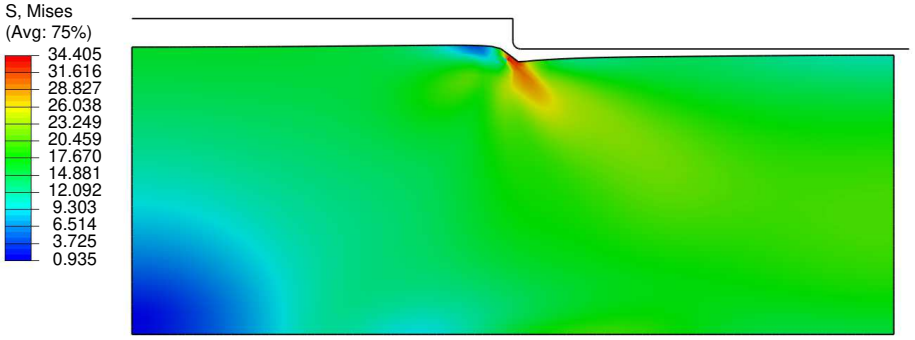

FIGURE 5.31: Numerical results of 1 mm line feature at 90 °C and rolling speed of 1.5 m/min.

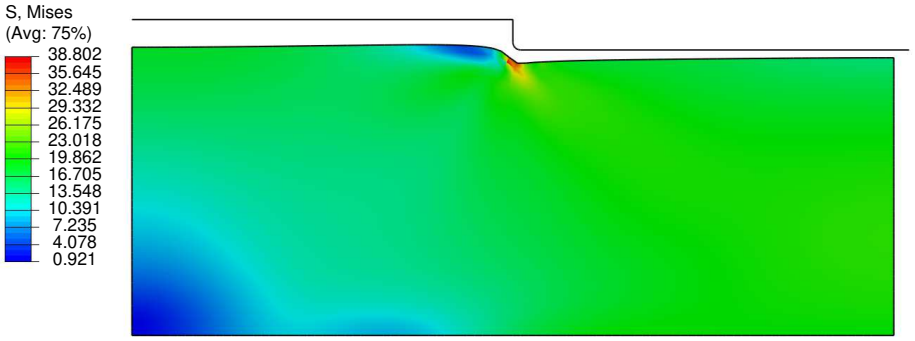

FIGURE 5.32: Numerical results of 1 mm line feature at 100 °C and rolling speed of 1.5 m/min.

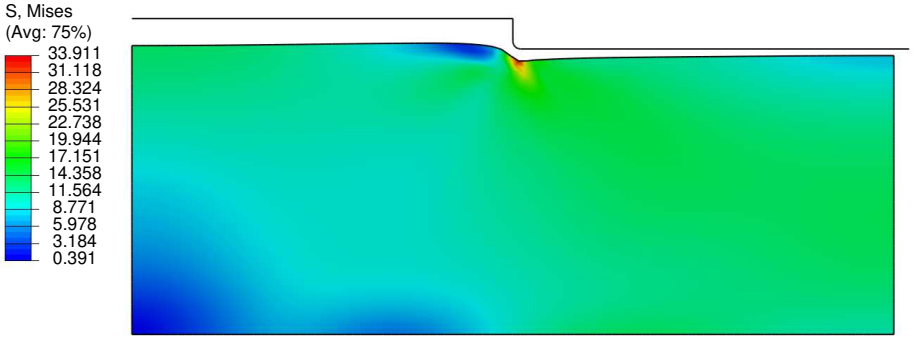

FIGURE 5.33: Numerical results of 1 mm line feature at 105 °C and rolling speed of 1.5 m/min.

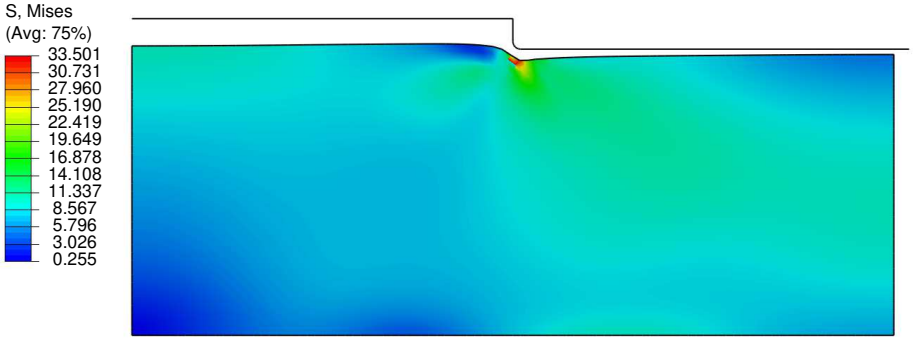

FIGURE 5.34: Numerical results of 1 mm line feature at 107 °C and rolling speed of 1.5 m/min.

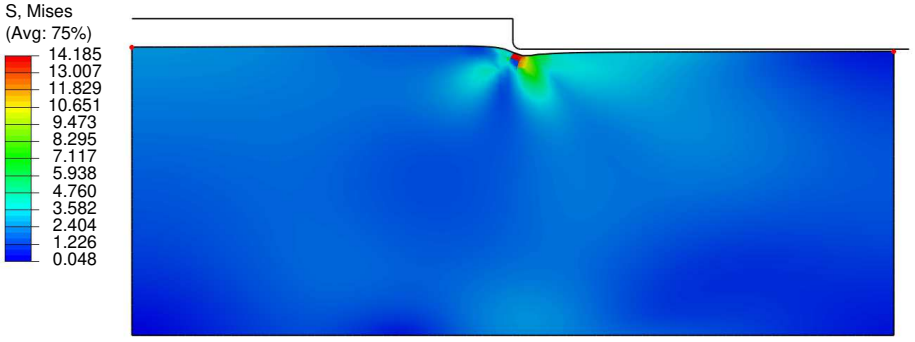

FIGURE 5.35: Numerical results of 1 mm line feature at 110 °C and rolling speed of 1.5 m/min.

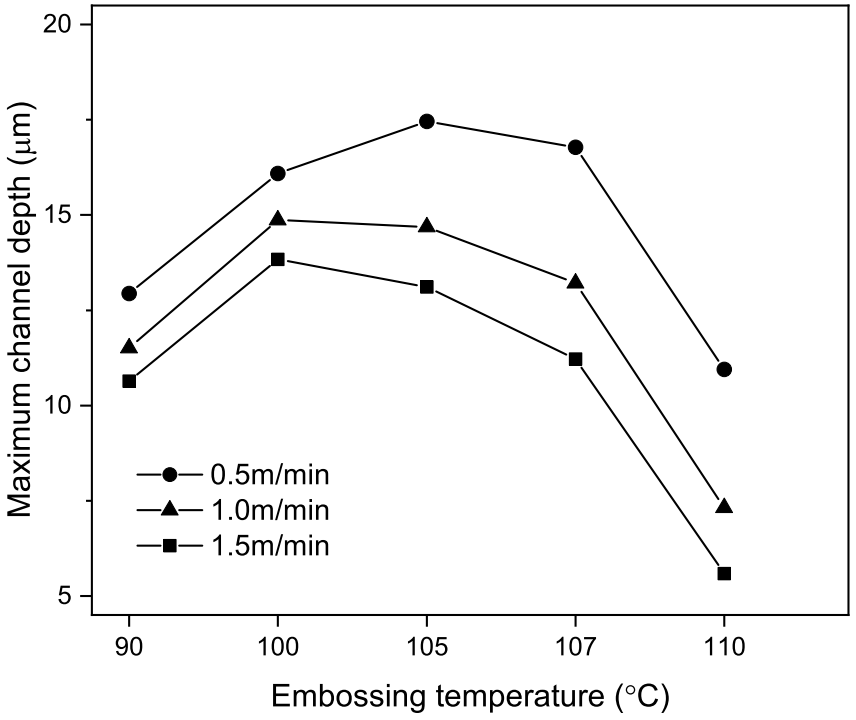

FIGURE 5.36: Maximum channel depth versus embossing temperature for different line features.

Next we made another simulation by changing the parameters of the Python script and compared the numerical results with the previous R2R embossing work conducted by Liedert *et al.* at VTT [76], who introduced the R2R hot embossing of a 125-µm-thick PMMA with a 150-µm-wide stamp (Figure 5.37.) The predicted profile of microfluidic channels were created by coping and reflecting the symmetric model, as illustrated by the red lines in Figure 5.37. The simulation results were very near to the SEM image however the predicted profiles especially the channel walls were slightly different. This is because the stamp geometries were idealised and these should be adjusted to the actual stamp shapes if we had more accurate profile data for the shim.

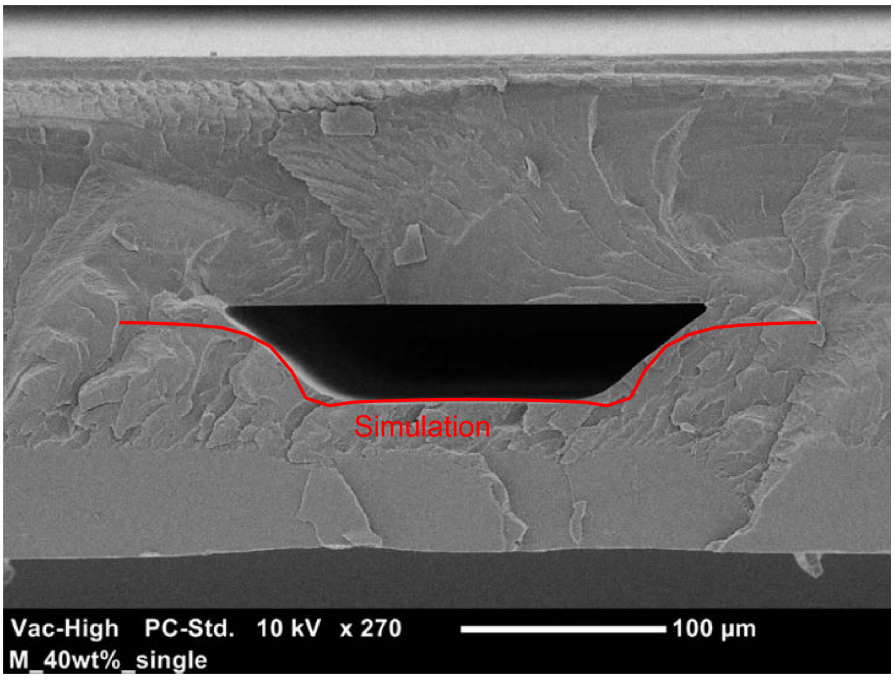

FIGURE 5.37: Comparison between an SEM image of the microfluidic channel by Liedert *et al.* [76] and numerical predictions.

The differences between numerical results and experimental results could be caused by insufficient heat transfer between the embossing roller and the polymer film. Moreover, the pressure was set to constant in the simulation however the nip pressure is changing at ±0.1 bar which is recorded by a nip pressure measurement system. Therefore, the model can be improved with the real pressure distribution being measured.

The Python script has been proved effective in generating simulations of different shim feature designs. Moreover, by changing the materials properties of each temperature,

the temperature effects have been investigated in the simulation. However, more work is needed to incorporate thermal expansion effects with the method used in our research.

5.5 Conclusions

The preliminary simulation results have shown the possibility of converting an existing constitutive theory of the polymer material into the simple numerical problems. The geometries of the model were defined automatically by a Python script and this can be used for different generic geometries and different embossing temperatures, therefore can be useful to the parameter optimisation process for the R2R hot embossing. It is anticipated that the simulation methods can be used on other thermoplastic materials which are widely processed with R2R hot embossing, including cyclic olefin copolymer (COC) and polycarbonate (PC), for they have similar thermo-mechanical properties.

However, there are some limitations in our work. During tensile tests it is difficult to keep a constant temperature for each test, which would affect the calibration of PMMA's thermo-mechanical properties at each testing temperature. This calibration method is suited to only a limited range of temperatures near PMMA's T_g. For a wider temperature range above PMMA's T_g, a more versatile constitutive model is required.

The simulation is a plane-strain case therefore only the cross-section of the embossed channel is displayed. The method can be used for simple geometries, however for more complex channel layouts such as a 3D case should be considered.

Chapter 6

Conclusions and Recommendations

6.1 Conclusions

This thesis presents a study of the thermo-mechanical behaviour of PMMA in R2R hot embossing of microfluidic channels, including a literature review of microfluidic device fabrication techniques and constitutive theories, mechanical characterisations of PMMA such as tensile tests and DMA, experimental results of R2R hot embossing trials, and finite element simulations of R2R hot embossing. The tensile test and DMA results have been calibrated to be used in the finite element simulations of R2R hot embossing. These simulations results have been validated through comparisons with experimental results.

The purpose of this thesis has been to enhance the understanding of R2R hot embossing of PMMA-based microfluidic channels. While no systematic research has been conducted on how to guide the process parameter settings during R2R hot embossing, the work of this project can be used to: 1. assist the process engineer to optimise the process parameters; 2. help microfluidic chip designer modify their shim and microfluidic channel designs according to simulation results.

6.1.1 Findings from Mechanical Calibrations of PMMA

The material calibration methods include tensile tests and DMA, and the calibration test conditions have represented the actual conditions during R2R hot embossing trials, including temperatures and strain rates.

For DMA, the temperature sweep from 20 to 150 °C have shown significant changes in both storage modulus and loss modulus as PMMA enters the glass transition stage. In addition, the frequency sweep has shown strong frequency/rate dependence in the temperature range above T_g. For calibration PMMA is modelled as a generalised Maxwell viscoelastic material for the DMA data for temperatures ranging from 106 to 112 °C.

The tensile tests have covered the temperature range from 90 to 120 °C and strain rates of 0.001, 0.01 and 0.1/s. The test results have demonstrated strong temperature- and rate-dependence when PMMA is in the glass transition stage. The yield peak decreases and then disappears at temperature above T_g, and the strain recovery rate increases with temperature. We have shown that the tensile test data is consistent with what has been found in previous compressive tests. The tensile test data has been fitted to a parallel network model with viscoplastic components for the temperatures ranging from 90 to 110 °C. The fitted data has been validated through comparison with finite element simulations of tensile tests at the same test conditions.

6.1.2 Findings from R2R Hot Embossing Trials

An experimental method has been developed to explore how the process parameters affect the R2R hot embossing of the PMMA film. We have conducted experimental trials of R2R hot embossing using our custom-designed generic shims with two feature reliefs (40 and 80 µm). Unfortunately, the average relief height was measured as 103 µm approximately the for 80 µm design. We have found defects associated with different shim layouts, consisting of V-shaped and coin-shaped patterns. The defects include reduced etching height and shape distortion. Nevertheless, good results have been obtained for the straight line features on the shim with a designed relief height of 40 µm. The height

variation is within 5% in the direction normal to the rolling direction and 10% in the direction parallel to the rolling direction.

R2R hot embossing trials have been conducted at every degree from 105 to 110 °C to evaluate the effects of temperature on the profiles of embossed microfluidic channels. For the set of 6 straight lines with different widths, the embossed profile of 1-mm-wide line is closest to the design profile, however the overall results are different from planar hot embossing, in which the transfer rate can reach 100%. The highest transfer rate achieved is 51.3% at 109 °C.

6.1.3 Findings from FE Simulations

The simulation approach described in this thesis has been used to predict the cross-sectional shape of microfluidic channels after R2R hot embossing. This method can be adjusted for the different conditions, and this conditions includes temperature, nip pressure and rolling speed. Moreover, we have written a Python script to automatically draw the geometries of PMMA film and embossing shim, and define the material properties, web moving speed and nip pressure. The Python script has been proved to be efficient in simulating different R2R hot embossing processes by changing the process parameters.

The FE simulation results have shown reasonable accuracy in predicting the outputs of R2R hot embossing for the 1-mm-wide line feature embossed from 105 to 110 °C.

6.2 Future Work

In this thesis certain points have been simplified or neglected as this is a preliminary research on the R2R hot embossing and there are some limitations in terms of experimental and numerical environments. To improve the current work, several recommendation points for the future work are give below.

6.2.1 Improved Characterisation Methods for PMMA

The 1 °C to 1 °C temperature control in DMA needs to be more precise, as we have observed that there is less than 0.2 °C of temperature variations in each 'isothermal' step.

In tensile tests the engineering strain was captured by the video extensometer, however the tensometer controls the largest testing strain by the strain measured by the extension of the grip. This is the reason for the difference in the largest testing strain in different tests. A closed-loop control system may be implemented to ensure that true strain reaches 100% for each test.

It is not possible to conduct compressive tests on the PMMA films provided in this project. As compression is a process more close to hot embossing than tension, it is worth doing compressive tests on the same material.

The material parameters in the theory need to be calibrated for other thermoplastic materials which are widely used in R2R hot embossing, such as cyclic olefin copolymer (COC), cyclic olefin polymer (COP), polypropylene (PP), polystyrene (PS) and polycarbonate (PC).

6.2.2 Improved Generic Shim Designs

As this is a one-time R2R hot embossing trial experiment, there is no chance to modify the design of the generic shim in this project. If possible in the future, the design of the generic shim can be improved in the following aspects: First, the aspect ratios of designed features should be lowered due to the limitation of shim fabrication and R2R hot embossing. Second, to avoid the interference of features too close to each other, the pattern density should not be too high. Third, it is worth putting in some designs from specific microfluidic applications.

6.2.3 Non-isothermal Simulations

By far all FE simulations were conducted for isothermal conditions. Future work needs to be done to cover the entire R2R hot embossing, by adding the the process when microfluidic channels are cooled to the room temperature. This requires another constitutive material model covering the temperature range from T_g to room temperature. In addition, future research could consider the potential effects of thermal expansions.

6.2.4 Modelling the Bonding Process

Solvent bonding has been used to seal the PMMA-based microfluidic channels with the same PMMA film [76]. It is required that the amount of distortion in the embossed patterns should be kept at minimum in the bonding process, therefore a bonding simulation to identify these distortions is needed.

The simulation of bonding is similar to the modelling of planar hot embossing. The starting point will be a two-dimensional symmetric model consisting of one PMMA layer of simple feature (such as a line feature) and another PMMA layer. Essential parameters in the numerical model include bonding pressure, temperature and hold time. Pattern deformations should be modelled considering two important phenomena: First two PMMA layers are pressing into each other by the bonding pressure, second the PMMA film will deform due to its viscoelastic response near T_g.

Appendix A

Surface Data

A.1 Generic Shim Layout

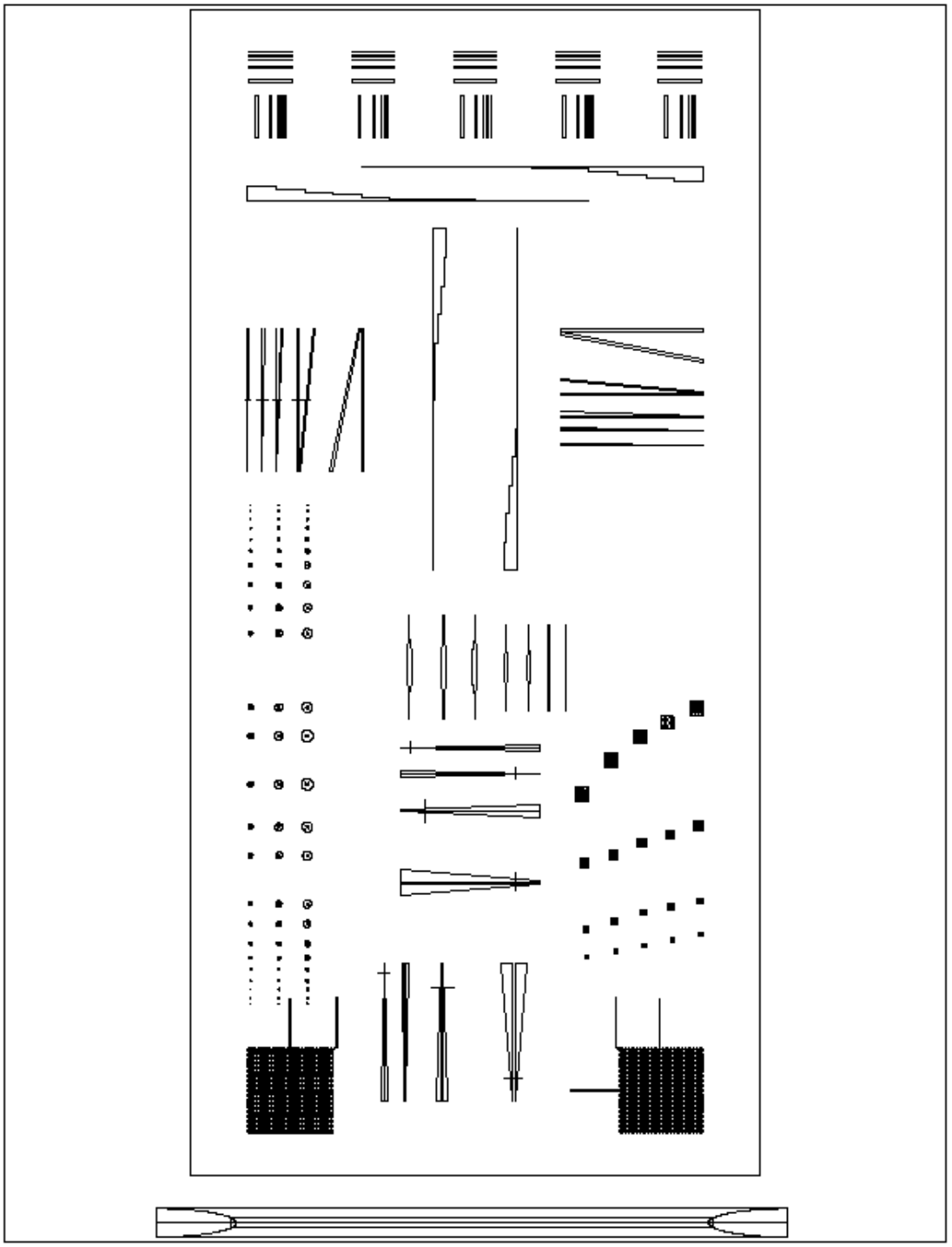

FIGURE A.1: Layout of features on the generic shims.

A.2 Surface Profiles of Features on the Shim

Feature AX1 refers to the Type A feature Number 1 in the x-direction, AY1 refers to the Type A feature Number 1 in the y-direction, et cetera.

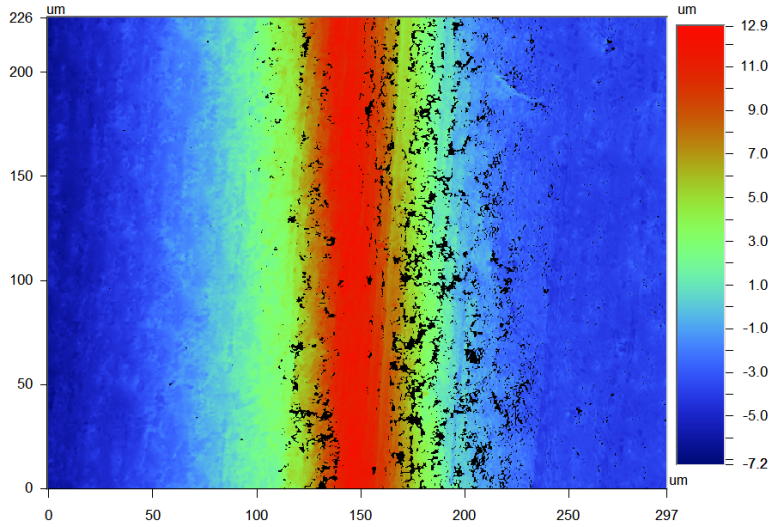

FIGURE A.2: Contour plot showing the surface profile of line feature AX1.

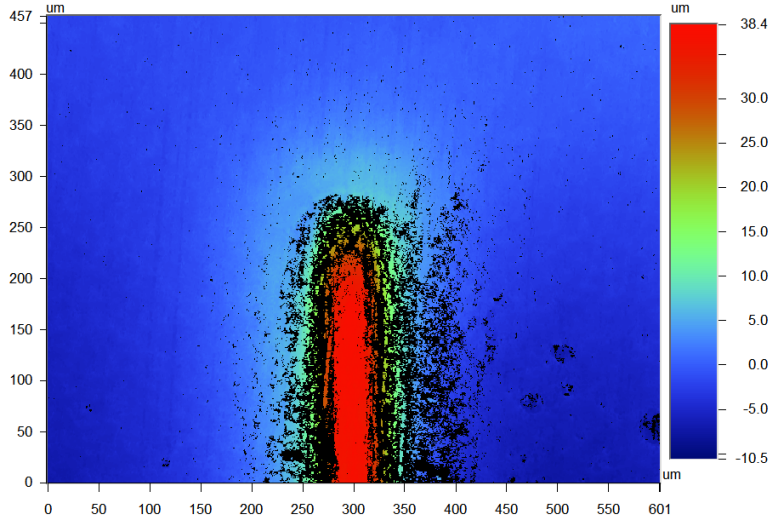

FIGURE A.3: Contour plot showing the surface profile of line feature AX2.

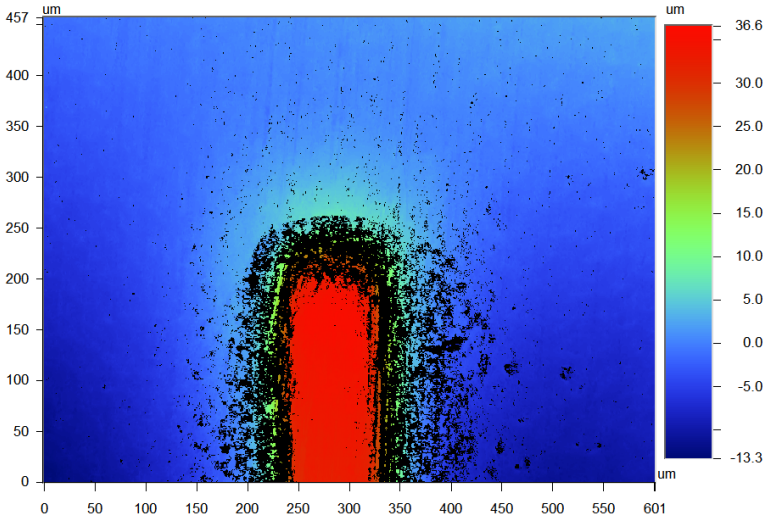

FIGURE A.4: Contour plot showing the surface profile of line feature AX3.

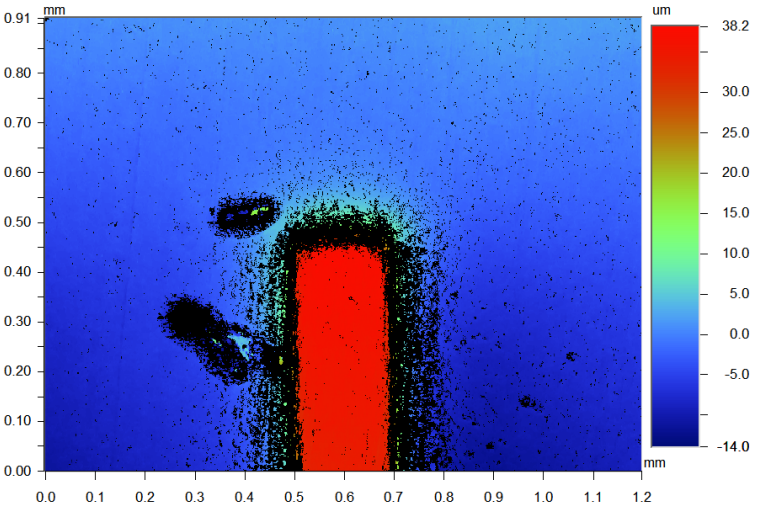

FIGURE A.5: Contour plot showing the surface profile of line feature AX4.

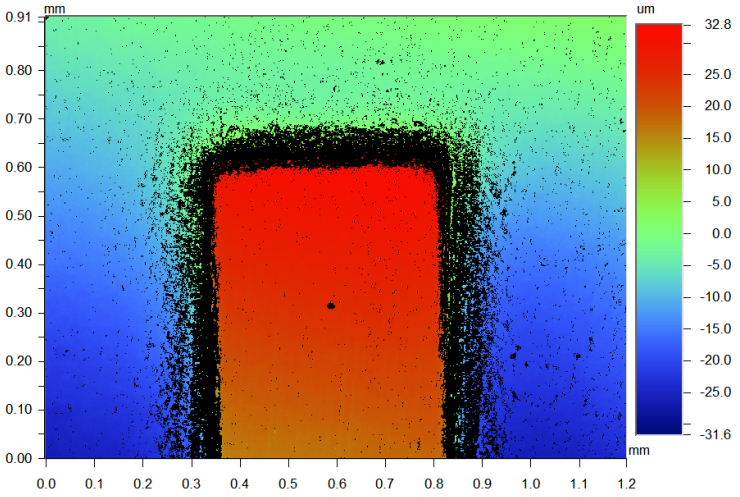

FIGURE A.6: Contour plot showing the surface profile of line feature AX5.

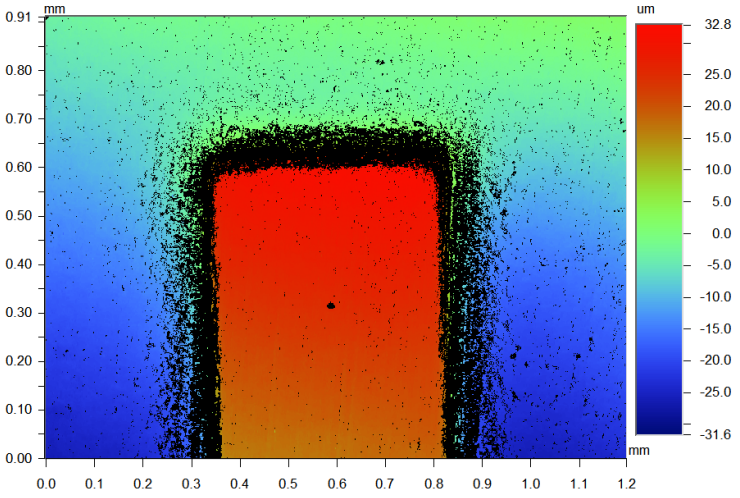

FIGURE A.7: Contour plot showing the surface profile of line feature AX5.

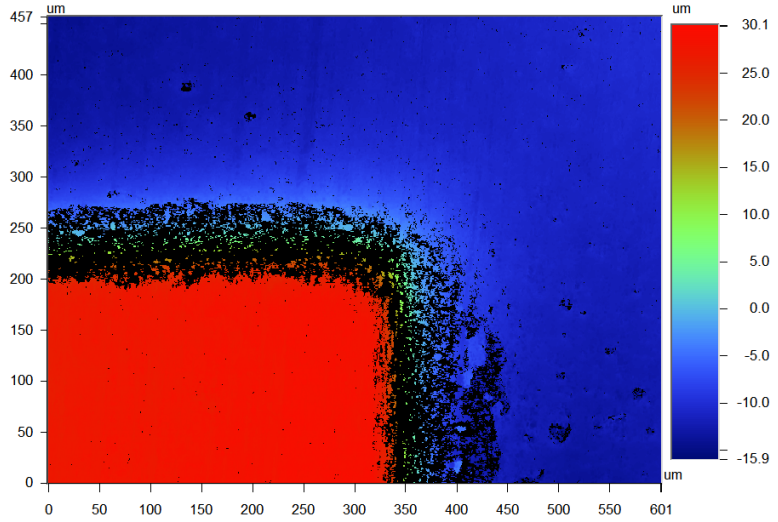

FIGURE A.8: Contour plot showing the surface profile of line feature AX6.

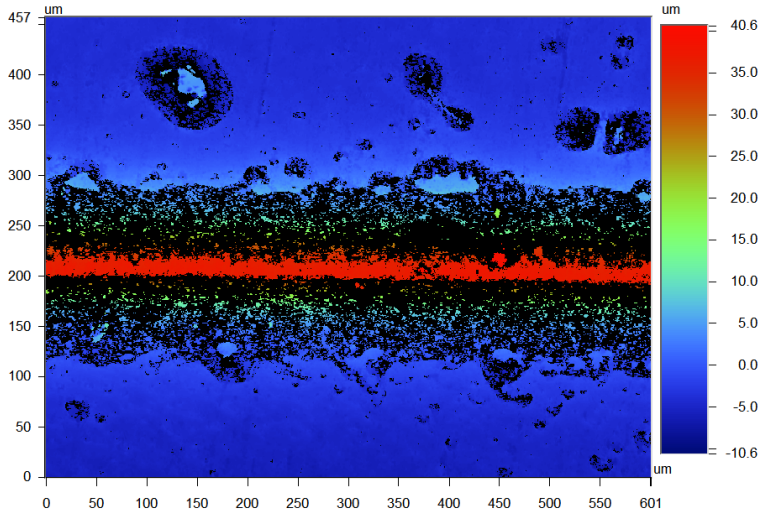

FIGURE A.9: Contour plot showing the surface profile of line feature AY2.

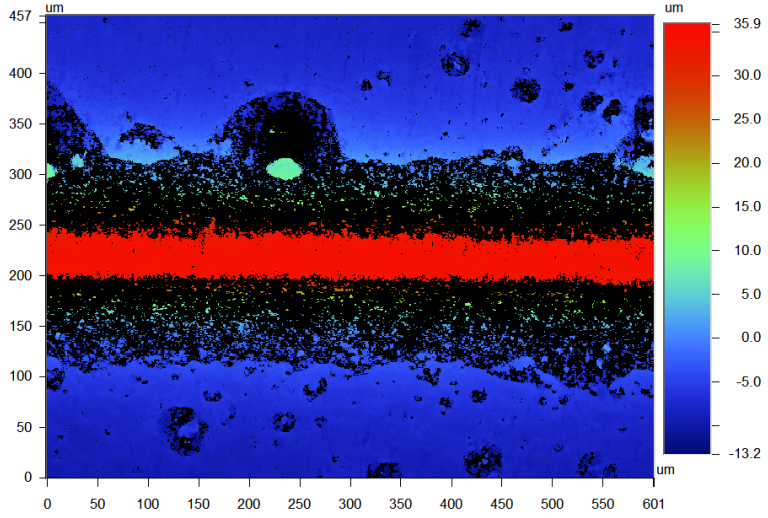

FIGURE A.10: Contour plot showing the surface profile of line feature AY3.

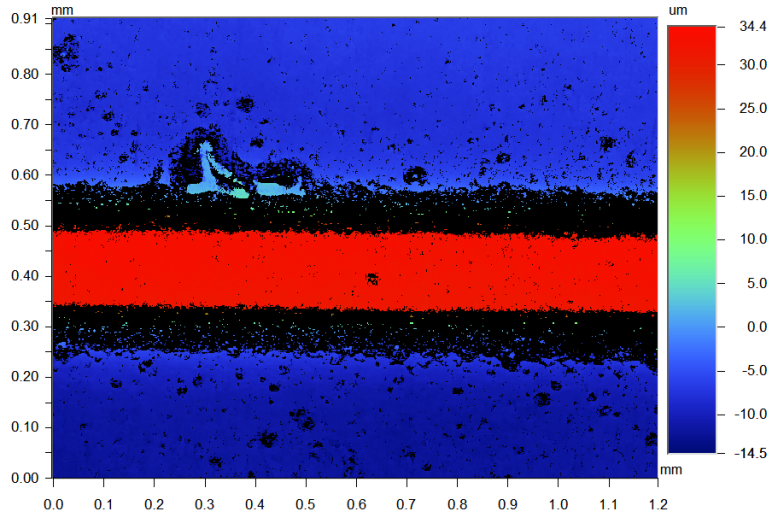

FIGURE A.11: Contour plot showing the surface profile of line feature AY4.

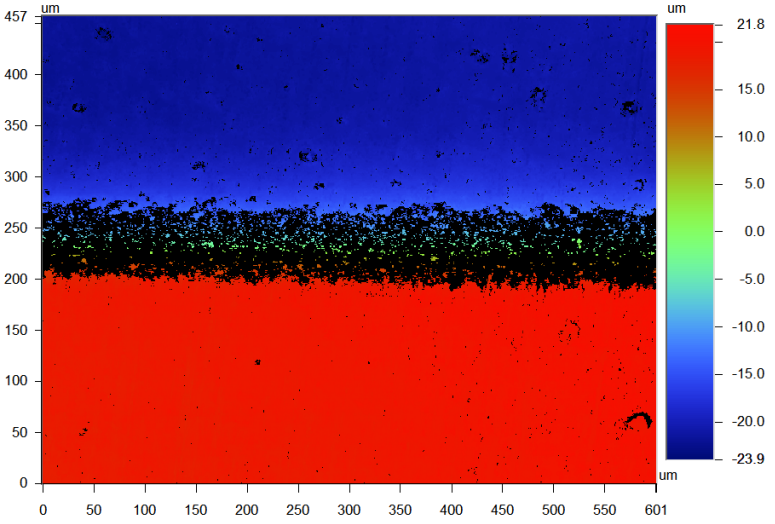

FIGURE A.12: Contour plot showing the surface profile of line feature AY5.

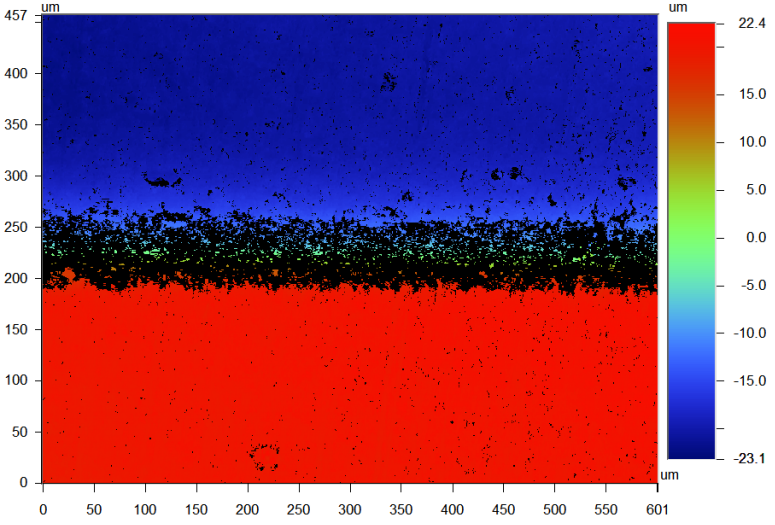

FIGURE A.13: Contour plot showing the surface profile of line feature AY6.

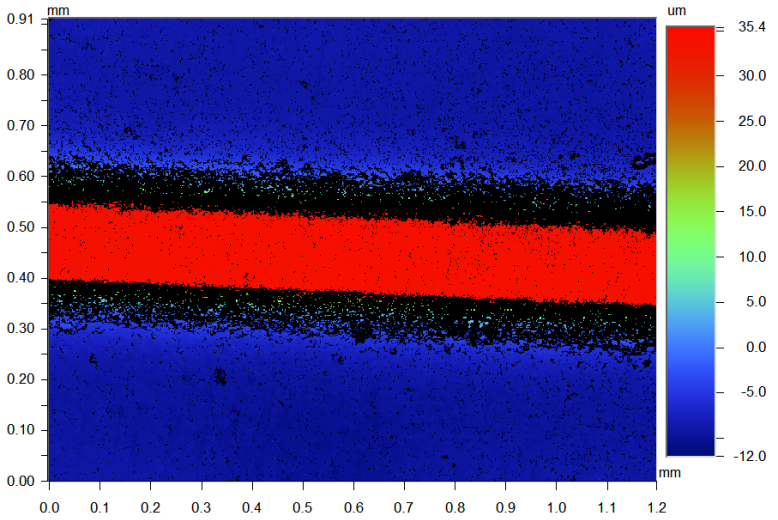

FIGURE A.14: Contour plot showing the surface profile of line feature B1.

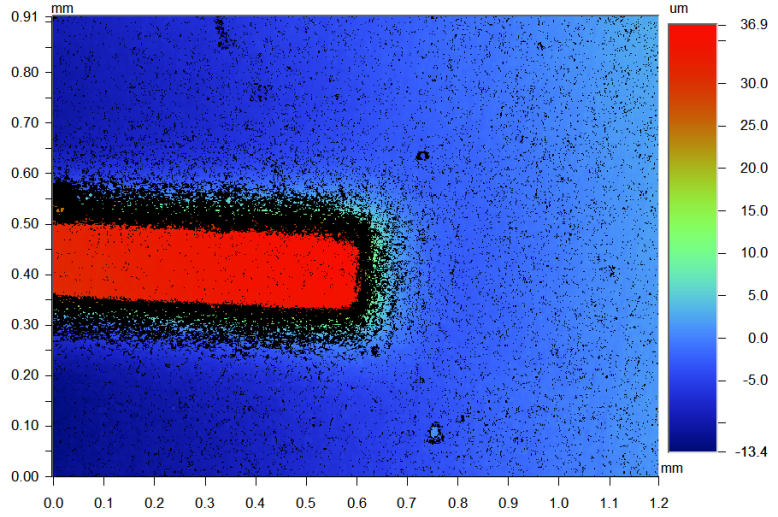

FIGURE A.15: Contour plot showing the surface profile of feature B2.

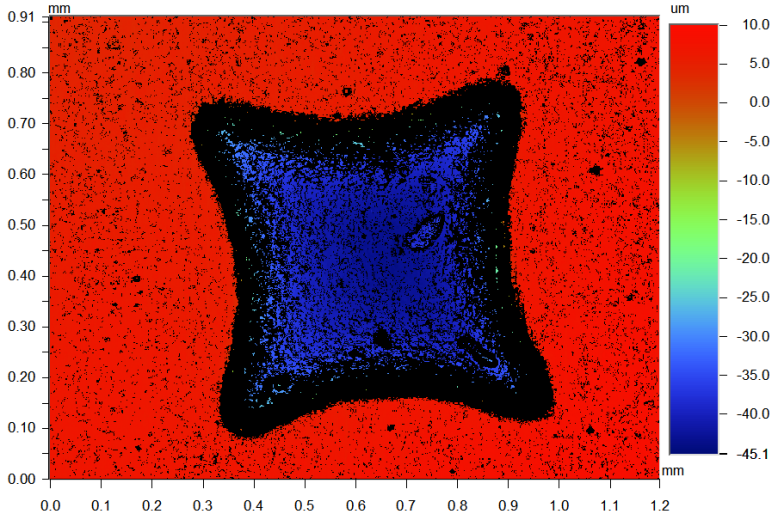

FIGURE A.16: Contour plot showing the surface profile of feature C1.

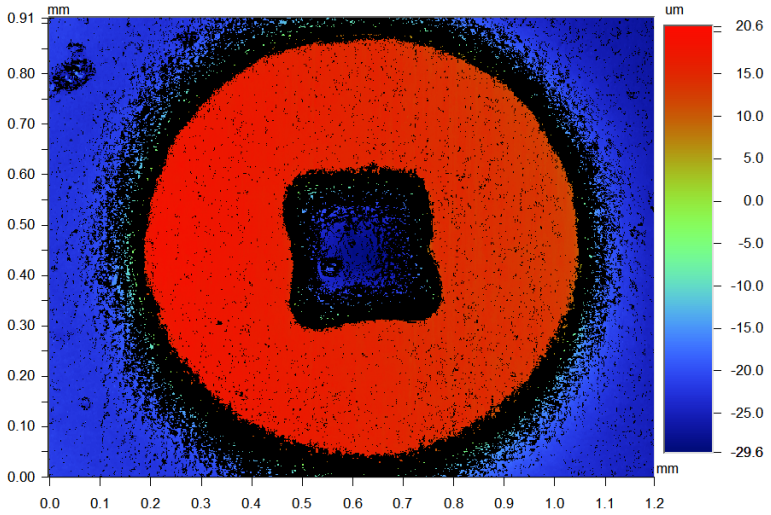

FIGURE A.17: Contour plot showing the surface profile of feature C2.

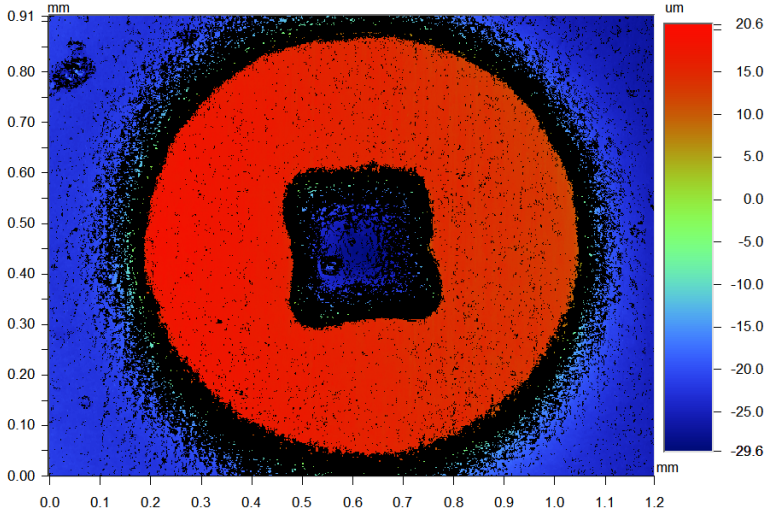

FIGURE A.18: Contour plot showing the surface profile of feature C3.

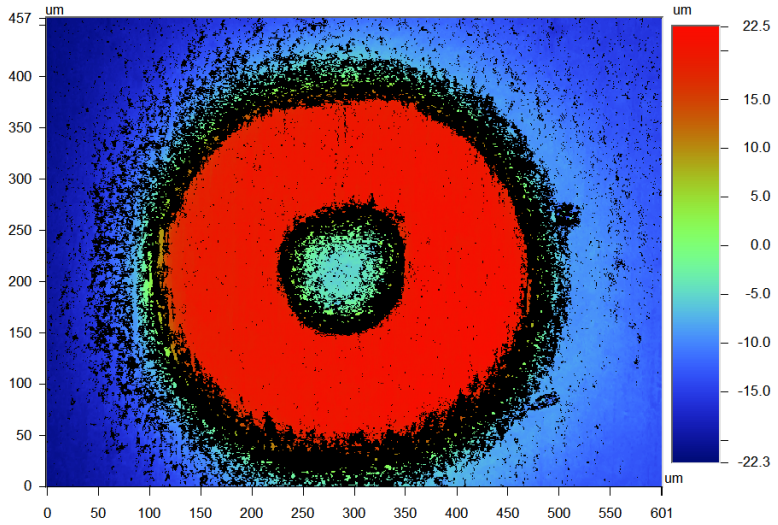

FIGURE A.19: Contour plot showing the surface profile of feature C4.

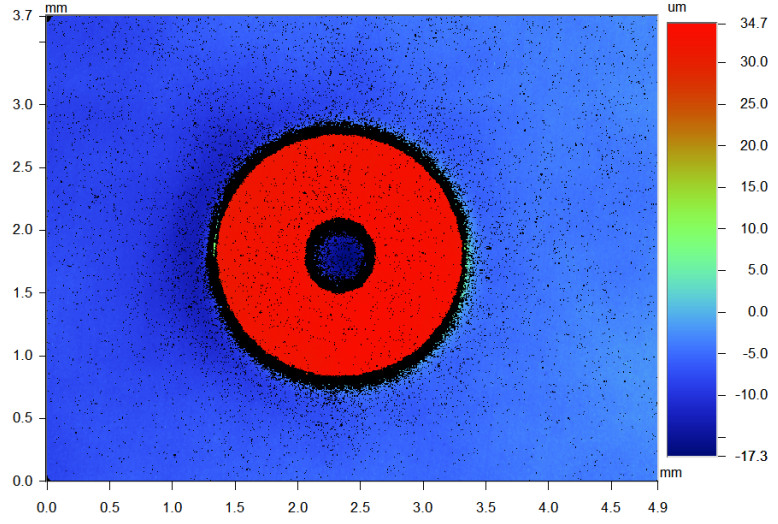

FIGURE A.20: Contour plot showing the surface profile of feature C5.

References

[1] O. Geschke, H. Klank, and P. Telleman, *Microsystem Engineering of Lab-on-a-Chip Devices*. Weinheim: Wiley-VCH Verlag GmbH & Co. KGaA, nov 2003.

[2] E. Oosterbroek, *Lab-on-a-Chip. Miniaturised Systems for (Bio)Chemical Analysis and Synthesis*. 2003.

[3] Y. Ghallab and W. Badawy, *Lab-on-a-chip: Techniques, Circuits, and Biomedical Applications*. 2010.

[4] G. J. Kost, *Principles and Practice of Point-of-Care Testing*. Lippincott Williams & Wilkins, 2002.

[5] S. K. Sia and L. J. Kricka, "Microfluidics and point-of-care testing," *Lab on a Chip*, vol. 8, pp. 1982–3, dec 2008.

[6] G. M. Whitesides, "The origins and the future of microfluidics.," *Nature*, vol. 442, no. July, pp. 368–373, 2006.

[7] E. K. Sackmann, A. L. Fulton, and D. J. Beebe, "The present and future role of microfluidics in biomedical research," *Nature*, vol. 507, pp. 181–189, mar 2014.

[8] A. Van den Berg and P. Bergveld, "Labs-on-a-Chip: origin, highlights and future perspectives. On the occasion of the 10th microTAS conference.," *Lab on a chip*, vol. 6, no. 10, pp. 1266–1273, 2006.

[9] Y. Ghallab and W. Badawy, "Sensing methods for dielectrophoresis phenomenon: From bulky instruments to lab-on-a-chip," *IEEE Circuits and Systems Magazine*, vol. 4, no. 3, pp. 5–15, 2004.

[10] H. Becker, "Mind the gap!," *Lab Chip*, vol. 10, no. 3, pp. 271–273, 2010.

[11] S. Franssila, *Introduction to Microfabrication*, vol. 54. 2005.

[12] J. W. Hong and S. R. Quake, "Integrated nanoliter systems," 2003.

[13] D. B. Weibel, M. Kruithof, S. Potenta, S. K. Sia, A. Lee, and G. M. Whitesides, "Torque-actuated valves for microfluidics," *Analytical Chemistry*, vol. 77, no. 15, pp. 4726–4733, 2005.

[14] P. Garstecki, M. A. Fischbach, and G. M. Whitesides, "Design for mixing using bubbles in branched microfluidic channels," *Applied Physics Letters*, vol. 86, no. 24, pp. 1–3, 2005.

[15] N. T. Nguyen and Z. Wu, "Micromixers - A review," 2005.

[16] A. Günther, M. Jhunjhunwala, M. Thalmann, M. A. Schmidt, and K. F. Jensen, "Micromixing of miscible liquids in segmented gas-liquid flow," *Langmuir*, vol. 21, no. 4, pp. 1547–1555, 2005.

[17] N. T. Nguyen, X. Huang, and T. K. Chuan, "MEMS-Micropumps: A Review," *Journal of Fluids Engineering*, vol. 124, no. 2, p. 384, 2002.

[18] D. J. Laser and J. G. Santiago, "A review of micropumps," 2004.

[19] G. M. Walker and D. J. Beebe, "A passive pumping method for microfluidic devices," *Lab on a Chip*, vol. 2, no. 3, p. 131, 2002.

[20] S. H. Lee, A. J. Helnz, S. Shln, Y. G. Jung, S. E. Chol, W. Park, J. H. Roe, and S. Kwon, "Capillary based patterning of cellular communities in laterally open channels," *Analytical Chemistry*, vol. 82, no. 7, pp. 2900–2906, 2010.

[21] S. M. Berry, L. J. MacCoux, and D. J. Beebe, "Streamlining immunoassays with immiscible filtrations assisted by surface tension," *Analytical Chemistry*, vol. 84, no. 13, pp. 5518–5523, 2012.

[22] S. L. Anna, N. Bontoux, and H. A. Stone, "Formation of dispersions using "flow focusing" in microchannels," *Applied Physics Letters*, vol. 82, no. 3, pp. 364–366, 2003.

[23] C. Zhang and D. Xing, "Miniaturized PCR chips for nucleic acid amplification and analysis: Latest advances and future trends," *Nucleic Acids Research*, vol. 35, no. 13, pp. 4223–4237, 2007.

[24] A. M. Foudeh, T. Fatanat Didar, T. Veres, and M. Tabrizian, "Microfluidic designs and techniques using lab-on-a-chip devices for pathogen detection for point-of-care diagnostics," *Lab on a Chip*, vol. 12, no. 18, p. 3249, 2012.

[25] C. L. Hansen, E. Skordalakes, J. M. Berger, and S. R. Quake, "A robust and scalable microfluidic metering method that allows protein crystal growth by free interface diffusion," *Proceedings of the National Academy of Sciences*, vol. 99, no. 26, pp. 16531–16536, 2002.

[26] J. U. Shim, G. Cristobal, D. R. Link, T. Thorsen, and S. Fraden, "Using microfluidics to decouple nucleation and growth of protein crystals," *Crystal Growth & Design*, vol. 7, no. 11, pp. 2192–2194, 2007.

[27] C. A. Mills, E. Martinez, F. Bessueille, G. Villanueva, J. Bausells, J. Samitier, and A. Errachid, "Production of structures for microfluidics using polymer imprint techniques," *Microelectronic Engineering*, vol. 78-79, pp. 695–700, mar 2005.

[28] H. Cao, Z. N. Yu, J. Wang, J. O. Tegenfeldt, R. H. Austin, E. Chen, W. Wu, and S. Y. Chou, "Fabrication of 10 nm enclosed nanofluidic channels," *Applied Physics Letters*, vol. 81, p. 174, jun 2002.

[29] H. Becker and C. Gärtner, "Polymer microfabrication technologies for microfluidic systems.," *Analytical and bioanalytical chemistry*, vol. 390, pp. 89–111, jan 2008.

[30] M. Worgull, *Modeling and Process Simulation.* Oxford: Elsevier, 2009.

[31] L. Peng, Y. Deng, P. Yi, and X. Lai, "Micro hot embossing of thermoplastic polymers: a review," *Journal of Micromechanics and Microengineering*, vol. 24, p. 013001, jan 2014.

[32] M. Worgull, A. Kolew, M. Heilig, M. Schneider, H. Dinglreiter, and B. Rapp, "Hot embossing of high performance polymers," *Microsystem Technologies*, vol. 17, pp. 585–592, oct 2010.

[33] R. K. Jena, C. Y. Yue, Y. Lam, P. Tang, and a. Gupta, "Comparison of different molds (epoxy, polymer and silicon) for microfabrication by hot embossing technique," *Sensors and Actuators B: Chemical*, vol. 163, pp. 233–241, mar 2012.

[34] R. K. Jena, S. a. Chester, V. Srivastava, C. Y. Yue, L. Anand, and Y. C. Lam, "Large-strain thermo-mechanical behavior of cyclic olefin copolymers: Application to hot embossing and thermal bonding for the fabrication of microfluidic devices," *Sensors and Actuators B: Chemical*, vol. 155, pp. 93–105, jul 2011.

[35] H. K. Taylor, M. Hale, Y. C. Lam, and D. Boning, "A method for the accelerated simulation of micro-embossed topographies in thermoplastic polymers," *Journal of Micromechanics and Microengineering*, vol. 20, p. 065001, jun 2010.

[36] L. P. Yeo, S. H. Ng, and Z. F. Wang, "Investigation of hot roller embossing for microfluidic devices," *Journal of Micromechanics and Microengineering*, vol. 20, p. 015017, jan 2010.

[37] S. H. Ng and Z. F. Wang, "Hot roller embossing for microfluidics: process and challenges," *Microsystem Technologies*, vol. 15, pp. 1149–1156, oct 2008.

[38] A. E. Guber, M. Heckele, D. Herrmann, A. Muslija, V. Saile, L. Eichhorn, T. Gietzelt, W. Hoffmann, P. C. Hauser, J. Tanyanyiwa, A. Gerlach, N. Gottschlich, and G. Knebel, "Microfluidic lab-on-a-chip systems based on polymers - fabrication and application," *Chemical Engineering Journal*, vol. 101, no. 1-3, pp. 447–453, 2004.

[39] C.-T. Pan, H. Yang, S.-C. Shen, M.-C. Chou, and H.-P. Chou, "A low-temperature wafer bonding technique using patternable materials," *Journal of Micromechanics and Microengineering*, vol. 12, pp. 611–615, sep 2002.

[40] L. H. Sperling, *Introduction to Physical Polymer Science*, vol. 78. 2006.

[41] J. E. Mark, ed., *Polymer Data Handbook*. Oxford University Press, 1999.

[42] H. Becker and U. Heim, "Silicon as tool material for polymer hot embossing," in *Twelfth IEEE International Conference on Micro Electro Mechanical Systems*, pp. 228–231, IEEE, 1999.

[43] M. B. Esch, S. Kapur, G. Irizarry, and V. Genova, "Influence of master fabrication techniques on the characteristics of embossed microfluidic channels.," *Lab on a chip*, vol. 3, pp. 121–7, may 2003.

[44] J. Steigert, S. Haeberle, T. Brenner, C. Müller, C. P. Steinert, P. Koltay, N. Gottschlich, H. Reinecke, J. Rühe, R. Zengerle, and J. Ducrée, "Rapid prototyping of microfluidic chips in COC," *Journal of Micromechanics and Microengineering*, vol. 17, pp. 333–341, feb 2007.

[45] A. Shamsi, A. Amiri, P. Heydari, H. Hajghasem, M. Mohtashamifar, and M. Esfandiari, "Low cost method for hot embossing of microstructures on PMMA by SU-8 masters," *Microsystem Technologies*, vol. 20, no. 10-11, 2014.

[46] J. Narasimhan and I. Papautsky, "Polymer embossing tools for rapid prototyping of plastic microfluidic devices," *Journal of Micromechanics and Microengineering*, vol. 14, pp. 96–103, jan 2004.

[47] M. Kim, B.-U. Moon, and C. H. Hidrovo, "Enhancement of the thermo-mechanical properties of PDMS molds for the hot embossing of PMMA microfluidic devices," *Journal of Micromechanics and Microengineering*, vol. 23, no. 9, 2013.

[48] Y. Xia and G. M. Whitesides, "Soft lithography," *Annual Review of Material science*, vol. 28, no. 12, pp. 153–184, 1998.

[49] M. A. Unger, "Monolithic Microfabricated Valves and Pumps by Multilayer Soft Lithography," *Science*, vol. 288, pp. 113–116, apr 2000.

[50] D. Qin, Y. Xia, and G. M. Whitesides, "Soft lithography for micro- and nanoscale patterning," *Nature Protocols*, 2010.

[51] V. Piotter, K. Mueller, K. Plewa, R. Ruprecht, and J. Hausselt, "Performance and simulation of thermoplastic micro injection molding," *Microsystem Technologies*, vol. 8, no. 6, pp. 387–390, 2002.

[52] D. A. Mair, E. Geiger, A. P. Pisano, J. M. J. Fréchet, and F. Svec, "Injection molded microfluidic chips featuring integrated interconnects," *Lab Chip*, vol. 6, no. 10, pp. 1346–1354, 2006.

[53] D. S. Kim, S. H. Lee, C. H. Ahn, J. Y. Lee, and T. H. Kwon, "Disposable integrated microfluidic biochip for blood typing by plastic microinjection moulding," *Lab on a Chip*, vol. 6, no. 6, p. 794, 2006.

[54] U. M. Attia, S. Marson, and J. R. Alcock, "Micro-injection moulding of polymer microfluidic devices," *Microfluidics and Nanofluidics*, vol. 7, no. 1, pp. 1–28, 2009.

[55] M. B. Chan-Park and W. K. Neo, "Ultraviolet embossing for patterning high aspect ratio polymeric microstructures," *Microsystem Technologies*, vol. 9, no. 6-7, pp. 501–506, 2003.

[56] M. Worgull, *Hot Embossing*. Oxford: Elsevier, 2009.

[57] H. Becker and U. Heim, "Hot embossing as a method for the fabrication of polymer high aspect ratio structures," *Sensors and Actuators a-Physical*, vol. 83, no. 1-3, pp. 130–135, 2000.

[58] J. P. Hulme, S. Mohr, N. J. Goddard, and P. R. Fielden, "Rapid prototyping for injection moulded integrated microfluidic devices and diffractive element arrays.," *Lab on a chip*, vol. 2, pp. 203–6, nov 2002.

[59] H.-S. Noh, Y. Huang, and P. J. Hesketh, "Parylene micromolding, a rapid and low-cost fabrication method for parylene microchannel," *Sensors and Actuators B: Chemical*, vol. 102, pp. 78–85, sep 2004.

[60] L. Brown, T. Koerner, J. H. Horton, and R. D. Oleschuk, "Fabrication and characterization of poly(methylmethacrylate) microfluidic devices bonded using surface modifications and solvents.," *Lab on a chip*, vol. 6, pp. 66–73, jan 2006.

[61] R. Truckenmüller, R. Ahrens, Y. Cheng, G. Fischer, and V. Saile, "An ultrasonic welding based process for building up a new class of inert fluidic microsensors and -actuators from polymers," *Sensors and Actuators A: Physical*, vol. 132, pp. 385–392, nov 2006.

[62] F. Dang, S. Shinohara, O. Tabata, Y. Yamaoka, M. Kurokawa, Y. Shinohara, M. Ishikawa, and Y. Baba, "Replica multichannel polymer chips with a network of sacrificial channels sealed by adhesive printing method.," *Lab on a chip*, vol. 5, pp. 472–8, apr 2005.

[63] M. Hösel and F. C. Krebs, "Large-scale roll-to-roll photonic sintering of flexo printed silver nanoparticle electrodes," *Journal of Materials Chemistry*, vol. 22, no. 31, p. 15683, 2012.

[64] M. Allen, C. Lee, B. Ahn, T. Kololuoma, K. Shin, and S. Ko, "R2R gravure and inkjet printed RF resonant tag," *Microelectronic Engineering*, vol. 88, no. 11, pp. 3293–3299, 2011.

[65] "Research and development activities in printed intelligence," tech. rep., VTT Finland, 2009.

[66] L. T. Jiang, T. C. Huang, C. R. Chiu, C. Y. Chang, and S. Y. Yang, "Fabrication of plastic microlens arrays using hybrid extrusion rolling embossing with a metallic cylinder mold fabricated using dry film resist.," *Optics express*, vol. 15, no. 19, pp. 12088–12094, 2007.

[67] N. Ishizawa, K. Idei, T. Kimura, D. Noda, and T. Hattori, "Resin micromachining by roller hot embossing," in *Microsystem Technologies*, vol. 14, pp. 1381–1388, 2008.

[68] D. Yun, Y. Son, J. Kyung, and H. Park, "Development of roll-to-roll hot embossing system with induction heater for micro fabrication," *Review of Scientific Instruments*, vol. 83, p. 015108, jan 2012.

[69] S. J. Liu, C. C. Huang, and C. T. Liao, "Continuous infrared-assisted double-sided roll-to-roll embossing of flexible polymer substrates," *Polymer Engineering and Science*, vol. 52, no. 7, pp. 1395–1401, 2012.

[70] L. P. Yeo, S. H. Ng, Z. F. Wang, Z. P. Wang, and N. F. de Rooij, "Micro-fabrication of polymeric devices using hot roller embossing," *Microelectronic Engineering*, vol. 86, pp. 933–936, apr 2009.

[71] M. D. Fagan, B. H. Kim, and D. Yao, "A novel process for continuous thermal embossing of large-area nanopatterns onto polymer films," *Advances in Polymer Technology*, vol. 28, no. 4, pp. 246–256, 2009.

[72] T. Velten, H. Schuck, M. Richter, G. Klink, K. Bock, C. K. Malek, S. Roth, H. Schoo, and P. J. Bolt, "Microfluidics on foil: State of the art and new developments," *Proceedings of the Institution of Mechanical Engineers, Part B: Journal of Engineering Manufacture*, 2008.

[73] S. Kim, Y. Son, H. Park, B. Kim, and D. Yun, "Effects of Preheating and Cooling Durations on Roll-to-Roll Hot Embossing," *Microscopy and Microanalysis*, vol. 21, no. 1, pp. 164–171, 2015.

[74] T. Velten, F. Bauerfeld, H. Schuck, S. Scherbaum, C. Landesberger, and K. Bock, "Roll-to-roll hot embossing of microstructures," in *Microsystem Technologies*, vol. 17, (Seville, Spain), pp. 619–627, 2011.

[75] A. L. Vig, T. Mäkelä, P. Majander, V. Lambertini, J. Ahopelto, and A. Kristensen, "Roll-to-roll fabricated lab-on-a-chip devices," *Journal of Micromechanics and Microengineering*, vol. 21, p. 035006, mar 2011.

[76] R. Liedert, L. K. Amundsen, A. Hokkanen, M. Mäki, A. Aittakorpi, M. Pakanen, J. R. Scherer, R. a. Mathies, M. Kurkinen, S. Uusitalo, L. Hakalahti, T. K. Nevanen, H. Siitari, and H. Söderlund, "Disposable roll-to-roll hot embossed electrophoresis chip for detection of antibiotic resistance gene mecA in bacteria.," *Lab on a chip*, vol. 12, pp. 333–9, jan 2012.

[77] C.-W. Tsao, T.-Y. Chen, W. Y. Woon, and C.-J. Lo, "Rapid polymer microchannel fabrication by hot roller embossing process," *Microsystem Technologies*, vol. 18, pp. 713–722, apr 2012.

[78] G. Cheng, M. Sahli, J. C. Gelin, and T. Barriere, "Process parameter effects on dimensional accuracy of a hot embossing process for polymer-based micro-fluidic device manufacturing," *The International Journal of Advanced Manufacturing Technology*, vol. 75, no. 1-4, pp. 225–235, 2014.

[79] J. Zhang, M. Sahli, J. C. Gelin, and T. Barriere, "Roll manufacturing of polymer microfluidic devices using a roll embossing process," *Sensors and Actuators A: Physical*, vol. 230, pp. 156–169, 2015.

[80] J. Wang, P. Yi, Y. Deng, L. Peng, X. Lai, and J. Ni, "Mechanism of forming defects in roll-to-roll hot embossing of micro-pyramid arrays: II. Numerical study," *Journal of Micromechanics and Microengineering*, vol. 25, no. 11, p. 115030, 2015.

[81] B. Feyssa, C. Liedert, L. Kivimaki, L.-S. Johansson, H. Jantunen, and L. Hakalahti, "Patterned immobilization of antibodies within roll-to-roll hot embossed polymeric microfluidic channels.," *PloS one*, vol. 8, p. e68918, jan 2013.

[82] K. Metwally, S. Queste, L. Robert, R. Salut, and C. Khan-Malek, "Hot roll embossing in thermoplastic foils using dry-etched silicon stamp and multiple passes," *Microelectronic Engineering*, vol. 88, no. 8, pp. 2679–2682, 2011.

[83] S. Miserere, G. Mottet, V. Taniga, S. Descroix, J.-L. Viovy, and L. Malaquin, "Fabrication of thermoplastics chips through lamination based techniques.," *Lab on a chip*, vol. 12, pp. 1849–56, apr 2012.

[84] H. Becker and L. E. Locascio, "Polymer microfluidic devices," *Talanta*, vol. 56, pp. 267–87, feb 2002.

[85] J. H. Jeong, Y. S. Choi, Y. J. Shin, J. J. Lee, K. T. Park, E. S. Lee, and S. R. Lee, "Flow behavior at the embossing stage of nanoimprint lithography," *Fibers and Polymers*, 2002.

[86] P. J. Carreau, "Rheological Equations from Molecular Network Theories," *Transactions of the Society of Rheology*, 1972.

[87] K. Yosuda, *Investigation of the analogies between viscometric and linear viscoelastic properties of polystyrene fluids*. PhD thesis, MIT, 1979.

[88] Y. J. Juang, L. Lee James, and W. Koelling, "Hot embossing in microfabrication. Part II: Rheological characterization and process analysis," *Polymer Engineering and Science*, 2002.

[89] H. C. Scheer, N. Bogdanski, and M. Wissen, "Polymer time constants during low temperature nanoimprint lithography," *Journal of Vacuum Science & Technology B*, vol. 23, no. 2963, 2005.

[90] A. F. Bower, *Applied Mechanics of Solids*. Boca Raton: CRC Press, 2011.

[91] M. L. Williams, R. F. Landel, and J. D. Ferry, "The Temperature Dependence of Relaxation Mechanisms in Amorphous Polymers and Other Glass-forming Liquids1," *Journal of the American Chemical Society*, vol. 77, no. 12, pp. 3701–3707, 1955.

[92] M. Worgull and M. Heckele, "New aspects of simulation in hot embossing," *Microsystem Technologies*, vol. 10, no. 5, pp. 432–437, 2004.

[93] N. W. Kim, K. W. Kim, and H.-C. Sin, "Finite element analysis of low temperature thermal nanoimprint lithography using a viscoelastic model," *Microelectronic Engineering*, vol. 85, pp. 1858–1865, sep 2008.

[94] M. Sahli, C. K. Malek, and J. C. Gelin, "3D modelling and simulation of the filling of cavities by viscoelastic polymer in roll embossing process," *International Journal of Material Forming*, vol. 2, pp. 725–728, dec 2009.

[95] R. K. Jena, X. Chen, C. Y. Yue, and Y. C. Lam, "Rheological (visco-elastic behaviour) analysis of cyclic olefin copolymers with application to hot embossing for microfabrication," *Journal of Micromechanics and Microengineering*, vol. 21, p. 085029, aug 2011.

[96] A. A. Abdel-Wahab, S. Ataya, and V. V. Silberschmidt, "Temperature-dependent mechanical behaviour of PMMA: Experimental analysis and modelling," *Polymer Testing*, vol. 58, pp. 86–95, 2017.

[97] L. R. G. Treloar, "Stresses and birefringence in rubber subjected to general homogeneous strain," *Proceedings of the Physical Society*, vol. 60, no. 2, pp. 135–144, 1948.

[98] M. Mooney, "A theory of large elastic deformation," *Journal of Applied Physics*, vol. 11, no. 9, pp. 582–592, 1940.

[99] O. H. Yeoh, "Some forms of the strain energy function for rubber," *Rubber Chemistry and Technology*, 1993.

[100] E. M. Arruda and M. C. Boyce, "A three-dimensional constitutive model for the large stretch behavior of rubber elastic materials," *Journal of the Mechanics and Physics of Solids*, vol. 41, no. 2, pp. 389–412, 1993.

[101] R. S. Marlow, "A general first-invariant hyperelastic constitutive model," *Constitutive Models for Rubber III*, pp. 157–160, 2003.

[102] H. Bourbaba, C. Ben Achaiba, and B. Mohamed, "Mechanical behavior of polymeric membrane: Comparison between PDMS and PMMA for micro fluidic application," in *Energy Procedia*, 2013.

[103] Y. Hirai, T. Konishi, T. Yoshikawa, and S. Yoshida, "Simulation and experimental study of polymer deformation in nanoimprint lithography," *Journal of Vacuum Science & Technology B: Microelectronics and Nanometer Structures*, 2004.

[104] H. Hocheng and C. C. Nien, "Numerical analysis of effects of mold features and contact friction on cavity filling in the nanoimprinting process," *Journal of Microlithography, Microfabrication, and Microsystems*, vol. 5, 2006.

[105] R. B. Dupaix and M. C. Boyce, "Constitutive modeling of the finite strain behavior of amorphous polymers in and above the glass transition," *Mechanics of Materials*, vol. 39, pp. 39–52, jan 2007.

[106] C. Liu, J. M. Li, J. S. Liu, and L. D. Wang, "Deformation behavior of solid polymer during hot embossing process," *Microelectronic Engineering*, vol. 87, pp. 200–207, feb 2010.

[107] A. Ghatak and R. B. Dupaix, "Material Characterization and Continuum Modeling of Poly (Methyl Methacrylate)(PMMA) above the Glass Transition," *International Journal of Structural Changes in Solids*, vol. 2, no. 1, pp. 53–63, 2010.

[108] N. M. Ames, *A thermo-mechanical finite deformation theory of plasticity for amorphous polymers: application to micro-hot-embossing of poly (methyl methacrylate)*. PhD thesis, MIT, 2007.

[109] H. K. Taylor, Y. C. Lam, and D. Boning, "A computationally simple method for simulating the micro-embossing of thermoplastic layers," *Journal of Micromechanics and Microengineering*, vol. 19, p. 075007, jul 2009.

[110] R. K. Jena, H. K. Taylor, Y. C. Lam, D. Boning, and C. Y. Yue, "Effect of polymer orientation on pattern replication in a micro-hot embossing process: experiments and numerical simulation," *Journal of Micromechanics and Microengineering*, vol. 21, p. 065007, jun 2011.

[111] Y. Hirai, S. Yoshida, and N. Takagi, "Defect analysis in thermal nanoimprint lithography," *Journal of Vacuum Science & Technology B: Microelectronics and Nanometer Structures*, 2003.

[112] M. Worgull, "Modeling of large area hot embossing," in *DTIP*, 2007.

[113] Y. He, J. Z. Fu, and Z. C. Chen, "Research on optimization of the hot embossing process," *Journal of Micromechanics and Microengineering*, 2007.

[114] M. E. Dirckx, *Demolding of hot embossed polymer microstructures.* PhD thesis, MIT, 2010.

[115] C. Martin, L. Ressier, and J. P. Peyrade, "Study of PMMA recoveries on micrometric patterns replicated by nano-imprint lithography," in *Physica E: Low-Dimensional Systems and Nanostructures*, 2003.

[116] N. M. Ames, V. Srivastava, S. A. Chester, and L. Anand, "A thermo-mechanically coupled theory for large deformations of amorphous polymers. Part II: Applications," *International Journal of Plasticity*, vol. 25, no. 8, pp. 1495–1539, 2009.

[117] Y. Deng, P. Yi, L. Peng, X. Lai, and Z. Lin, "Flow behavior of polymers during the roll-to-roll hot embossing process," *Journal of Micromechanics and Microengineering*, vol. 25, no. 6, p. 065004, 2015.

[118] A. international, *ASM Handbook, Volume 08: Mechanical Testing and Evaluation.* ASM International, 2000.

[119] A. D. Mulliken and M. C. Boyce, "Mechanics of the rate-dependent elastic–plastic deformation of glassy polymers from low to high strain rates," *International Journal of Solids and Structures*, vol. 43, pp. 1331–1356, mar 2006.

[120] "DMA/SDTA 1 Product Brochure," 2017.

[121] Evonik, "Technical Information: Plexiglas."

[122] A. D. Mulliken, *Low to high strain rate deformation of amorphous polymers: experiments and modeling*. PhD thesis, MIT, 2004.

[123] H. Klank, J. P. Kutter, and O. Geschke, "CO(2)-laser micromachining and back-end processing for rapid production of PMMA-based microfluidic systems.," *Lab on a chip*, vol. 2, no. 4, pp. 242–246, 2002.

[124] *Intron Advanced Video Extensometer Reference Manual*. Instron Corporation, revision b ed., 2004.

[125] British Standards Institute, "ISO 527-3 Plastics — Determination of tensile properties — Part 1: General principles," in *ISO standard*, pp. 1–16, 1999.

[126] British Standards Institute, "ISO 527-3 Plastics — Determination of tensile properties — Part 3: Test conditions for films and sheets," in *ISO standard*, pp. 1–12, 2004.

[127] *Abaqus 6.14 Documentation*. Simula Dassult Systemes, 2014.

[128] R.-D. Chien, "Hot embossing of microfluidic platform," *International Communications in Heat and Mass Transfer*, vol. 33, no. 5, pp. 645–653, 2006.

[129] P. Datta and J. Goettert, "Method for polymer hot embossing process development," *Microsystem Technologies*, vol. 13, no. 3-4, pp. 265–270, 2007.

[130] N. S. Cameron, H. Roberge, T. Veres, S. C. Jakeway, and H. John Crabtree, "High fidelity, high yield production of microfluidic devices by hot embossing lithography: rheology and stiction.," *Lab on a chip*, vol. 6, no. 7, pp. 936–41, 2006.

[131] D. Yao and R. Kuduva-Raman-Thanumoorthy, "An enlarged process window for hot embossing," *Journal of Micromechanics and Microengineering*, vol. 18, no. 4, p. 45023, 2008.

[132] K. Metwally, L. Robert, S. Queste, B. Gauthier-Manuel, and C. Khan-Malek, "Roll manufacturing of flexible microfluidic devices in thin PMMA and COC foils by embossing and lamination," *Microsystem Technologies*, vol. 18, pp. 199–207, oct 2011.